Mapping the Zinc Dynamics and Requirements of the Mammalian Cell Cycle

by

Samuel Ellis Holtzen

B.S. Biochemistry, Georgia Institute of Technology, 2017

A thesis submitted to the

Faculty of the Graduate School of the University of Colorado

in partial fulfillment of the requirements for the degree of

Doctor of Philosophy

College of Arts & Sciences

Department of Molecular, Cellular & Developmental Biology

2024

Committee Members:

Amy Palmer, Advisor

Robin Dowell, Chair

Nausica Arnoult

Sabrina Spencer

Lee Niswander

Abstract

Holtzen, Samuel E. (Ph.D. Molecular, Cellular, and Developmental Biology)

Mapping the Zinc Dynamics and Requirements of the Mammalian Cell Cycle

Thesis directed by Professor Amy Palmer

Ionic zinc (Zn^{2+}) is an essential micronutrient that plays important roles in maintaining cellular and organismal health. As a cofactor in catalysis and secondary messenger in signaling, Zn^{2+} plays a central but understudied role in a myriad of cellular processes including proliferation and genome stability. We are still unsure how depletion of cellular Zn^{2+} acts to impair proliferation. To address this, I used high content imaging and flow cytometry of live and fixed cells and found that short exposure to ZD impairs DNA synthesis and leads to simultaneous activation of replication stress signaling. I then identified that Zn^{2+} is required for S-phase progression, and depletion of Zn^{2+} during S-phase will elongate mother cell S-phase, as well as cause transient quiescence in daughter cells after division. This quiescence is maintained by sustained expression of the tumor suppressor p21. I also examined changes in free Zn^{2+} throughout the cell cycle. Using a genetically encoded Förster resonance energy transfer (FRET) based sensor for measuring labile Zn^{2+}, my colleagues and I found that cells experience a transient increase in labile Zn^{2+} in early G1, which we named the Zn^{2+} pulse, that scaled with available media Zn^{2+}. Knockdown of the metal responsive transcription factor MTF-1 with an shRNA impaired reestablishment of Zn^{2+} levels after perturbation. Further, knockdown of MTF-1 increased resting free Zn^{2+} by impairing expression of metallothionein. Finally, knockdown of MTF-1 decreased cell proliferation in high Zn^{2+} using both a bulk assay and single-cell microscopy. Together, this work sheds new light on Zn^{2+} regulation and fluctuations in the mammalian cell cycle.

Acknowledgements

Science doesn’t happen alone; it takes a village. The long and sometimes lonely road to a PhD is always flanked with voices of encouragement. You just have to look for them. For all the voices that encouraged me, I am so very grateful.

I want to start off by thanking my parents, who have always been my cheerleaders. They have always cultivated in me a desire to explore, and the advice they offer me, solicited and unsolicited, was always spoken with my best interest in mind. If it weren’t for you, I would have never grown into the person I am today, and for that, I am so thankful.

I want to acknowledge my MCDB cohort, and all of the hours we sat in the MCDB Core classroom, puzzling over biology, discussing life, and above all supporting each other. I couldn’t have made it through that first year without y’all, and I’m so happy to call you my cohort and my friends. I specifically want to thank Mitchell Leih and Tristan Caro, both of whom went from fellow first year, to roommate, to friend. You both have been simultaneously an uplifting and grounding presence in my life, and I’m so happy to have known y’all.

Behind every scientist is a family tree of other curious thinkers that push, pull, and support them through their foray into the unknown. I am greater than the sum of my parts thanks to the wonderful mentors that believed in me while I was still a fledgling scientist. They have taught me everything I know. Amanda Stockton, my undergraduate research advisor, who always taught me to look at problems with clear eyes, and to think outside the box. Adam Guss, my research advisor at Oak Ridge National Laboratory, who taught me to trust my instincts and believe in myself. And of course, none of the work I’ve done would have been possible without Theresa Nahreini, Joe Dragavon and all the folks who make the core facilities possible. You are always helpful, always kind, and always willing to go the extra mile. Thank you.

I wanted to extend my gratitude to the past and present members of the Palmer lab, especially Erin Richards and Leah Damon. Y’all have been such a wonderful presence throughout my PhD career, and I am eternally grateful for your words of advice and patience, and for being role models for me as I progress through the program. I am so thankful for y’all, and all of the folks that greeted me every day with smiles.

Even now, I struggle to put my gratitude for Amy Palmer into words. You believed in me in those first days all the way through to the end. You have pushed me further than I ever thought possible, and I’ve become a greater scientist and person because of you. You are an incredible, grounded scientist and I will always be so proud to call you my PhD thesis advisor. From the bottom of my heart, thank you.

I would be remiss if I didn’t thank my best friend Max. Even though we are a thousand miles away from each other, our friendship has never stalled, never wavered. No morning was complete without a “good morning” text from them, and I looked forward to it every day. A pep talk was a text and a phone call away. No matter how hard things got, I always knew that Max would be there to prop me up, get me a metaphorical cup of tea, and send me off with a “you got this, champ.” Everyone should have a Max. I’m so glad to know you.

And of course, Devin. You have always advocated for me, taught me to be kind to myself, and to accept things as they are. I couldn’t have done this without you, and I am so proud to have you in my life. Wherever this road leads, whatever path we take, we take together. I am so excited to follow where our path leads.

Table of Contents

Chapter 1: Introduction 1

1.1 Overview 1

1.2 Zn^{2+} homeostasis and signaling 2

1.3 Zn^{2+} in the mammalian cell cycle.. 11

1.4 Zn^{2+} in genome stability.. 15

1.3 Tools to measure and manipulate cellular Zn^{2+}.. 18

1.3.1 Genetically-encoded fluorescent sensors for measuring cellular labile Zn^{2+} 18

1.3.2 Small molecule tools to manipulate labile Zn^{2+} in cells.. 23

1.4 Fluorescent tools to study the mammalian cell cycle in live cells.................................. 28

1.5 Introduction to This Thesis 34

Chapter 2: Human cells experience a Zn^{2+} pulse in early G1 36

2.1 Publication Status.. 36

2.2 Abstract 36

2.3 Introduction.. 37

2.4 Results 39

2.4.1 Genetically encoded FRET-based sensor ZapCV2 illuminates intracellular Zn^{2+} dynamics.. 39

2.4.2 There is a Zn^{2+} pulse after mitosis that correlates with both nutritional and labile Zn^{2+} 44

2.4.3 MTF-1 knockdown results in higher levels of labile Zn^{2+} 47

2.4.4 Depletion of MTF-1 changes how cells respond to Zn^{2+} perturbation 51

2.4.5 MTF-1 knockdown compromises proliferation in high Zn^{2+} 58

2.4.6 MTF-1 knockdown alters the Zn^{2+} pulse following mitosis.......... 61

2.4.7 High Zn^{2+} does not induce apoptosis.......... 61

2.4.8 Cells emerging from serum starvation show different dynamics of labile Zn^{2+} compared to normally cycling cells. 66

2.5 Discussion 69

2.6 Materials and Methods 74

Cell culture 81

Plasmids and cell lines 83

Live cell imaging 85

2.7 Acknowledgements 92

Chapter 3: Transient Zn^{2+} deficiency induces replication stress and compromises daughter cell proliferation 94

3.1 Publication Status.......... 94

3.2 Abstract 94

3.3 Introduction.......... 95

3.4 Results 97

3.4.1 Zn^{2+} is required at the G1/S transition and in S-phase for normal S-phase progression 97

3.4.2 Zn^{2+} deficient cells show impaired DNA synthesis 99

3.4.3 Zn^{2+} deficient cells show signs of replication stress 99

3.4.4 Zn^{2+} deficiency does not cause double-stranded breaks, origin under-licensing, replication fork slowing, or an imbalance in the nucleotide pool ... 103

3.4.5 Transient Zn^{2+} deficiency during S-phase of the mother cell impairs proliferation of daughter cells ... 110

3.4.6 Sustained p21 expression maintains cell cycle pause induced by Zn^{2+} deficiency ... 116

3.5 Discussion ... 119

3.6 Materials and Methods ... 122

3.7 Acknowledgements ... 136

Chapter 4: Future Directions ... 137

4.1 Zinc and the cell cycle ... 137

4.2 Zinc and replication stress ... 138

Bibliography ... 139

Tables

Table 1: Concentration of cytosolic Zn^{2+} during Zn^{2+} pulse..62

Table 2: Key resources table...75

Table 3: Plasmid Sequences...82

Table 4: Materials table...122

Figures

Figure 1.1: MTF-1 regulated Zn^{2+} homeostasis....................3

Figure 1.2: Negative feedback loop formed by MTF-1, Zn^{2+}, and MT/ZnT....................7

Figure 1.3: Zn^{2+} binding proteins and selected binding affinities of Zn^{2+} finger proteins....................9

Figure 1.4: Key players in the cell cycle infrastructure....................12

Figure 1.5: Classes of fluorescent biosensors for detecting metal ions in living cells....................19

Figure 1.6: Tools to alter free and total Zn^{2+} in cells....................24

Figure 1.7: Fluorescent tools for probing the mammalian cell cycle in single cells....................27

Figure 2.1: Zn^{2+} levels influence cell proliferation over time....................40

Figure 2.2: In situ calibration of genetically encoded FRET based sensors....................41

Figure 2.3: Characterization of MCF10a cells expressing H2B-mCherry and NES-, NLS-ZapCV2 or NLS-zinc dead construct....................42

Figure 2.4: Tracking of labile zinc over the cell cycle reveals zinc dynamics around mitosis that is modulated by nutritional zinc....................45

Figure 2.5: Available zinc and MTF1 levels influence time to peak FRET after mitosis....................46

Figure 2.6: MTF-1 knockdown results in less cell proliferation under high nutritional Zn^{2+} condition....................49

Figure 2.7: MTF-1 KD cells have higher resting zinc than Scr Ctrl cells....................50

Figure 2.8: Plots of dynamic range (DR) versus fractional saturation (FS) from intracellular FRET calibration experiments....................52

Figure 2.9: Depletion of MTF-1 changes labile zinc dynamics after perturbation of available media zinc....................53

Figure 2.10: Second biological replicate of media change experiment....................55

Figure 2.11: MTF-1 KD compromises cell proliferation in high Zn^{2+}......57

Figure 2.12: Zn^{2+} pulse, mitosis, and altered Zn^{2+} dynamics following mitosis in MCF10a Scr Ctrl and MTF-1 KD cells expressing NES-ZapCV2......59

Figure 2.13: MTF-1 KD increases the magnitude of the Zn^{2+} pulse and alters Zn^{2+} dynamics following mitosis......63

Figure 2.14: MTF-1 KD cells undergo comparatively higher apoptosis than Scr-Ctrl cells in ZR50 condition......64

Figure 2.15: Serum starvation leads to 4 major populations of cells at different stages of the cell cycle, and each shows a similar Zn^{2+} pulse when aligned to mitosis......67

Figure 3.1: Cells treated with Zn^{2+} deficient media across the G1/S transition and during S-phase have an elongated S-phase......98

Figure 3.2: Zn^{2+} deficient cells show impaired DNA synthesis......100

Figure 3.3: Acute Zn^{2+} deficiency increases replication stress markers......101

Figure 3.4: A Gaussian Mixture Model identifies cell cycle phases in fixed cells expressing the FUCCI (CA) sensor......104

Figure 3.5: RPA2 foci in Zn^{2+} deficient cells resolve after resupply of Zn^{2+}......105

Figure 3.6: Zn^{2+} induced DNA synthesis impairment is not due to under licensing of origins of replication, nor is it fully due to origin firing inhibition by Chk1......107

Figure 3.7: Zn^{2+} deficiency does not activate Chk2 nor does it induce double-stranded breaks......108

Figure 3.8: Zn^{2+} deficiency does not cause imbalance or depletion of nucleotides or their precursors......109

Figure 3.9: Zn^{2+} deficiency in the mother cell S-phase causes proliferation pause in daughter cells......111

Figure 3.10: The FUCCI (CA) sensor can identify cell cycle phase transitions at a population level....114

Figure 3.11: Neither Zn^{2+} deficiency nor Zn^{2+} resupply stimulates mitotic DNA synthesis (MiDAS)....115

Figure 3.12: Transient Zn^{2+} deficiency during S-phase induces proliferation impairment accompanied by sustained p21 expression in G0....117

Chapter 1: Introduction

1.1 Overview

The building blocks of life are composed of several key elements. Some of these elements like carbon, hydrogen, nitrogen, oxygen, and sulfur are highly abundant. Others, the trace elements, are less abundant, but nonetheless play an indispensable role in allowing life to flourish (1). Ionic zinc (Zn^{2+}) is one such element. Zn^{2+} is the second most abundant transition metal ion in living organisms, and its physical and chemical properties carve out its niche in biology. Due to its full d^{10} shell of electrons, Zn^{2+} can participate in both octahedral and tetrahedral ligand binding at no thermodynamic penalty. It is the only metal ion which favors tetrahedral binding in biological systems, which is evident in the geometry of Zn^{2+} binding sites in Zn^{2+} binding proteins.

In the context of human health, adequate dietary Zn^{2+} is crucial (2). Zinc deficiency is a worldwide epidemic, affecting approximately 17% of the world's population, with rates as high as 30% in southeast Asia and sub-Saharan Africa (3). A lack of Zn^{2+}, whether from simple nutritional deficiency or dietary chelators such as phytates, can have detrimental and long-lasting effects, especially in children, which can range from chronic diarrhea, neurological deficits, and stunted growth, and can be lifelong (2, 3). Zn^{2+} excess is much less common, but can be equally severe due to secondary deficiency in Cu^{2+} and can lead to weakness, lethargy, and other neurological disorders (4). Although the precise mechanisms by which Zn^{2+} deficiency causes its hallmark symptoms are unknown, it is apparent that a window of dietary Zn^{2+} is required for optimal human health.

At a cellular level, it is even more apparent that life has evolved a complex network of regulatory proteins and pathways to maintain an optimal zinc ion concentration (5, 6). Total Zn^{2+} in cells varies with cell type, but is typically hundreds of micromolar (7). The vast majority of Zn^{2+} in the cell is bound to zinc binding proteins, of which there are almost 3000 in the human proteome

(8, 9). This bound Zn^{2+} pool acts as a reservoir for mobilizing zinc into its unbound state in response to several cellular stimuli (10–12). The exchangeable form of Zn^{2+}, called free or labile, is on the order of pico- to nanomolar (8, 10, 13), and can change rapidly in response to extracellular and intracellular stimuli, and can affect a growing list of cellular processes (11, 12, 14).

In this section, I will outline the fundamentals of Zn^{2+} homeostasis with a focus on perturbations to extracellular Zn^{2+} and the set of cellular machinery that restores and maintains homeostasis. Next, I will discuss the work that has linked perturbed cellular Zn^{2+} to changes in the mammalian cell cycle, proliferation, and DNA synthesis. I will then discuss the role of Zn^{2+} in the DNA damage response and the roles Zn^{2+} plays in maintaining genome stability. Next, I will discuss tools that researchers use to perturb and study Zn^{2+} in live cells. Finally, I will outline and describe fluorescent tools to study the cell cycle in living cells.

1.2 Zn^{2+} homeostasis and signaling

Zn^{2+} excess and deficiency are both detrimental, so life has evolved a complex network of proteins that regulate intracellular Zn^{2+} homeostasis (6). This network aims to keep labile and total Zn^{2+} within an acceptable range, while still allowing for the flexibility to transmit intra- and extracellular signals through small changes in labile Zn^{2+} levels (5, 7). The network is made up of several nodes, each corresponding to a species or class of metal regulatory proteins. The main players are the metal-responsive transcription factor MTF-1, metallothioneins (MTs), zinc transporters (ZnTs), and Zrt-, Irt-like proteins (ZIPs), all of which coordinate to maintain the free Zn^{2+} levels in cells (Figure 1.1) (15–17).

The metal regulatory transcription factor MTF-1 senses labile divalent metal cation levels and regulates the expression of several key metal binding and transporting proteins (18). This

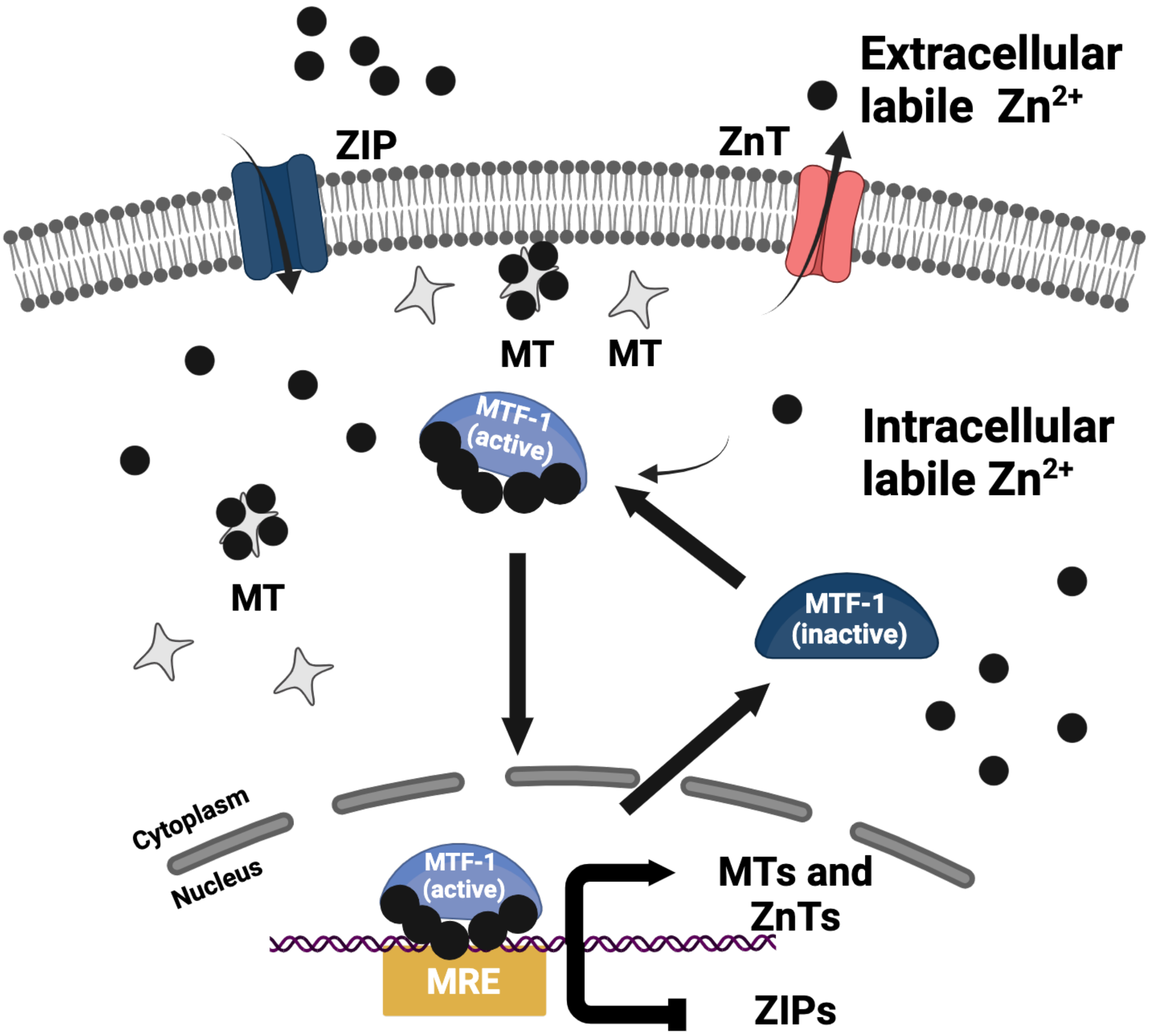

Figure 1.1: MTF-1 regulated Zn^{2+} homeostasis. MTF-1, a transcription factor that senses free Zn^{2+} concentration in the cytosol, moves to the nucleus after binding a quorum of Zn^{2+} ions. In the nucleus, MTF-1 recognizes metal responsive elements (MREs) and drives the expression of proteins that work to decrease the free Zn^{2+} concentration in the cytosol, such as ZnT transporters and metallothioneins (MTs). MTF-1 also inhibits the expression of ZIP transporters that normally act to increase the cytosolic free Zn^{2+}.

transcription factor is composed of six Zn^{2+} finger (ZF) domains, which act as sensors for transcription activation in response to increased concentrations of toxic metals such as Hg^{2+} and Cd^{2+}, as well as physiological metals such as Zn^{2+} and Cu^{+} (19). When cytosolic MTF-1 binds a quorum of Zn^{2+} ions, the protein undergoes a conformational change to expose a nuclear localization signal (NLS), which signals cellular machinery to facilitate entry into the nucleus (20). MTF-1 binds genomic metal responsive elements (MREs) corresponding to the conserved sequence TGCRCNC (21). MTF-1 binding to these MREs drives expression of MTs and ZnTs, which act to decrease free Zn^{2+} in the cytosol by buffering or exporting the ion (6, 22). There is also evidence that suggests MTF-1 can bind DNA and drive expression of Zn^{2+} responsive genes in the absence of excess metal treatment, implying either that activation is dependent on other cellular signals, or that MTF-1 maintains a basal level of transcriptional activation (18). Genes regulated by MTF-1 are not limited to Zn^{2+} homeostasis genes. Also under the control of MTF-1 are metal homeostasis genes not related to Zn^{2+} or other metals, which paints a more complex picture of MTF-1 gene regulation (19). MTF-1 can also act as a repressor of Zn^{2+} importer gene expression by physically blocking PolII from transcribing these genes (23), demonstrating that this transcription factor acts both as an activator and a repressor depending on cellular context.

Thioneins (Ts) and their metal-bound counterparts metallothioneins (MTs) are the zinc buffering workhorses of the cell(16). MTs are a class of small, cysteine-rich proteins, which act as molecular sponges to buffer excess metal ions like Zn^{2+} and Cd^{2+}. Each MT molecule can bind up to seven metal ions, affording it a high metal ion buffering capacity (24). There are four main isoforms in humans, MT1, MT2, MT3, and MT4, each with varying levels of sequence diversity and functional redundancy (25). MT concentration and localization changes with cell type and Zn^{2+}:MT stoichiometry changes with the concentration of the ion in the cytosol (16, 26). Further, MTs show a widely varying affinity for Zn^{2+} in vitro (27). Finally, the observed rate constant of Zn^{2+} binding (k_{on}) is thought to be fast, on the order of 100-300 $M^{-1}s^{-1}$, depending on the MT isoform studied (28). This high affinity and lability points to very dynamic binding of divalent metal cations to MT. In response to an intracellular Zn^{2+} concentration that surpasses the buffering capacity of MTs, MTF-1 is able to increase the buffering capacity of a cell by driving expression of more MT protein (19).

Since MTs are rich in cysteine residues, they are also susceptible to oxidation. Zn^{2+} binding to MT decreases its reactivity with the oxidizing reagent 5,5'-dithiobis-(2-nitrobenzoic acid) (DTNB), implying that Zn^{2+} offers a protective effect against oxidation of this protein (29); however, oxidation of cysteine residues decreases their ability to bind to Zn^{2+}, and can cause MT to release Zn^{2+} into the unbound state, increasing cellular labile Zn^{2+} concentration (30). The downstream effects of this liberated Zn^{2+} are still a matter of debate and ongoing investigation, but some have speculated that this newly labile Zn^{2+} activates pathways to reestablish redox homeostasis (30).

Zn^{2+} is not membrane permeable, and therefore requires an array of transporters to carry the ion across the membrane. There are two types of Zn^{2+} transporters: ZnTs and ZIPs (6). Both of these transporters serve to carry Zn^{2+} and sometimes other metals across the membrane. Neither type of transporter requires ATP hydrolysis to transport Zn^{2+}, nor do they require Zn^{2+} to change redox state (6). Most of our mechanistic knowledge of these transporters is based on analyzing structures of bacterial Zn^{2+} transporters (31). That said, recent work has demonstrated that the transport mechanism is highly conserved from mammals to bacteria (32, 33).

There are ten ZnTs encoded in the human genome. Early structural work with the bacterial YiiP transporter facilitated study of human ZnTs in the absence of a crystal structure (34). Later, cryogenic electron microscopy images confirmed many early inferences of human ZnT structure and function (35). ZnT transporters exist as homo- or heterodimers and function to lower the labile cytosolic Zn^{2+} concentration by either moving Zn^{2+} ions into the extracellular space, or into intracellular compartments such as the ER or the Golgi (6). This is accomplished by a conserved zinc/proton (Zn^{2+}/H^{+}) exchange mechanism, which uses the import of one or two extracellular protons to drive Zn^{2+} across the membrane to the extracellular or luminal space (5, 36). Differential expression of the nine ZnT homologs at their cognate intracellular locations can change local Zn^{2+} concentration(37). ZnTs may sense cytosolic Zn^{2+} using their cytosolic C-terminal domains and modulate their own Zn^{2+} transport ability via autoregulation (34).

In contrast to ZnTs, ZIP transporters are much less understood. The fourteen ZIP transporters increase the labile cytosolic Zn^{2+} concentration by importing extracellular Zn^{2+} or exporting Zn^{2+} from the internal organelles. Based on protein alignments, ZIP transporters are much more structurally heterogeneous than the ZnT transporters. A recently solved crystal structure has revealed several insights into the mechanism of the bacterial *Bordetella bronchiseptica* ZIP autoregulation (32, 33). The intracellular C-terminal loop aids in sensing intracellular Zn^{2+} and arrests the transport from the periplasm. In addition, biochemical analysis has revealed that ZIP transporters are much less Zn^{2+} specific, and tend to transport manganese, iron, copper, and cadmium as well (38).

These players set the stage, but we can glean further insight if we perturb Zn^{2+} concentration and watch how these species interact and establish homeostasis after a perturbation in Zn^{2+}. With an increase in intracellular Zn^{2+} concentration, MTF-1 enters the nucleus and binds to the MREs to express high Zn^{2+} response genes such as MTs and ZnTs. These act to sequester the Zn^{2+}, in the case of MTs, or remove the Zn^{2+} from the cytosol in the case of ZnTs. As these downstream effectors act to decrease the amount of labile Zn^{2+} in the cytosol, MTF-1 translocation to the nucleus decreases, in turn decreasing the concentration of downstream effectors, thus forming a negative feedback loop that controls Zn^{2+} homeostasis to its set point. This set point is, among other things, dependent on cellular identity and expression of MTF-1, MTs, and Zn^{2+} transporters (Figure 1.2).

So much is known about the high Zn^{2+} response in metazoan cells, and it is easy to identify the players that respond to increased cytosolic Zn^{2+}. Zn^{2+} deficiency, on the other hand, is a very

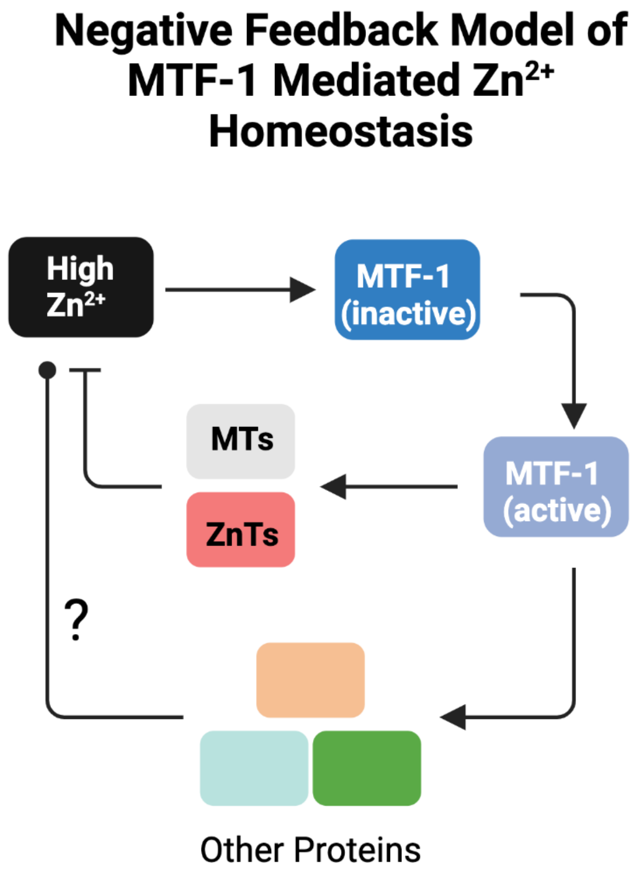

Figure 1.2: A simplified model of the negative feedback loop formed by MTF-1, Zn^{2+}, and MT/ZnT. Zn^{2+} acts to activate MTF-1, which in turn increases expression of metallothionein and ZnT transporters and other genes directly or indirectly related to metal regulation, which act to decrease the amount of labile Zn^{2+} in the cytosol. This decrease in labile Zn^{2+} deactivates MTF-1, forming a negative feedback loop. The cellular concentration of these players defines the intracellular labile Zn^{2+} setpoint.

different story. Although a low Zn^{2+} responsive genomic element has been found in C. *elegans* (39), and a handful of low Zn^{2+}-activated transcription factors have been identified in S. *pombe* (40, 41), no low Zn^{2+} responsive genomic element has been identified in humans. Further, no transcription factor that controls the low Zn^{2+} response has been identified in metazoans that acts in a similar fashion as MTF-1 does in high Zn^{2+} homeostasis. Instead, the mammalian response to low Zn^{2+} is a loose constellation of highly-varied phenotypes with no clear central player (13, 42–44). Identifying the player or players that facilitates the cellular response to Zn^{2+} deficiency is still an active area of research.

Approximately 10% of the genes encoded in the human genome are predicted to encode Zn^{2+} binding proteins (9). This corresponds to almost 3000 different proteins, only a handful of which are involved in regulating Zn^{2+} levels. Zn^{2+} binding can be separated into catalytic and structural binding modes (45, 46). Catalytic Zn^{2+} ions can act as strong Lewis acids, and are usually bound by a mixture of three histidine, aspartic acid, glutamic acid, or cysteine residues and one water molecule that acts in catalysis, as is the case in the protein carbonic anhydrase (45). Structurally, Zn^{2+} ions are tetrahedrally coordinated by cysteine and histidine residues in motifs deemed "Zn^{2+} fingers", due to their secondary structure when bound to a Zn^{2+} ion, and are highly abundant in transcription factors (TFs) and facilitate DNA binding (Figure 1.3A) (46, 47). The apparent dissociation constants (K_ds) of Zn^{2+} to these proteins are on the order of pM to nM, which generally overlaps with the labile Zn^{2+} concentration in cells (Figure 1.3B) (46).

Labile Zn^{2+} can change in response to natural and imposed perturbations (7, 11, 12, 48). These changes in labile Zn^{2+} can then alter mRNA expression, chromatin organization, and transcription factor binding, all on time scales as short as 30 minutes (12, 49). For example, extracellular stimulation of hippocampal neurons with KCl or glutamate leads to an increased Zn^{2+}concentration, and these stimuli lead to differential transcription in bulk RNA-seq, all within 30 minutes of treatment (12). Importantly, the Zn^{2+} dependent transcription in these neurons was

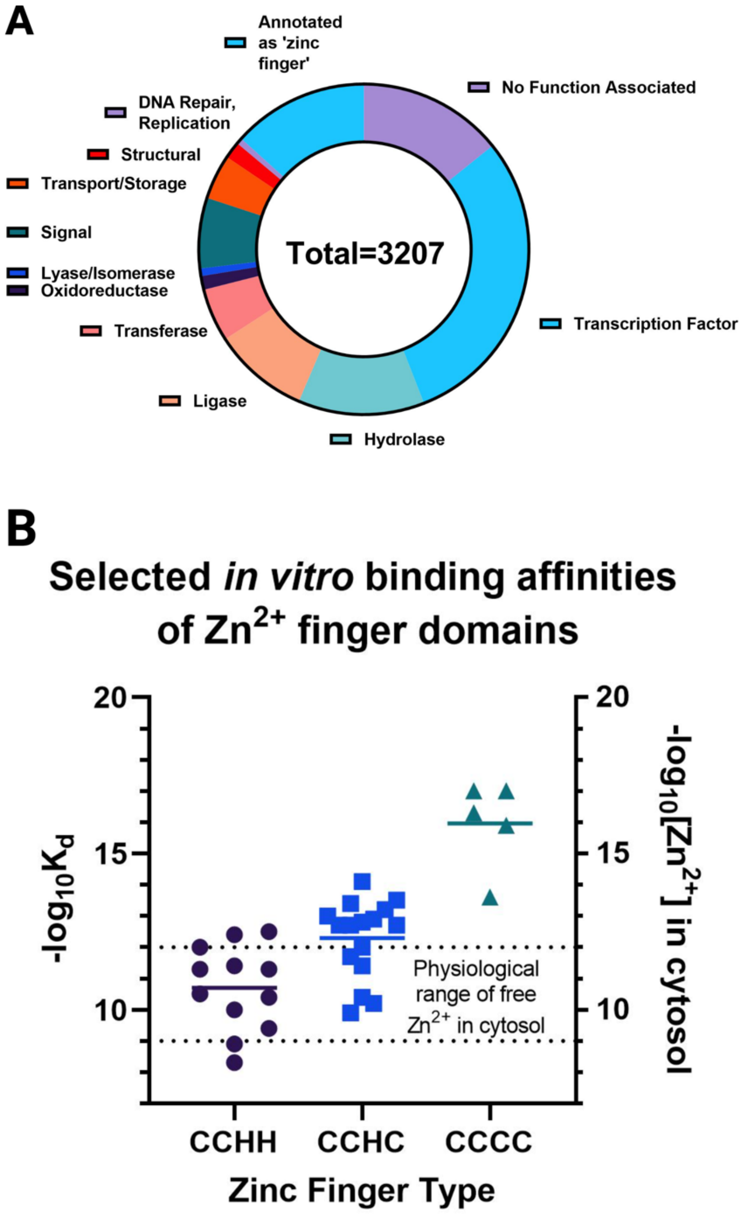

Figure 1.3: Zn^{2+} binding proteins and selected binding affinities of Zn^{2+} finger proteins. (A) Approximate distribution of Zn^{2+} binding proteins involved in different cellular processes. Adapted from (9). (B) Selected binding affinities of different Zn^{2+} finger types with varying H:C ratios on the left vertical axis. Dashed lines indicate the range of cytosolic labile Zn^{2+} in MCF10a cells. Adapted from (10, 46).

blocked upon treatment with TPA, while retaining Ca^{2+} dependent transcription in response to KCl and glutamate. Strong Zn^{2+} deficiency using TPA can increase the diffusion of the Zn^{2+} dependent chromatin architecture protein CTCF within 30 minutes (49). Finally, one group determined that spontaneous and synchronous spikes in labile Zn^{2+} immediately followed Ca^{2+} transients in primary hippocampal neurons, implying that Zn^{2+} can be mobilized in response to cellular signals (50). Work from our lab indicates that short treatment with the Zn^{2+} chelator TPA or excess $ZnCl_2$ can alter chromatin accessibility at promoter and enhancer regions in the genome (51). Together, these observations further strengthen the hypothesis that changes in labile Zn^{2+} can alter chromatin architecture, gene expression, and other intracellular signals.

Through changes in epigenetic markers, one genome is able to supply the information for creating thousands of different cell types, each with its own unique protein, RNA, post-transcriptional and translational modification, and metabolic profile. It stands to reason that the cell type specific expression of Zn^{2+} homeostasis genes can vary within individual cells depending on their environment, and between cell types depending on their identity. Indeed, some tissues accumulate high levels of Zn^{2+}, such as the prostate, the hippocampus, mammary glands, and the pancreas (52, 53). Zn^{2+} can also be concentrated into synaptic vesicles in the hippocampus, or within so-called “zincosomes” in other tissues that require accumulation of the ion (54); however, these studies used a Zn^{2+} binding dye, which is plagued with mislocalization issues and requires further investigation (55). In addition to static accumulation of Zn^{2+} in tissues, flux of the ion across membranes and within the cytosol of cells is required for their function, as is the case with the “zinc spark” in maturing oocytes (56–58). Zn^{2+} homeostasis is significantly altered in cancers (59–61). For example, prostate cancer cells show a decrease in labile and total Zn^{2+} that scales with the grade of the tumor (62). In contrast, breast cancer cells accumulate total Zn^{2+} compared to healthy breast epithelial cells, indicating that there must be some remodeling of the Zn^{2+} homeostatic pathway as cells become cancerous (60, 61). These findings underscore the need to study Zn^{2+} dynamics and homeostasis in an array of cell types, and at a range of subcellular, cellular, and organismal regimes.

1.3 Zn^{2+} in the mammalian cell cycle

For an organism to grow and reproduce, its cells must proliferate in a controlled manner. Uncontrolled cell growth and division is detrimental, and can lead to cancer and other diseases linked to cellular hyperproliferation (63). To control growth and reproduction, life has evolved a series of complex ratchet-like pathways and checkpoints to grow in an ordered fashion and divide successfully (64–66). One complete revolution around this ratchet is called a cell cycle, and can be divided into distinct phases: interphase, which consists of G0, G1, G2, and S-phase and the cell division phase mitosis (Figure 1.4A-B) (64). Each phase is controlled by cyclin-dependent kinases (CDKs), either alone or in combination (67). Their activities throughout the cell cycle are temporally linked with the expression of the cyclins, small activator proteins that increase CDK activity, and CDK inhibitors, such as p16, p21, and p27 that act to decrease CDK activity (Figure 1.4C) (68–71). The expression of cyclins and CDK inhibitors, as well as machinery related to DNA replication and mitosis is controlled by a series of highly conserved transcription factors in the E2F family (72–74). The competition between expression of cyclins and activation of checkpoint signaling tightly controls cell cycle progression (75–77).

After a cell divides, the newborn cell either enters a gap phase called G1 where it prepares for genome duplication, or it enters a reversible resting state called G0 (78, 79). This bifurcation in cell fate is informed by the rate of cyclin D expression in the mother cell, which integrates the mother's mitogen and growth signals (80). This integration determines whether the daughter cell is born in a proliferative hyper-pRb state, or whether it enters a state of low CDK2 activity after division. During G1, a cell prepares its genome for replication by expressing proteins and synthesizing metabolites required for timely progression through S-phase (81). The most crucial

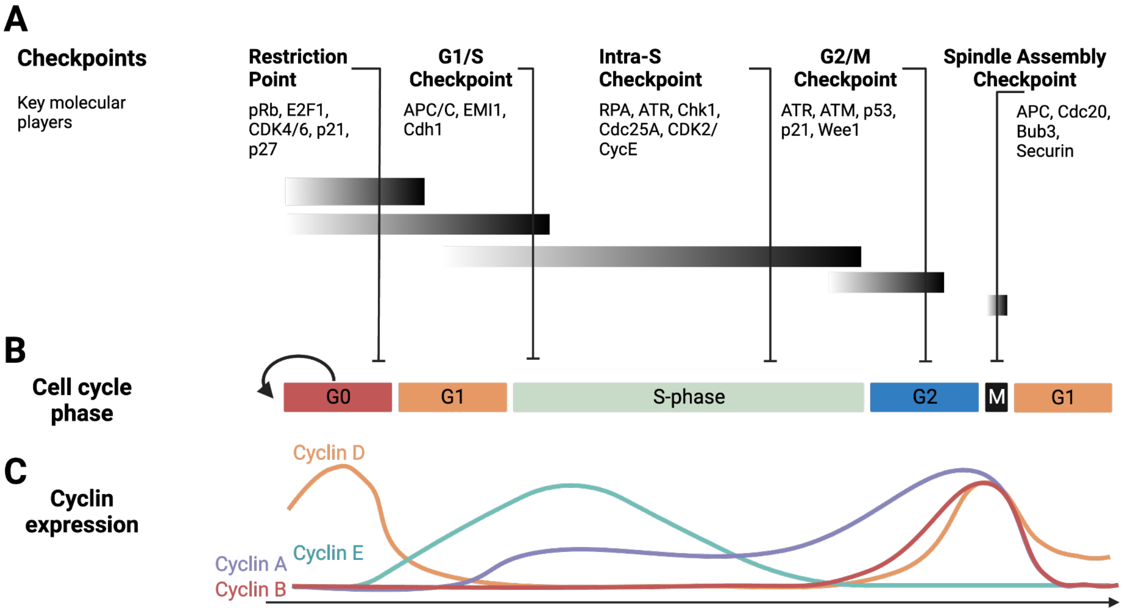

Figure 1.4: Key players in the cell cycle infrastructure. (A-B) The checkpoints of a cell cycle ensure faithful genome duplication and tightly controlled cellular growth. Each checkpoint uses the actions of sensors, regulators, and effector proteins to slow down or stop the cell cycle in response to internal and external stresses. (C) Cyclin expression is correlated to the activity of each cyclin's cognate cyclin-dependent kinase (CDK). Cyclin expression throughout the cell cycle is controlled by a number of transcription factors. The competition between the checkpoints and the cyclins underscores the tight control of each step of the cell cycle. Adapted from (64, 82–84).

aspect of G1 is preparing DNA replication origins in a process called licensing. The cell is tasked with replicating its genome once and only once, which requires infrastructure to ensure faithful genome replication, while minimizing under- or over-replication (81). G1 cells load the pre-replication complex (preRC) onto sites scattered throughout the genome that act as hubs for replication machinery assembly (85–87). At the G1/S transition, cells activate a subset of these origins to start the orchestrated process of DNA replication (88).

Cells walk the razor's edge during S-phase. Unwound DNA opens the genome to insults such as DNA damage and under- or re-replication events (83). Some of these insults come from outside, such as agents that damage DNA or inhibit DNA replication like UV radiation (89). Others are endogenous, such as difficult to replicate sections which take on odd secondary structures that make unwinding or duplicating difficult (90, 91). These pitfalls are collectively called "replication stress" so named because they make the timely completion of S-phase difficult. Cells have evolved several pathways to sense and respond to replication stress. Sensing of single- or double-stranded breaks in DNA is transduced to the DNA damage regulating kinases ATR, ATM, and DNA-PKcs. In turn, these proteins activate the checkpoint kinases Chk1 and Chk2 to signal stress responses and DNA repair gene mobilization (65, 83, 92). ATM and DNA-PKcs signal activation of Chk2, and are active throughout the cell cycle to sense double-stranded breaks (92). ATR activation and subsequent mobilization of Chk1 is mostly constrained to S-phase and G2 (92). Together, these sensors and transducers are integral to the maintenance of genome integrity.

After cells finish replicating their genome, they enter the second gap phase G2, where cells begin to synthesize proteins and ensure the genome is prepared for cell division (93). During G2, any under-replicated DNA is either fixed or protected as the cell prepares to divide (94–96). Concurrently, cells express the machinery that segregates chromosomes and aligns them along the metaphase plate (97, 98). As mitosis commences, cells choreograph an elegant dance that involves several distinct steps: prophase involves breaking down the nuclear envelope, packaging chromosomes into sister chromatids and drawing them close to the line where the cell will eventually divide. Sister chromatids are aligned along this imaginary line during metaphase. Anaphase is when the cell splits its genome along the metaphase plate, ensuring each daughter cell gets two and only two copies of each chromosome. Telophase is when the cell's plasma membrane undergoes scission, the nuclear envelope is reformed, and the chromosomes are unwound again. All of these steps take place within one hour for most noncancerous cells (99).

Zn^{2+} has a crucial yet enigmatic role in regulating the mammalian cell cycle. Several studies have found that Zn^{2+} deficiency is detrimental to several processes spanning the cell cycle phases. Early work by Chesters et al found that treatment with the strong chelator diethylenetriaminepentaacetic (DTPA) to synchronized 3T3 fibroblast cells before entry into S-phase inhibited tritiated thymidine incorporation, and Zn^{2+} resupply was able to rescue this effect (100). This was taken to mean that a process in G1 and at the G1/S transition requires Zn^{2+} for adequate thymidine incorporation and thus, S-phase. After this work, several groups attempted to identify the mechanism by which Zn^{2+} deficiency inhibits DNA synthesis. Another group showed that treatment with the divalent metal ion chelator ethylenediaminetetraacetic acid (EDTA) caused several cell lines to incorporate less radiolabeled thymidine than control cells, and that this was due to decreased thymidine kinase activity (101, 102). Following this, Chesters et al undertook mechanistic work to identify whether cell cycle abnormalities were due to DNA synthesis impairment, or expression of cyclin mRNA, and found that Zn^{2+} deprivation in the form of DTPA treatment impacted cyclin D3 and cyclin E mRNA expression (103). The conclusions from these studies identify that Zn^{2+} deficiency has a measurable impact on cellular proliferation by altering DNA synthesis and cyclin expression.

The above studies have their own limitations. All early work interrogating Zn^{2+} and the cell cycle used population techniques, such as total tritiated thymidine incorporation or Northern blots on populations of synchronized cells. This can introduce cell cycle artifacts and can make interpretation of the data difficult (104, 105). EDTA and DTPA are extracellular divalent metal ion chelators, which act in the growth media of cultured cells to decrease labile metal ions. These chelators are also very nonspecific, binding to any divalent metal cations in the growth media, such as Ca^{2+}, Ni^{2+}, Cu^{2+}, and Zn^{2+}. The Chesters et al study referenced above attempted to circumvent the limitations of DTPA by supplying Zn^{2+}, Fe^{2+}, Co^{2+}, Ni^{2+}, Mn^{2+}, Cd^{2+} with the chelator in a 2:3 stoichiometric ratio; however, many of these cations are highly toxic to cells in culture, which can make interpreting the true cause of the DNA synthesis inhibition problematic.

In 2020, Lo et al took a different approach to study the role of Zn^{2+} in the mammalian cell cycle (13). Using long-term live-cell imaging, flow cytometry, and immunofluorescence imaging, they demonstrated that cells treated with the membrane-permeable Zn^{2+} chelator tris(2-pyridylmethyl)amine (TPA) bifurcated into two populations after division. In the first population, cells entered G0 and were able to re-enter the cell cycle upon resupply of Zn^{2+}. In the second, cells were born with a high CDK2 activity and committed to another cell cycle in a timely manner, only to stall in a hyper-pRb state. These cells were unable to divide again and showed decreased DNA synthesis and increased single-stranded DNA and double stranded break markers. This publication unearthed many buried questions about zinc's role in the cell cycle progression and DNA synthesis and acted as a springboard for using single-cell tools to probe the role of Zn^{2+} in the mammalian cell cycle.

1.4 Zn^{2+} in genome stability

Zn^{2+} and DNA are inextricably linked. Over 700 transcription factors have at least one Zn^{2+} binding motif which is required for DNA binding (47). In addition, many DNA synthesis and DNA damage repair proteins have at least one Zn^{2+} binding motif that is required for protein function (9). The most abundant of these Zn^{2+} binding motifs are the Zn^{2+} fingers (ZFs) (Figure 1.3) (106).

ZFs contain a combination of four cysteine or histidine residues that coordinate with the Zn^{2+} ion; ZFs have K_ds within the physiological range of Zn^{2+} in the cell (46). Given that Zn^{2+} levels can change in response to a host of stimuli, it is possible that population and depopulation of these DNA-binding ZF motifs can alter the function of these proteins and thus genome stability. Further, changes in a cell's oxidative state can lead to oxidation of cysteine residues in Zn^{2+} binding proteins and alter Zn^{2+} affinity to these binding sites. Finally, Zn^{2+} is a cofactor in hundreds of enzymes required for metabolism, and thus it is plausible that changes in labile Zn^{2+} can alter the activity of Zn^{2+}-dependent enzymes required for synthesis of nucleotides and ATP.

ZF domains are found in hundreds of proteins that interact with DNA in some capacity. One stereotypical example is the chromatin remodeling factor CTCF, which contains 11 ZF domains (107). Recent live-cell single-molecule studies of CTCF have demonstrated that chelation of Zn^{2+} with the membrane permeable chelator TPA decreases the dwell time of fluorescently-tagged CTCF in the nucleus (49). This implies that transcription factors are sensitive to changes in cellular labile Zn^{2+}, and that fluctuations in labile Zn^{2+} can alter transcriptional programming and chromatin architecture; however, the direct mechanism by which changes in labile Zn^{2+} can alter chromatin architecture has never been shown.

There are numerous reports of Zn^{2+} deficiency inducing DNA damage and mobilizing DNA damage response (DDR) proteins, in particular p53 and its downstream targets (42–44). Indeed, recent unpublished work revealed that treatment with the membrane permeable chelator TPA for as little as 30 minutes increases chromatin accessibility proximal to p53 binding sites (51). Intriguingly, p53 is a Zn^{2+} binding protein, and the binding affinity of Zn^{2+} to p53 in physiologically relevant conditions sits at a tipping point between population and depopulation of the Zn^{2+} binding site (108). Further, depopulation of p53's Zn^{2+} binding site by mutation or decreased labile Zn^{2+} abolishes DNA binding, so it is logical to assume that p53 is nonfunctional under Zn^{2+} deficient conditions (108); however, this is not necessarily the case. p53 is still active under low Zn^{2+}

conditions, and can still drive the expression of its target genes (109, 110). This is consistent with other research, as p53 target genes are differentially expressed based on the nature of perturbation used to induce their expression (111). That said, one group has identified that Zn^{2+} deficiency decreases the amount of p53 and p21 in cancerous prostate cells through the Akt/Mdm2 signaling axis. In this work, the authors postulated that the Akt signaling axis is responsible for cell survival under conditions of Zn^{2+} deficiency (43). This points to a more complex view of Zn^{2+}-dependent p53 regulation.

Zn^{2+} is often referred to as an antioxidant, mostly due to several studies in which increased oxidative markers were observed upon withdrawal of Zn^{2+} (112). Indeed, a major player in the antioxidant management pathway, superoxide dismutase (Sod1), possesses a Zn, Cu, Mn, or Ni ion that is required for its catalytic function (113–115). It is often speculated that Zn^{2+} chelation can remove this essential metal cofactor from Sod1, thus impairing the protein's dismutase activity and ability to scavenge reactive oxygen species (ROS) (112, 113). In early work from Ho et al, strong chelation with N,N,N′,N′-tetrakis(2-pyridinylmethyl)-1,2-ethanediamine (TPEN) induces single-stranded DNA accumulation and increased nitrite and other oxidative products in rat glioma cells (109). Later work from the same group identified that treatment with TPEN induced expression of p53, as well as increased the concentration of oxidative products in human lung fibroblasts. Further, gene expression analysis after treatment with TPEN showed an increase in genes involved in DNA damage response and oxidative stress (110). Treatment with low Zn^{2+} media without chelator addition showed a different pattern of gene expression. TPEN has a K_d on the order of fM, which is lower than the K_d of most Zn^{2+} binding proteins (116). It is likely that TPEN itself will remove Zn^{2+} from proteins, and thus cause off-target effects as a result. Indeed, we have shown that TPEN is highly toxic to cells and induces cell death at low concentrations (13). This underscores the importance of Zn^{2+} chelator selection.

Finally, every enzyme class has members that require Zn^{2+} for function, including those that process nucleic acids as well as regulators of DNA biosynthesis (45). For example, extracellular purines are required for purinergic signaling, and are processed by a class of Zn^{2+} dependent ectoenzymes that hydrolyze ATP to ADP and AMP (117). *In vitro* studies found that Zn^{2+} depletion of these enzymes inhibits their activity, leading to decreased extracellular ATP clearance and increased purinergic signaling *in vivo*. Another group solved the crystal structure of the CDC7 kinase involved in activating the replicative helicase in S-phase and found that the Zn^{2+} site between the kinase and its coactivator DBF4 is essential for its function (118). Finally, all DNA polymerase complexes are Zn^{2+} binding proteins and, depending on the organism, bind between 2-5 Zn^{2+} ions per complex (119, 120). Treatment of purified DNA polymerases with ortho-phenanthroline, a non-selective chelator of divalent metal cations, inhibits enzyme activity in a dose-dependent manner, indicating that DNA synthesis is a metal dependent process (119). Together, these studies demonstrate that Zn^{2+} is required for several processes that contribute to DNA synthesis. That said, these studies, for the most part, were conducted *in vitro*, requiring further study in cells to determine how Zn^{2+} dependent enzymes are affected by labile Zn^{2+} concentration in their native environment.

1.3 Tools to measure and manipulate cellular Zn^{2+}

1.3.1 Genetically-encoded fluorescent sensors for measuring cellular labile Zn^{2+}

In order to study Zn^{2+} localization, and to quantify changes in Zn^{2+} in response to endogenous and external stimuli, the field of Zn^{2+} biology has developed tools to visualize Zn^{2+} dynamics in living cells (121). The vast majority of these tools take advantage of fluorescence turn-on or Förster resonance energy transfer (FRET) upon binding of Zn^{2+} (8, 122). Each sensor has its own advantages and drawbacks, and proper tool selection requires a deep understanding of the technical consideration of each.

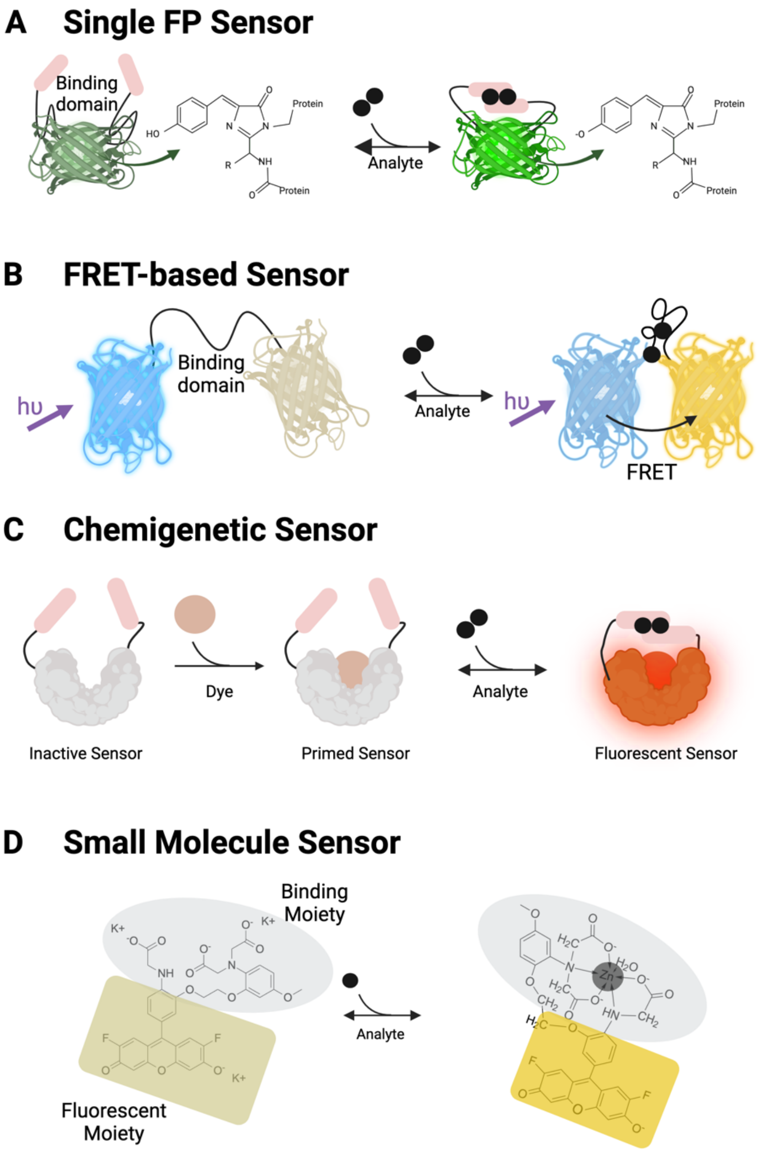

Figure 1.5: Classes of fluorescent biosensors for detecting metal ions in living cells. (A) The mode of operation of a single fluorescent protein (FP) biosensor. The binding domain of the construct reversibly binds an analyte of interest, causing a change in protonation state of the FP's chromophore and turning on fluorescence. (B) The mode of operation of a biosensor that uses Förster resonance energy transfer (FRET). The binding domain of the sensor reversibly binds the analyte and brings the two FPs close together, allowing the donor FP to transfer its excitation energy to the acceptor FP. (C) The mode of operation of a chemigenetic sensor. The inactive sensor is expressed in cells. A fluorogenic dye is added to the cells, covalently binding to the sensor and priming it to fluoresce upon binding of the analyte to the binding domain. (D) The mode of operation of a small molecule sensor. Fluozin-3 is depicted. The sensor is unbound and in a low-fluorescent state. Once the analyte binds to the binding moiety, the fluorescent moiety becomes fluorescent. Structures made with Biorender and ChemBioDraw.

The prototypical single fluorescent protein biosensor consists of a circularly permuted fluorescent protein (FP) attached to a metal sensing domain via a small peptide linker (Figure 1.5A) (123). In a cell, some population of the sensor is in the open, unbound state, where the chromophore of the FP is exposed to the solvent and thus tends to be protonated and weakly fluorescent (124). After perturbation, analyte concentration increases in the cell, and the metal sensing domains on the construct bind and induce a conformational change that excludes the solvent from the core of the fluorophore. This leads to a deprotonation of the chromophore, and a fluorescence increase at the FP's excitation/emission wavelength (125). By changing the metal sensing domains, one is able to change the sensor's specificity to different metals (126, 127). In addition, mutation of the metal binding domains and linker length can alter the sensor's apparent K_d, offering a suite of sensors suited for analytes within multiple quantification ranges (8, 128). Examples of single-FP sensors are GCaMP for measuring intracellular Ca^{2+} and GZnP, ZnGreen, ZnRed and ZIBG1-2 for measuring labile Zn^{2+} (123, 126, 129, 130).

One advantage of the single-FP biosensor is its speed. Since binding and thus deprotonation of the fluorophore is a rapid process, researchers have extensively engineered these sensors to minimize the response time of these sensors. For example, a new variant, jGCaMP8f, has a time to half on ($t_{1/2,\ rise}$) of less than 10 ms; however, optimization on this axis of the chemical space comes at a cost, and generally, the faster the sensor, the lower its sensitivity (127). Another useful attribute of single-FP sensors is their relatively small spectral footprint. Since the fluorescent protein only absorbs and emits at one wavelength, the sensor can be used in conjunction with other sensors to probe changes in multiple analytes or signaling pathways. These sensors come with some significant drawbacks. The most obvious is pH dependence. Since the protonation of the chromophore is a pH dependent process, small changes in pH can also elicit a response from the sensor. It is therefore very important to ensure that perturbations to the cellular system are not significantly changing pH as well as the analyte. Single-FP biosensors expressed in cells can have a widely varying expression level, so researchers normally use either F/F_0 or *z*-score to normalize the signal. While the sensor can be used for quantification in cells, the measurement is more prone to artifacts introduced from construct expression changes, cell movement, and cell thickness (127).

Another class of genetically-encoded metal ion sensors are those that take advantage of Förster resonance energy transfer (FRET), a type of nonradiative energy transfer between dipole-coupled fluorophores (Figure 1.5B) (131). In FRET, a donor FP is excited by its cognate excitation wavelength. The acceptor FP, whose excitation wavelength overlaps with the emission wavelength of the donor FP, is then brought close to the donor. This allows energy to be transferred to the acceptor FP. To determine how close the FPs are to each other, one can calculate FRET efficiency. This can be defined as the rate of FRET transfer divided by the rate of all other decay pathways, or as the quantum yield of the donor in the presence or absence of the acceptor. Since these are often difficult to measure in a biological system, researchers often use sensitized emission, in which energy transfer between the donor FP to the acceptor FP causes fluorescence emission in the acceptor. If a metal binding domain is sandwiched between two FPs that can participate in FRET, then the binding of the metal is able to change FRET efficiency between the FPs, and offers a readout of analyte concentration (8, 132). As with the single-FP fluorescent biosensor, point mutations to the analyte binding region can alter the apparent K_d, and thus change the quantification range of the reporter. Examples of FRET sensors for measuring metal ion concentrations in cells are D3cpv Cameleon for quantifying intracellular free Ca^{2+}, ZapCV2 for quantifying labile Zn^{2+}, and MagFRET for quantifying free Mg^{2+} (8, 133–135).

One advantage of FRET-based biosensors is their sensitivity. FRET efficiency is correlated with the inverse of the radius between the fluorophores to the sixth power, so small changes in distance lead to a dramatic change in FRET efficiency (131). Another advantage of these sensors is their ability to quantify the analyte of interest (8, 122). Since there are two FPs in the construct, expression level of the acceptor FP can be normalized to the acceptor intensity, which can be convenient when studying metal ion concentration in cells of varying thicknesses. If one is to calibrate the sensor by achieving minimum and maximum FRET ratio through a series of in-situ perturbations, they are able to precisely calculate the concentration of free analyte in the cell (136). FRET sensors come with several drawbacks as well. FRET sensors typically suffer from a low dynamic range, and extensive engineering must be done to increase the dynamic range of a sensor. Another inherent issue with this type of sensor is its spectral bandwidth. Since they require two fluorophores, the option to multiplex is limited, especially when using common FP-tags such as CFP and YFP. Finally, detecting FRET requires a unique microscope setup, that can rapidly detect both the FRET channel and the donor channel.

The chemigenetic sensors use dye-binding proteins such as HaloTag or SNAP-tag with a metal binding domain attached to the protein (Figure 1.5C) (137–139). When a fluorogenic dye is covalently linked to the protein, it is primed to become fluorescent (140, 141). As such, when the analyte binds to the sensing domains, the chemical environment around the fluorescent dye is changed, and increases the fluorescence of the dye (138). This design is relatively new, and researchers have only engineered a handful of sensors using a chemigenetic platform. That said, the inherent flexibility in excitation/emission wavelengths allows for more creative uses, such as two-photon microscopy or near-IR microscopy to minimize phototoxicity. Examples of chemigenetic sensors are HaloCamP for measuring free Ca^{2+}, and Halo-MGH for measuring free Mg^{2+} (137, 142).

There are several examples of small molecule sensors for metal ions in biology, specifically Zn^{2+}. Small molecule sensors offer ease of use and high dynamic ranges for fast quantification of metal ions in living systems. The design principle of these sensors is simple: an organic fluorophore, such as fluorescein, coumarin, BODIPY, or rhodamine is coupled to a Zn^{2+} binding group (Figure 1.5D). When the sensor is unbound, the binding domain quenches fluorophore by photoinduced electron transfer (PET), yielding a low fluorescence. When Zn^{2+} binds to the sensor, the binding moiety is unable to participate in PET, leading to decreased quenching of the fluorophore, and fluorescence turn-on. The vast majority of sensors use this mechanism, and therefore are intensiometric. These sensors are useful for quantifying metal ions in solution, as well as identifying changes in extracellular Zn^{2+} in response to a perturbation. Since most of these sensors are charged, they are membrane impermeable, so acetoxymethylester derivatives are available to allow for better cell permeability and therefore ease of use. These sensors have very high dynamic ranges. FluoZin-3, for example, has a reported dynamic range of approximately 200 (143). Other examples of small molecule sensors for Zn^{2+} are TFLZn, ZP1, and ZP4 (144–146).

Small molecule sensors have significant drawbacks. The genetically encoded sensor platform offers control over expression level or subcellular localization by varying the promoter, or adding a nuclear or cytoplasmic localization signal to the genetic construct (147). Small molecules lack any of these control mechanisms, which means their inherent biophysical attributes govern subcellular localization (148). Since engineering these biophysical attributes is only slightly tractable, these sensors are more likely than genetically-encoded sensors to mislocalize to specific organelles which can lead to issues in data interpretation downstream (55). Selecting an appropriate probe concentration is also important, since higher probe concentration in cells can lead to perturbations in the analyte being measured (55). It is important that researchers empirically determine the minimal concentration of probe required to get adequate signal to noise for the target analyte.

1.3.2 Small molecule tools to manipulate labile Zn^{2+} in cells

Researchers have developed several tools to manipulate the levels of Zn^{2+} in cells (116). Broadly, these tools can either increase or decrease the level of labile Zn^{2+} inside of a cell. To

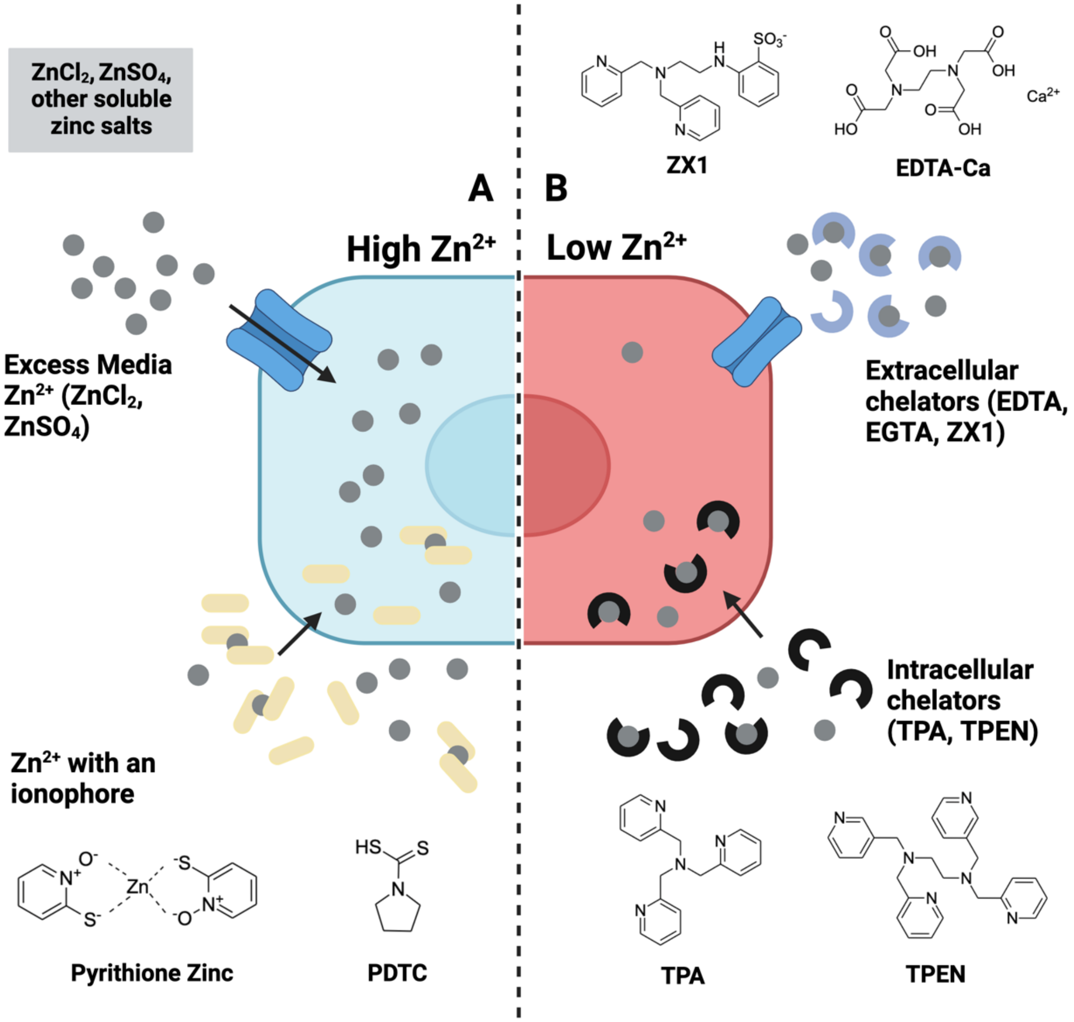

Figure 1.6: Tools to alter labile and total Zn^{2+} in cells. A. Tools to raise intracellular Zn^{2+}. Treatments take advantage of both natural transport mechanisms via ZIPs and ZnTs, as well as using an ionophore to facilitate passive diffusion across the membrane. B. Tools to lower intracellular Zn^{2+}. These take advantage of either sequestering media Zn^{2+} without crossing the cellular membrane, or decreasing intracellular labile Zn^{2+} by chelating both intracellular Zn^{2+} and Zn^{2+} in the media. Structures made with ChemBioDraw.

increase Zn^{2+} inside of a cell, researchers use one of two methods: supplementing the media of the cells with Zn^{2+}, or adding Zn^{2+} along with an ionophore to drive the metal ion across the cell membrane and increase cytosolic Zn^{2+} concentration (13, 136, 149). To decrease Zn^{2+} inside of a cell, researchers use three methods, either alone or in combination: membrane permeable chelators, membrane impermeable chelators, and pretreatment of growth media. Each of these tools has its own considerations, advantages, and drawbacks, depending on the model system and the biological question posed.

To increase cytosolic Zn^{2+}, researchers can add excess Zn^{2+} to the growth media, usually in the form of $ZnCl_2$ or $ZnSO_4$ solutions (13, 44). Since Zn^{2+} import can be modeled by facilitated diffusion of the ligand through the transporter, it is logical to assume that cytosolic Zn^{2+} will increase upon addition of excess Zn^{2+} (Figure 1.6A) (32, 33). Indeed, several groups have identified that cytosolic Zn^{2+} will increase upon addition of extracellular Zn^{2+} (13, 48). The kinetics of this process is slow, however, so adding ionophores can allow more rapid crossing of the cell membrane. One such ionophore is pyrithione, which makes a 2:1 complex with Zn^{2+} and allows the ion to cross all cell membranes, including intracellular membranes (Figure 1.6A) (150). This causes rapid increases in labile cytosolic Zn^{2+}, but can also interfere with redox balance and has been shown to cause cell death and growth inhibitory behavior (149, 151). For long-term experiments, it is advised that researchers use Zn^{2+} supplementation to minimize cell death.

Membrane permeable chelators allow for a rapid removal of labile Zn^{2+} from the entire cell. This is highly advantageous, because Zn^{2+} signaling can occur on the order of minutes and requires a rapid perturbation to study (49, 152). Some membrane permeable chelators are TPEN and TPA (Figure 1.6B). TPEN is widely used in the field of Zn^{2+} biology, owing to its high binding affinity and selectivity for Zn^{2+}; however, TPEN's K_d' for Zn^{2+} is on the order of 0.6 fM, making it stronger than most Zn^{2+} binding proteins and has been shown to remove Zn^{2+} from the cellular proteome (116, 121, 153). Additionally, it is highly cytotoxic in high concentrations and long incubation periods and has been used to study the apoptotic effects of severe cellular reduction in labile Zn^{2+} (154). TPA has a much lower affinity for Zn^{2+}, with a K_d of 10 pM (152). It has been used to study long-term effects of Zn^{2+} deficiency in a cell culture system for several days (13). TPA binds Cu^+ with higher affinity than Zn^{2+}, but in a cellular context, labile Cu^+ is at a much lower concentration than cellular Zn^{2+}, and TPA's phenotypic effects are only reversed by supplementation with Zn^{2+} (13, 152, 155, 156).

Membrane impermeable chelators aim to lower extracellular Zn^{2+} in the hopes of causing a decrease in intracellular Zn^{2+}, or to study paracrine or autocrine signaling. Some examples of membrane impermeable chelators are ZX1, EDTA, and EGTA (Figure 1.6B) (116). An advantage of these chelators is their high metal affinity and rapid kinetics; however, there are drawbacks of using these chelators (157). ZX1 is highly selective for Zn^{2+}, and has rapid kinetics, but there is limited knowledge of off-target effects (116). EDTA and ethylene glycol-bis(2-aminoethylether)-N,N,N′,N′-tetraacetic acid (EGTA) are highly nonselective for Zn^{2+}, and EDTA is often used in conjunction with a Ca^{2+} counterion to decrease this lack of selectivity (158).

An additional approach for manipulating Zn^{2+} concentration is pretreatment of media with Zn^{2+} chelators. Cells require growth factors that are present in serum and other media additives (such as insulin) in order to proliferate, and commercially available serum and insulin often have highly variable amounts of Zn^{2+} (13, 159, 160). Researchers have used Chelex-100, an iminodiacetate-based resin, in order to chelate metal ions from these components (13, 161). That said, Chelex-100 has low metal specificity and will remove several important divalent metal cations such as Ca^{2+}, Fe^{2+}, Cu^{2+}, and Mg^{2+} (13). Another newer method for removing Zn^{2+} selectively is an A12 resin which consists of a Zn^{2+} scavenging protein S100A12 immobilized on a solid support (162). Regardless of what method is used to deplete Zn^{2+} from media, it is crucial that researchers validate the metal ion concentration in their media with an external metric, such as inductively-coupled plasma-mass spectrometry (ICP-MS) (163). Further, it is required that

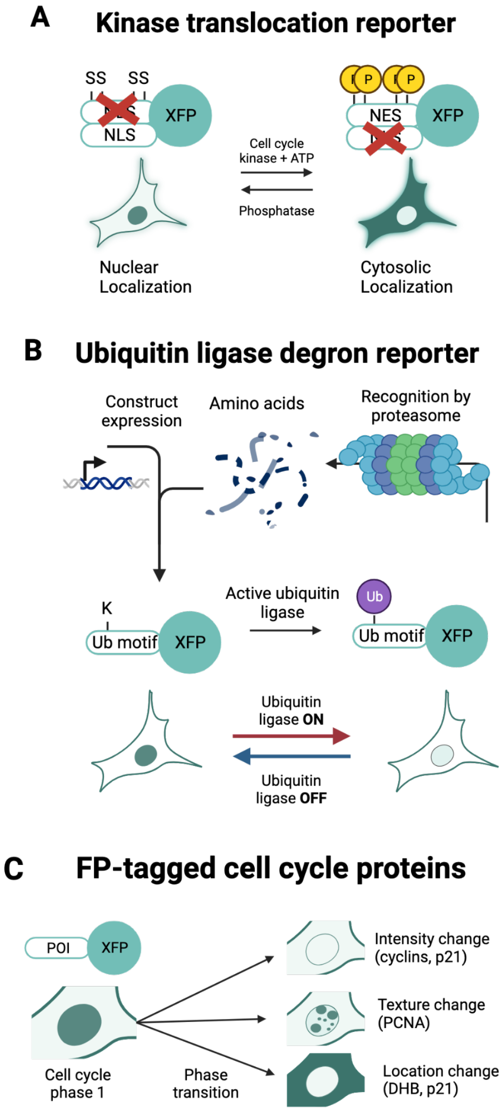

A Kinase translocation reporter

B Ubiquitin ligase degron reporter

C FP-tagged cell cycle proteins

Figure 1.7: Fluorescent tools for probing the mammalian cell cycle in live single cells. (A) Schematic of the design and operation of the kinase translocation reporter (KTR). A fluorescent protein is fused to a kinase recognition domain, which houses a nuclear exclusion signal (NES) and a nuclear localization signal (NLS). Unphosphorylated sensor is localized to the nucleus, and upon phosphorylation by a kinase, translocates to the cytosol. Intensity ratio of cytosol to nucleus yields a readout of kinase activity. (B) Schematic of the design and operation of the ubiquitin ligase degron reporter. A fluorescent protein is fused to a protein fragment containing a ubiquitination motif recognized by a cognate ubiquitin ligase. The ubiquitin ligase targets the fluorescent protein construct for degradation, and signal is decreased. Inactivation of the ubiquitin ligase causes inhibited degradation, and thus the sensor builds up and signal returns. (C) Schematic of FP-tagged cell cycle proteins. Throughout the cell cycle, proteins are created or destroyed, shuttled between the nucleus and cytoplasm, or form foci. FP tagging of cell cycle proteins of interest (POIs) allows for visualization of these changes and thus allows the researcher to infer cell cycle phase.

researchers undertake extensive testing of newly formulated growth media to ensure that any treatments do not interfere with normal function of their model system.

1.4 Fluorescent tools to study the mammalian cell cycle in live cells

Researchers have developed an array of tools to study the mammalian cell cycle. These tools take advantage of the periodic nature of the cell cycle, as well as the robust expression and activity of effector proteins such as ubiquitin ligases and CDKs. Most fluorescent cell cycle tools fall into three categories: the kinase translocation reporters, the degradation sensors, and FP-tagged protein sensors.

Kinase translocation reporters (KTRs) are constructs consisting of a fluorescent protein attached to a kinase pseudo-substrate through a flexible linker (Figure 1.7A) (164). The kinase recognition domain can be interleaved between a nuclear localization signal (NLS) and a nuclear exclusion signal (NES) (78). The kinase recognition domain can also be flanked by a kinase “landing pad” taken upstream or downstream of the cognate kinase recognition site of a natural substrate (165). Phosphorylation of the serine, tyrosine, or threonine in the kinase recognition domain causes an unmasking of the NES (78, 164, 165). This unmasking signals the intrinsic cellular machinery to export the construct from the nucleus to the cytoplasm (166). Upon deactivation of the kinase of interest, phosphatases remove the phosphates from the kinase recognition domain, revealing the NLS, and allowing import into the nucleus (167). The ratio of cytoplasmic signal to nuclear signal yields a readout of kinase activity in that cell.

KTRs can be engineered to recognize one or more cell cycle kinase using either an engineered kinase recognition domain or a fragment from a natural substrate of the kinase of interest (165, 168). One example of this type of sensor is the CDK2 activity sensor that uses a fragment of DNA Helicase B (DHB) linked to a fluorophore. During quiescence, CDK2 activity is low, and the sensor is localized to the nucleus. As the cell progresses through the cell cycle, CDK2 activity builds up and peaks just before mitosis, phosphorylating the sensor and causing a translocation to the cytosol (78). Another example of a KTR used in cell cycle work is the CDK4/6 activity sensor, which is very similar to the CDK2 sensor. In this construct, the DHB fragment is replaced by a fragment of the retinoblastoma protein (Rb) that is recognized by CDK4 and CDK6, with minor contributions from CDK2 (169). After mitosis, cells are either born with high or low CDK4/6 activity. After a time, cells can either remain in this CDK4/6 low state, or they begin building up kinase activity to enter the cell cycle. This sensor therefore allows one to more closely identify entry and exit from quiescence by monitoring decrease and subsequent increase in CDK4/6 activity after mitosis.

KTRs have the advantage of being single fluorescent protein sensors, and thus take up less spectral bandwidth than multiple color sensors. This affords multiplexing with other fluorescent protein biosensors, and thus one can monitor the activities of other signaling pathways in the same cell (164). The nuclear export process is on the order of minutes, which is faster than most cell cycle phase processes, which happen on the order of hours (99, 170). One can therefore identify fluctuations in kinase activity at high temporal resolution.

KTRs have their drawbacks as well. Kinases are notoriously promiscuous. A residue on a protein might be phosphorylated by dozens of other kinases in a process called crosstalk (171). An excellent example of this is the CDK4/6 sensor, whose translocation shows a significant contribution from CDK2 (169). Thus, extensive testing must be done to ensure that the translocation is due only to the kinase of interest while keeping kinase crosstalk to a minimum. This validation can take the form of kinase assays using ^{32}P-labeled ATP, purified kinase and biosensor, or *in cellulo* assays using small molecule inhibitors of the kinase of interest and other kinases with similar recognition motifs (78, 164, 168). Another drawback is more inherent in the translocation readout. Since kinase activity is read out as a ratio of cytoplasmic to nuclear signal, the sensor requires use of an imaging modality and is incompatible with cell sorting or flow cytometry.

Degradation reporters make use of the cyclical activity of ubiquitin ligases throughout the cell cycle. Since each phase of the cell cycle requires different sets of proteins to be expressed and degraded, life has evolved a set of cell cycle specific ubiquitin ligases to target old or unnecessary proteins for degradation as the cell cycle progresses (172, 173). Degradation reporters take advantage of this natural regulation in ubiquitin ligase activity (174). The reporter systems are composed of fluorescent proteins fused with fragments of key cell cycle proteins that contain a ubiquitin ligase target domain (Figure 1.7B). When the ubiquitin ligase is inactive, the chromophore of the fluorescent protein can mature. After a while, expression of the protein will reach a steady state, and the fluorescence intensity will stay relatively constant. Activation of the cognate ubiquitin ligase leads to ubiquitination of the reporter and causes its rapid degradation, thus dropping fluorescence intensity dramatically. The cell is still making the construct, but the degradation of the protein is in kinetic competition with the maturation of the chromophore, so the fluorescence intensity stays near zero. When the ubiquitin ligase is deactivated once again, the construct is no longer degraded and the chromophore is able to mature and produce fluorescence. Identifying the changepoints in the fluorescence over time allows one to identify cell cycle phase boundaries.

The first degradation reporter to be developed was the FUCCI sensor (174). This sensor consists of two different fluorescent proteins tagged to two proteins that are reciprocally targeted by different ubiquitin ligases. The first construct was an mAG fluorescent protein fused to human Geminin protein (aa 1-100). This construct is targeted by the $\mathrm{APC}^{\mathrm{Cdh1}}$ complex and degraded during G1. The second construct was an mKO2 fluorescent protein fused to human Cdt1 protein (aa 30-120). This construct is targeted by the $\mathrm{SCF}^{\mathrm{Skp2}}$ complex and degraded during S-phase and G2. Cells expressing this system will show red fluorescence in G1, and green fluorescence in

S/G2. After several rounds of optimization, the group who originally published the FUCCI sensor published an optimized sensor that further reduced the lengths of fusion proteins and selected new ubiquitination targets to improve response and cell cycle phase resolution. The FUCCI (CA) sensor sought to probe the activity of APC^{Cdh1} and $Cul4^{Dbd1}$ to yield high resolution of the G1/S and S/G2 boundary (175). Almost concurrently, another group developed PIP-FUCCI, which used a shorter ubiquitin ligase target domain called the PIP-box motif from Cdt1, with the human Geminin construct remaining almost identical (176).

Degradation sensors have several advantages. Since these reporters are intensity based rather than localization-dependent, researchers can identify cell cycle phase populations using flow cytometry or cell sorting (175, 177). These reporters also have a high dynamic range, since sensor turn off reaches nearly zero fluorescence when the cognate ubiquitin ligase is active. Finally, these sensors may be used for nuclear tracking, since all constructs contain an NLS (174, 175).

There are drawbacks to degradation sensors. The original FUCCI system was unable to delineate the S/G2 boundary. Further, the signal was fully lost at mitosis, making long-term cell tracking difficult without a nuclear marker (177). Newer iterations of the FUCCI sensor have mostly resolved this issue. Use of this sensor requires an overexpression of fragments of crucial cell cycle proteins such as Cdt1 or Geminin, which can outcompete the endogenous cell cycle protein (176, 178). In addition, these sensors are inherently retrospective, since the changepoint in signal is due to activation or deactivation of the cognate ubiquitin ligase. This means that one cannot know when the cell cycle phase ends until the next begins. Normally this is not an issue with highly proliferative cells in a live-cell imaging context; however, for cells that cycle slowly, or for studying quiescence, long-term live-cell imaging of these populations would be space prohibitive due to large file sizes. Instead, researchers should investigate the use of KTRs or fluorescently tagged cell cycle proteins.

Researchers have also used fluorescent protein-tagged cell cycle effectors to study the cell cycle (64, 71, 179). This consists of fluorescently tagging cell cycle proteins at the N- or C-termini and expressing the construct either from a plasmid or from the endogenous locus in the genome (180). This allows researchers to visualize changes in localization or intensity as a function of the cell cycle (Figure 1.7C). Because of the periodic nature of the cell cycle, one would expect that these fluorescently-tagged cell cycle proteins would show a cyclical change in expression or localization during the cell cycle, and thus yield a readout of the cell cycle phase at a single cell level (177). Further, since each cell will have a different environment and molecular memory, fluorescent tagging of cell cycle proteins, especially when expressed from the endogenous locus, can reveal cell-to-cell variation (96).

One of the first and most popular uses of fluorescently-tagged cell cycle proteins is the histone H2B-XFP fusion protein (181). Although not inherently a cell cycle protein itself, tagging this histone subunit allows for robust visualization of the nucleus throughout the cell cycle, as well as during mitosis. Since almost all cells have at least one nucleus, this allows researchers to track single cells as they move across the field of view and divide (182). Another common FP-tagged cell cycle protein is the proliferating cell nuclear antigen (PCNA) (183). During G1, PCNA shows a diffuse nuclear localization. As cells enter S-phase, the signal moves to distinct nuclear foci that correspond to DNA replication centers. As replication terminates and the cell enters G2, the signal goes back to being diffuse throughout the nucleus. This allows researchers to use the coefficient of variation in nuclear fluorescence intensity to identify the boundary between G1 and S-phase. Finally, researchers have fluorescently tagged the CDK inhibitor p21 (71), the CDK activator cyclin D1 (64), and the stress response transcription factor p53 to visualize their behavior as a function of the cell cycle (179). Using these cell lines in combination with other cell cycle reporters such as KTRs and degradation sensors can yield a rich dataset on how these cell cycle proteins vary across the cell cycle (184, 185).

FP tagging cell cycle proteins has a number of advantages. Expression from a plasmid can yield information about how the protein is processed, degraded, or shuttled throughout the cell. Since much of the intensity or localization changes are due to biochemical processes within the cell, even exogenous expression from a plasmid will reveal cell cycle phase boundaries and cell-to-cell heterogeneity in an apparently homogeneous population (183).

There are technical drawbacks to using FP-tagged cell cycle proteins as well. As mentioned in the previous section on degradation sensors, overexpression of the FP fusion protein is required for enough signal for accurate quantification. This has the potential for causing changes in cell cycle dynamics and can be potentially cytotoxic. This is especially relevant in the case of CDK inhibitors or activators like p21 or cyclin D, whose overexpression is used in molecular biology to cause changes in cell cycle dynamics (186–189). Finally, expression of any construct at high levels can cause a burden on cellular resources, which can in turn inhibit proliferation (190). An option to circumvent these issues is to use a genome editing technique such as CRISPR/Cas9. In brief, the Cas9 protein creates a double-stranded break near a targeted sequence in the genome (191). If a template with homology to the protein of interest and a fluorescent protein gene is supplied, the break repair machinery of the cell can fix the break using the new template (180). Once the cell fixes the break, the cell will be heterozygous or homozygous for the FP-protein fusion. This seems simple enough, but CRISPR/Cas9 genome editing requires rigorous verification that the edit was successful and to ensure that the protein fusion does not interfere with its normal function in the cell (64, 180). Finally, the protein of interest might be expressed at such a low level that the fluorescence of the fusion might have poor signal to noise, as is the case with p53 (179, 180). This limits the technique to a subset of proteins that are known to have a high dynamic range of expression throughout the cell cycle. This issue can be partially circumvented by using newer, brighter FPs such as mNeonGreen or mTurquoise2 in the fusion (192, 193), but these workarounds still rely on adequate expression of the protein of interest.

1.5 Introduction to This Thesis

The goal of my thesis work was to define the role of Zn^{2+} throughout the mammalian cell cycle, primarily through the lens of single-cell tools. Chapter 2, "Human cells experience a Zn^{2+} pulse in early G1," identifies whether naturally cycling cells show changes in labile Zn^{2+} throughout the cell cycle. It also aims to determine the effect of knocking down a key transcription factor involved in the high Zn^{2+} response in cells. This study uses the genetically encoded fluorescent biosensor ZapCV2 to measure free Zn^{2+} in naturally proliferating cells, and the nuclear marker H2B-HaloTag to track cells in real time. After tracking cells, a postdoctoral fellow and I found that cells increase labile Zn^{2+} in the minutes leading up to mitosis, and peaks at approximately one hour into the daughter cell G1, which we deemed the Zn^{2+} pulse. We also determined that knockdown of the metal responsive transcription factor MTF-1 increases resting labile Zn^{2+} and modulates the size of the Zn^{2+} pulse. Finally, we found that cells require a minimal and maximal free Zn^{2+} concentration in order to proliferate, and cells outside of this window pause proliferation until Zn^{2+} levels are restored. This work shines a light on the regulation of the mammalian cell cycle by Zn^{2+}, and the natural rhythmic fluctuations in Zn^{2+} levels and other metal ion levels as a whole.

In addition to determining the natural fluctuations in Zn^{2+} throughout the cell cycle, I wanted to assess the ramifications of transient Zn^{2+} deficiency on cellular proliferation and integrate decades of research that have pointed to DNA synthesis impairment as a driver of Zn^{2+} deficiency induced quiescence. Chapter 3, "Transient Zn^{2+} deficiency induces replication stress and informs the proliferation of daughter cells," aims to identify the Zn^{2+} requirements of the mammalian cell cycle and identify the consequences on Zn^{2+} deficiency on proliferation through the lens of DNA replication stress. I found that Zn^{2+} deficiency during G1 and across the S/G2 transition has little effect on the mother cell's S-phase, but Zn^{2+} deficiency across the G1/S transition and in S-phase causes strong impairment of mother S-phase progression. In addition, I found that acute Zn^{2+}

deficiency inhibits DNA synthesis rate, and that this impairment can be rescued with resupply of Zn^{2+}. This DNA synthesis rate impairment is accompanied by simultaneous accumulation of the replication stress marker RPA2, which is also fully reversible upon resupply of Zn^{2+}. These impairments are not due to DNA origin underlicensing, nor are they due to Chk1-dependent inhibition of origin firing, nor are they due to double-stranded breaks. Finally, I found that Zn^{2+} deficiency during the mother cell's S-phase causes daughter cells to temporarily withdraw from the cell cycle. This withdrawal is accompanied by sustained expression of the tumor suppressor gene p21, which acts to inhibit proliferation. Together, this is the first evidence that mild Zn^{2+} deficiency causes replication stress during S-phase, and that this replication stress transmits to daughter cells to inform their proliferation.

Chapter 2: Human cells experience a Zn^{2+} pulse in early G1

2.1 Publication Status

Rakshit, A.; Holtzen, S. E.; Lo, M.L.; Conway, K.A.; Palmer, A.E. “Human cells experience a Zn^{2+} pulse in early G1.” *Cell Reports,* 42(6): 112656, June 17, 2023

A.R and S.E.H contributed equally to this work. Conceptualization, Methodology, A.E.P., M.N.L., A.R., S.E.H.; Investigation, A.R. S.E.H, M.N.L., K.A.C.; Writing – Original Draft, Writing – Review and Editing A.E.P., A.R., S.E.H.; Formal Analysis, A.R. and S.E.H.; Software, S.E.H; Funding Acquisition, Supervision, Project Administration, A.E.P.

2.2 Abstract

Zinc is an essential micronutrient required for all domains of life. Cells maintain zinc homeostasis using a network of transporters, buffers, and transcription factors. Zinc is required for mammalian cell proliferation and zinc homeostasis is remodeled during the cell cycle; however, whether labile zinc changes in naturally cycling cells has not been established. We use genetically encoded fluorescent reporters, long-term time-lapse imaging, and computational tools to track labile zinc over the cell cycle in response to changes in growth media zinc and knockdown of the zinc regulatory transcription factor, MTF-1. Cells experience a pulse of labile zinc in early G1, whose magnitude varies with zinc in growth media. Knockdown of MTF-1 increases labile zinc and the zinc pulse. Our results suggest that cells need a minimum zinc pulse to proliferate and that if labile zinc levels are too high, cells pause proliferation until labile cellular zinc is lowered.

2.3 Introduction

Zinc (Zn^{2+}) is the second most abundant transition metal ion in mammals and is an essential micronutrient crucial for growth, cell differentiation, and cell proliferation (6, 194). At the molecular level, Zn^{2+} is an essential cofactor for over 2500 proteins (9) and plays fundamental roles in metabolism (195–197), DNA synthesis (13, 100, 101), and transcriptional regulation (12, 49). It is now well established that Zn^{2+} is required for cell proliferation (13, 194). Early work by Chesters et al suggested that Zn^{2+} is necessary for the G1 to S transition (198) and for DNA synthesis in S-phase (100, 199). However, subsequent studies contradicted these conclusions, finding that after cells cross the restriction point in G1, they don't need Zn^{2+} until the G2/M transition (103). The contradictory findings of these early studies may have been confounded by long-term incubation with high concentrations of Zn^{2+} chelators, drugs, and cell synchronization, which often activates stress signaling pathways (79, 104). More recently, Lo et al showed that conditions of mild Zn^{2+} deficiency cause cells to either exit the cell cycle and go quiescent or stall in S-phase (13). Such studies suggest that Zn^{2+} may be required during multiple phases of the cell cycle, yet an open question is whether labile Zn^{2+} itself varies over the course of the cell cycle and, if so, how proteins responsible for preserving Zn^{2+} homeostasis might influence Zn^{2+} dynamics.

Mammalian cells use an elegant system of highly-coordinated proteins to control cellular uptake, organelle distribution, and elimination of excess Zn^{2+} across the plasma membrane to maintain intracellular Zn^{2+} homeostasis (5, 22, 200, 201). Transporters such as ZIP (*Slc39a1-14*) and ZnT (*Slc30a1-10*) are responsible for the import and export of Zn^{2+} across organelle and plasma membranes (5, 22, 200, 201). Metallothioneins (MT) buffer intracellular Zn^{2+} and help maintain the labile Zn^{2+} pool (16, 22). Finally, the metal regulatory transcription factor-1 (MTF-1) regulates labile Zn^{2+} levels by adjusting the expression of the exporters ZnT1, ZnT2, and the cellular buffer MT[23,24]. Multiple studies have suggested that disruption of zinc-regulatory proteins can attenuate proliferation (59, 202, 203). For example, downregulation of MT-2A and knockdown of zinc transporters ZnT1, ZnT6, and Zip11 reduce proliferation of MCF-7 breast cancer cells (203) and *Capan-1* pancreatic cancer cells (59), respectively. Furthermore, studies have shown that the levels and localization of zinc regulatory proteins, particularly MT, vary in a cell cycle-dependent manner. MT levels are 3–5 fold higher in proliferating human Chang hepatocytes (CCl-13) (204). In HT-29 cells, MT levels oscillate during the cell cycle, reaching a maximum in late G1 phase and at the G1/S transition (26). Finally, MT was shown to translocate to the nucleus when cells transition from quiescence to G_1 and again early in S phase (26). Combined, these studies suggest that mammalian cells remodel Zn^{2+} homeostasis to meet different Zn^{2+} requirements during different phases of the cell cycle.

While mammalian cells contain hundreds of micromolar total Zn^{2+}, most of it is bound to proteins, such that the labile pool is on the order of hundreds of picomolar (122, 132, 136). To our knowledge, there have only been two studies that have explored whether Zn^{2+} levels change during the mammalian cell cycle. The first study used X-ray fluorescence microscopy (XRFM) to show that total cellular Zn^{2+} increases over 3-fold in mitotic cells, perhaps to help daughter cells prepare for Zn^{2+} requirements (205). XRFM is powerful for revealing a spatial map of total (but not labile) zinc in fixed, frozen, or air-dried cells. In the second study, Li and Maret used the fluorescent reporter FluoZin-3 to measure labile Zn^{2+} in a population of PC-12 cells in a cuvette after release from serum starvation (48). Their study showed two peaks in Zn^{2+} at 3 and 12 hours after release from synchronization. These peaks map roughly to early G1 and the G1/S transition in PC-12 cells, although an independent measurement of cell cycle was not carried out in this study. These studies represent an important first step in revealing fluctuations in the Zn^{2+} during the cell cycle. However, there are also limitations to these studies. The XRFM study focused on naturally cycling cells, but the technique is not compatible with real-time measurement in live cells. On the other hand, the FluoZin-3 study measured labile Zn^{2+} in live cells, but it relied on bulk analysis of serum-starved cells which masks the heterogeneity inherent in individual cells and disrupts their natural cell cycle tempo.

Here, we overcome limitations associated with previous studies using high throughput long-term imaging and computational single-cell image analysis to track individual cells in a naturally cycling population. We use a genetically encoded fluorescent Zn^{2+} sensor to measure labile Zn^{2+} levels in the cytosol and nucleus of asynchronously cycling cells expressing a fluorescent histone 2B marker to aid in cell tracking and mitosis detection. We identified a labile Zn^{2+} pulse immediately following mitosis that lasts for two hours into early G1 phase. The magnitude of the Zn^{2+} pulse can be modulated by the total Zn^{2+} in the media and knockdown of the Zn^{2+} regulatory transcription factor, MTF-1. Knockdown of MTF-1 also results in increased cytosolic labile Zn^{2+} and impaired reestablishment of homeostasis after elevation of Zn^{2+} in the growth media. Our results show that a Zn^{2+} pulse that is too low or too high is correlated with impaired proliferation, suggesting that Zn^{2+} levels and dynamics are an important part of cell cycle regulation.

2.4 Results

2.4.1 Genetically encoded FRET-based sensor ZapCV2 illuminates intracellular Zn^{2+} dynamics

Previous work has established zinc as essential for cell proliferation, and that withdrawal of zinc ions (Zn^{2+}) induces quiescence in MCF10a cells. We sought to recapitulate these observations in naturally cycling MCF10a cells expressing the genetically encoded cytosolic zinc sensor ZapCV2 to examine whether there are changes in the labile zinc pool over the cell cycle. The ZapCV2 sensor is composed of a zinc binding domain sandwiched between ECFP and a circularly-permuted (cp) Venus (Figure 2.1A). The sensor can be targeted to the cytosol with a

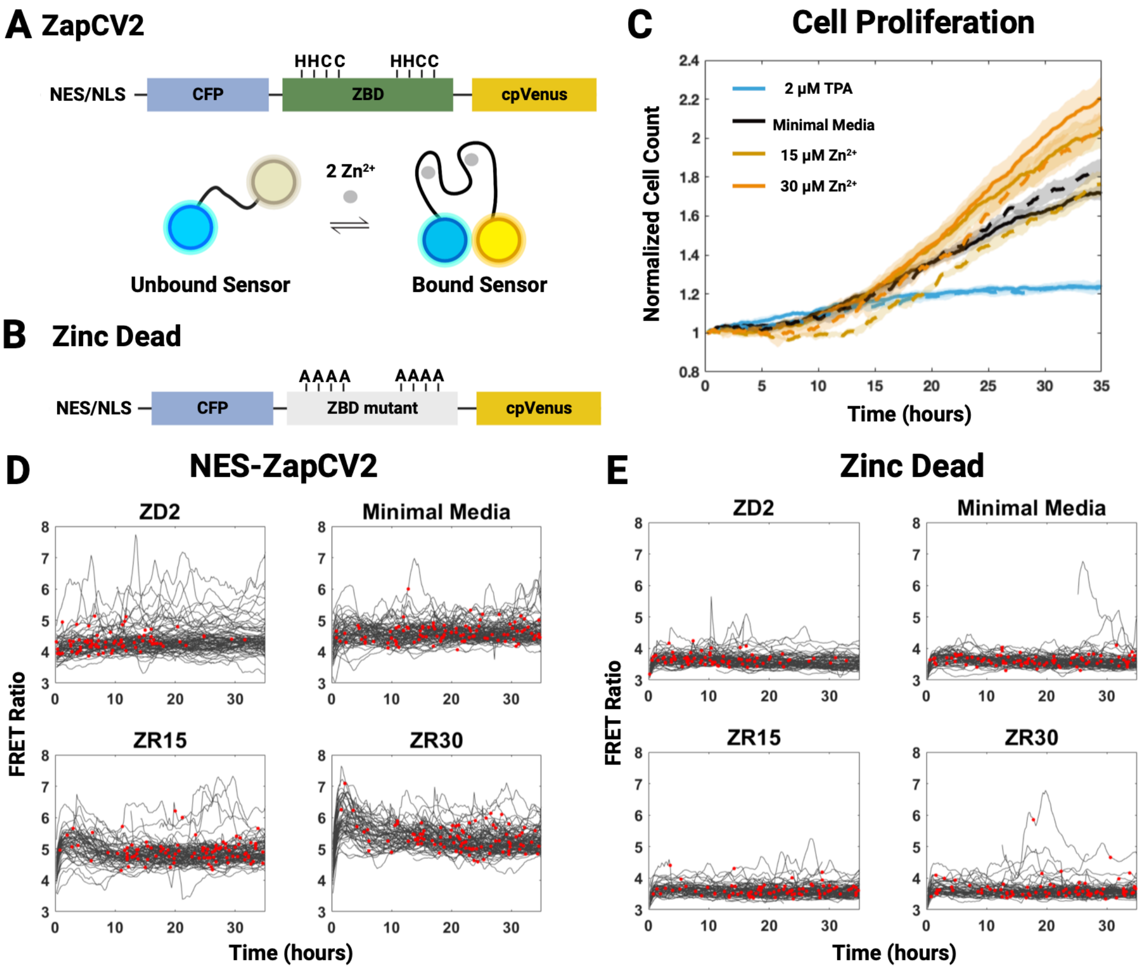

Figure 2.1: Zn^{2+} levels influence cell proliferation over time. (A and B) Diagram of the ZapCV2 zinc-binding and zinc-dead sensors. Zinc-binding residues and alanine mutants are labeled. Illustration of sensor binding to zinc. Zinc binding induces a conformational change, which leads to increased FRET. (C) Proliferation of cells expressing the cytosolic zinc sensor ZapCV2 (solid line) and zinc-dead sensor (dashed line) in different medium conditions over 35 h. Each line represents the average of four wells normalized to initial plating density. Shaded areas represent standard deviation. (D and E) Single-cell FRET ratios of MCF10a cells expressing either NES-ZapCV2 or zinc-dead sensor. Red dots indicate a mitosis event. Each plotted trace must contain at least one mitosis event. 100 random traces across four wells are plotted in each condition.

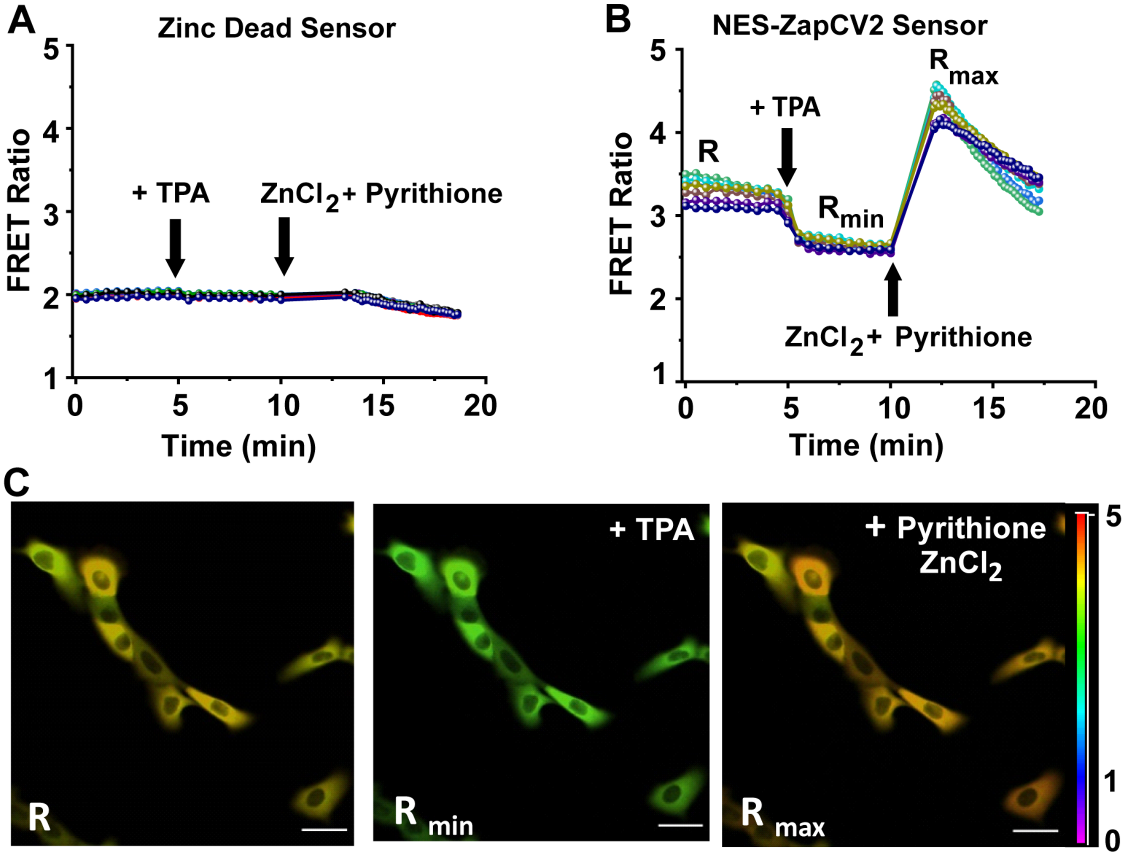

Figure 2.2: In situ calibration of genetically encoded FRET based sensors. Panel (A) and (B) depict six Zn^{2+} calibration traces (FRET ratio vs. time) from a single FRET calibration experiment performed on MCF10a cells stably expressing H2B-mCherry and the NES-Zinc-dead sensor, and H2BmCherry and the NES-ZapCV2 sensor, respectively. Cells were grown in MM for 24h then the media was changed to HHBSS buffer before the calibration experiment. Black arrows indicate addition of (i) 50 µM TPA at 5 min; and (ii) 104 nM buffered Zn^{2+} + 0.001% saponin + 750 nM pyrithione at 10 min. R, Rmin and Rmax represent the average resting, minimum and maximum FRET ratio (Intensity of CFP$_{ex}$ YFP$_{em}$ /Intensity of CFP$_{ex}$ CFP$_{em}$) from a single cell. Those traces were generated by placing a ROI on individual cells and following FRET ratio over time upon subsequent addition of TPA and Zn^{2+}/pyrithione or using our MATLAB R2020A (Mathworks) pipeline for automated cell segmentation and tracking, as well as methods for calculating the FRET ratio as described in Lo, et. al. (C) Fluorescence images of cells displaying resting (left), minimum (center), and maximum (right) FRET ratios acquired during FRET sensor calibration experiment (Objective 20X, scale bar: 100 µm). Images are pseudo-colored with rainbow gradient LUT over the following ratio range: 0 – 5.

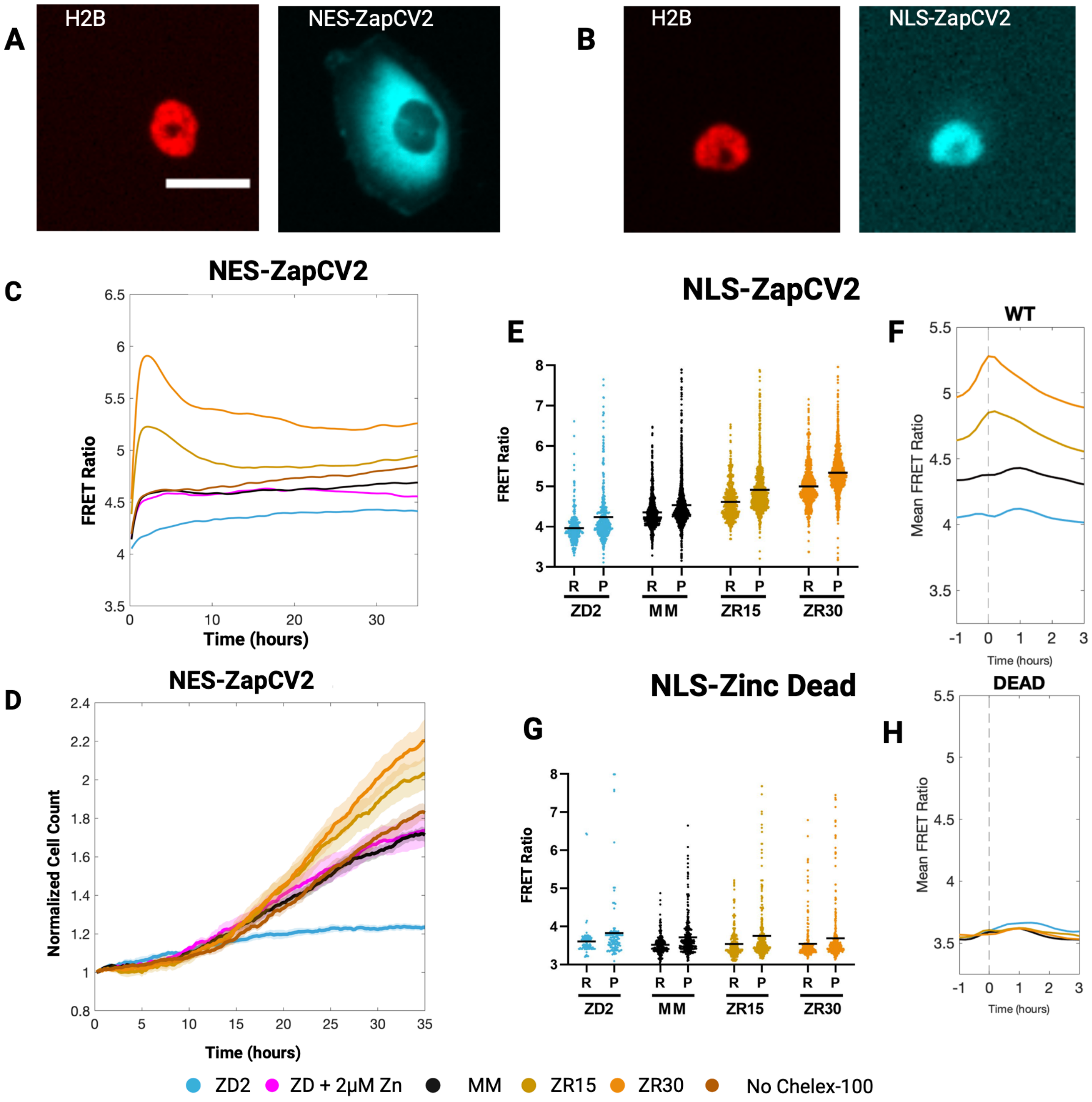

Figure 2.3: Characterization of MCF10a cells expressing H2B-mCherry and NES-, NLS-ZapCV2 or NLS-zinc dead construct. (A,B) Fluorescent images of MCF10a cells expressing H2BmCherry and NES-ZapCV2 (A) and NLS-ZapCV2 (B). Left: mCherry channel showing H2B nuclear marker. Right: FRET channel showing ZapCV2 with either a nuclear localization signal (NLS) or a nuclear export signal (NES). Scale bar = 12 µm. (C) Mean FRET ratio traces of cells grown in media with different amounts of total zinc. (D) Proliferation of cells grown in different zinc media. (E) Resting and peak FRET ratios of cells expressing NLS-ZapCV2 as described in Figure 2E. R: resting FRET ratio, P: peak FRET ratio. Each dot represents a single cell. The black line represents the mean. F) Average FRET ratio traces of cells expressing NLS-ZapCV2 aligned to mitosis (n=300-500 cells, one biological replicate). Dashed line indicates mitosis. G) Resting and peak FRET ratios of cells expressing NLS-zinc dead as described in Figure 2E. H) Average FRET ratio traces of cells expressing NLS-zinc dead aligned to mitosis (n=300-500 cells, one biological replicate). Dashed line indicates mitosis.

nuclear exclusion signal (NES-ZapCV2) or the nucleus with a nuclear localization signal (NLS-ZapCV2). Zn^{2+} binding induces a conformational change increasing Förster resonance energy transfer (FRET) from ECFP to cpVenus. The FRET/CFP ratio is proportional to the labile Zn^{2+} concentration in the compartment to which the sensor is targeted. We also developed a mutant ZapCV2 sensor, in which all the cysteine and histidine residues in the zinc binding domain were replaced with alanine, abolishing Zn^{2+} binding (Figure 2.1B). This "zinc dead" sensor does not respond to perturbations of the labile Zn^{2+} pool (Figure 2.2).

First, we sought to identify the global effects of Zn^{2+} availability on proliferation. We treated cells with media containing several different concentrations of Zn^{2+} and monitored proliferation over multiple days. Our minimal media (MM) contains 1.46 μM total Zn^{2+}, which is enough to sustain proliferation[10]. We then added 15 μM or 30 μM $ZnCl_2$ for a zinc rich condition (ZR15, ZR30), or 2 μM tris(2-pyridylmethyl) amine (TPA) for a zinc deficient (ZD2) condition. We have previously shown that the ZD2 condition lowers labile zinc to ~1 pM and the ZR30 condition increases the labile zinc to 210 pM. We imaged asynchronously cycling cells in each condition for multiple days. These time-lapse images were segmented and tracked via the H2B-mCherry nuclear marker using an automated live cell tracking pipeline EllipTrack (182). After data extraction, we counted the number of segmented ellipses in each frame and normalized this count to the first frame. We observed that the zinc deficient condition (ZD2) showed reduced proliferation when compared to MM (Figure 2.1C), consistent with previous observations of zinc deficiency impairing proliferation. To differentiate loss of proliferative ability from loss of tracking due to cell death, we plotted mitosis events and the FRET ratio of all conditions. Mitosis events dramatically decreased after 15 hours in ZD2 media without significant loss of single cell tracks, confirming that this observation is indeed due to induction of quiescence and not cell death (Figure 2.1D, 2.1E). The loss of proliferation is not due to off-target effects of TPA, since addition of equimolar $ZnCl_2$/TPA did not inhibit proliferation (Figure 2.3). The high zinc conditions (ZR15, ZR30) showed enhanced proliferation and an increased FRET ratio, indicating increased labile cytosolic Zn^{2+}. Finally, cells expressing the zinc dead sensor showed a lower FRET ratio that did not change with Zn^{2+} in the media and these cells showed a similar overall pattern of proliferation (Figure 2.1C, 2.1E). These data confirm that Zn^{2+} levels influence both cell proliferation and labile cytosolic Zn^{2+} and that sensor expression does not perturb normal cellular proliferation.

2.4.2 There is a Zn^{2+} pulse after mitosis that correlates with both nutritional and labile Zn^{2+}

The single-cell FRET traces in Figure 2.1D suggest that the labile Zn^{2+} pool may fluctuate over the cell cycle. However, since the population is asynchronously cycling, it is difficult to evaluate changes in Zn^{2+} at specific cell cycle phases. In order to extract salient information about Zn^{2+} dynamics during the cell cycle, we aligned single-cell traces *in silico* to mitosis events detected by the cell tracking software. *In silico* alignment revealed that the FRET ratio and hence average labile Zn^{2+} is correlated with the amount of Zn^{2+} in the growth media (ZD2 has the lowest FRET ratio, ZR30 has the highest resting FRET ratio) (Figure 2.4A). The zinc dead sensor did not show the commensurate FRET ratio increase with increased media Zn^{2+} (Figure 2.4B).

Close analysis of Zn^{2+} dynamics around mitosis reveals a peak in FRET ratio that persists for 1.5-2 hours into G1 and occurs immediately following the spike in H2B-mCherry that denotes a mitosis event (Figure 2.4C). There is a slight FRET change in the zinc dead sensor, but this does not correlate with the amount of Zn^{2+} in the media (Figure 2.4D). To define the change in FRET ratio at the peak of the pulse, we calculated the average FRET ratio of the track two hours approaching mitosis, referred to as the “resting FRET ratio (R)”, and the maximum value within the first two hours of mitosis, referred to as the “peak FRET ratio (P)” (Figure 2.4C). The peak FRET ratio was positively correlated with both the labile Zn^{2+} pool and nutritional Zn^{2+} (Figure 2.4E). Additionally, the difference between the peak and resting FRET ratio increased with higher Zn^{2+}. In contrast, the zinc dead sensor did not show an increase in resting or peak FRET ratio in

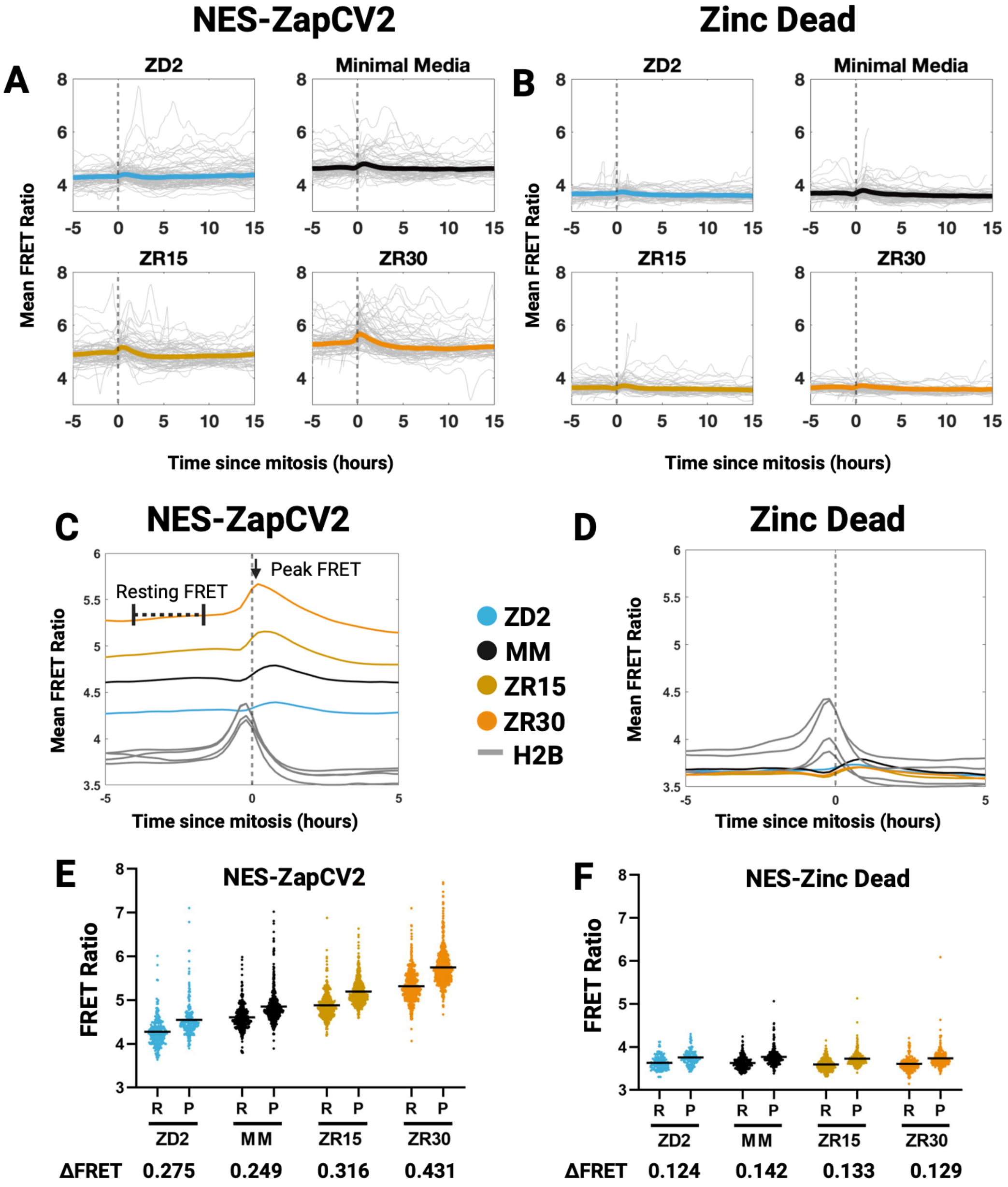

Figure 2.4: Tracking of labile zinc over the cell cycle reveals zinc dynamics around mitosis that is modulated by nutritional zinc. (A and B) Single-cell traces of cells expressing either NES-ZapCV2 or the NES-zinc-dead sensor after alignment to mitosis are represented in gray (n = 100 randomly selected cells per plot). Average FRET ratios of these traces are overlaid in color. (C) Averaged FRET ratio of NES-ZapCV2 and H2B-mCherry intensity in a 10 h window around mitosis. Resting FRET is calculated by averaging ten frames (4 h–2 h) approaching mitosis. Peak FRET is the maximum value within ten frames (2 h) of mitosis. (D) Plot as shown in (C) with cells expressing the NES-zinc-dead sensor. (E and F) Values of resting FRET (R) and peak FRET (P) in both zinc-binding and zinc-dead sensors. Mean values are shown as black bars. Each dot represents an individual cell track (n > 100 for each condition, one of three biological replicates is shown). Quantification of FRET change (ΔFRET) between resting and peak is shown below each group.

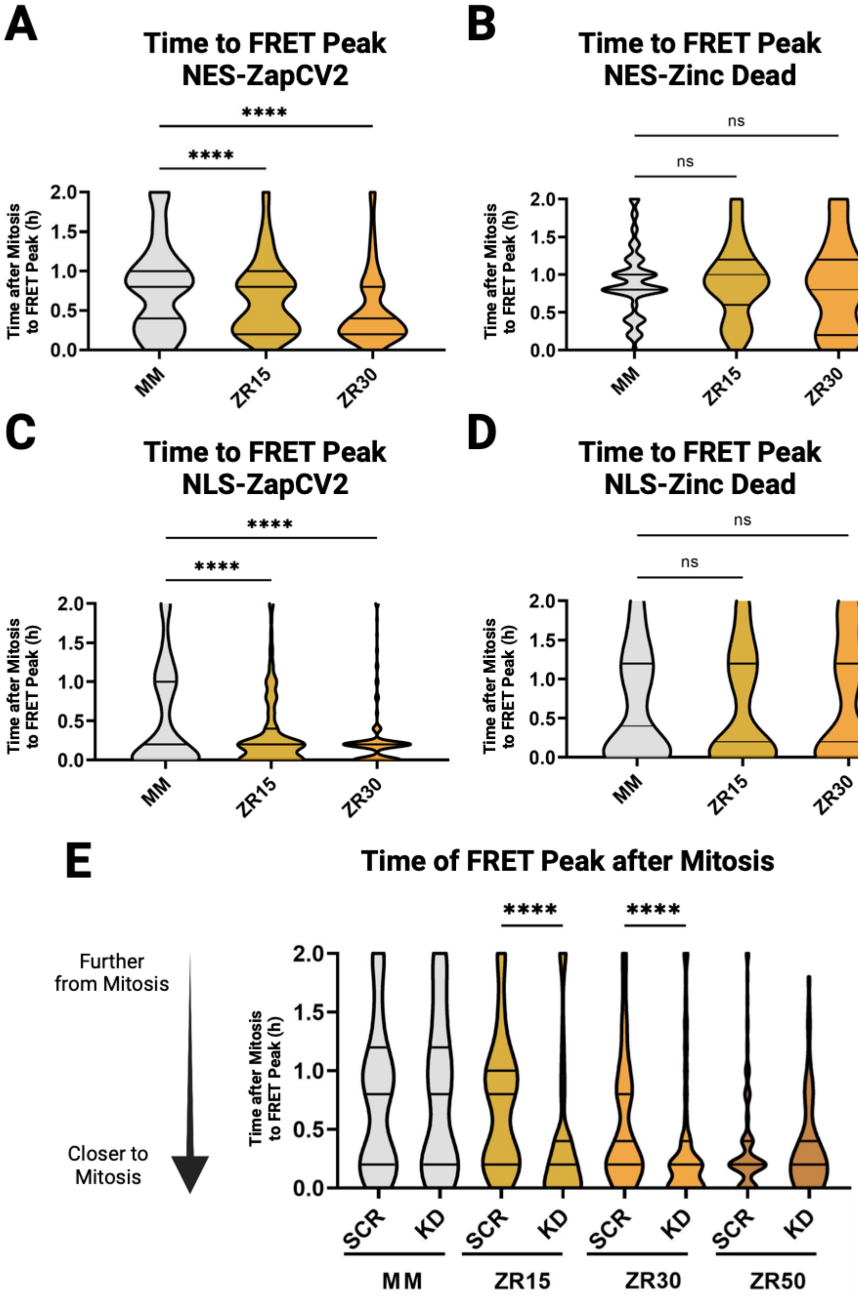

Figure 2.5: Available zinc and MTF1 levels influence time to peak FRET after mitosis. (A, B) Violin plots showing time after mitosis of FRET peak in cells grown in different zinc conditions and expressing NES-ZapCV2 sensor or NES-zinc dead sensor. (C, D) Violin plots showing time after mitosis of FRET peak in cells grown in different zinc conditions and expressing NLS-ZapCV2 sensor or NLS-zinc dead sensor. (E) Violin plots showing time after mitosis of FRET peak in cells grown in different zinc media. Cells in this experiment were expressing NES-ZapCV2, and either an MTF1 shRNA, or a scrambled shRNA. Comparisons conducted with one-way ANOVA, with follow-up t-tests, which are plotted. * indicates $p < 0.05$, ** indicates $p < 0.01$, *** indicates $p < 0.001$, **** indicates $p < 0.0001$. NS indicates $p > 0.05$. Horizontal lines in violin plots represent median and first and third quartiles.

differential Zn^{2+} conditions (Figure 2.4F). Together, these results indicate that nutritional Zn^{2+} influences labile Zn^{2+} levels and the magnitude of the Zn^{2+} pulse after mitosis.

We also examined the labile Zn^{2+} pool in the nucleus with a nuclear localized zinc sensor (NLS-ZapCV2). Figure 2.3 shows fluorescence images of NES- and NLS-ZapCV2, along with H2B-mCherry. Figure 2.3 also shows that nuclear Zn^{2+} undergoes a transient increase immediately following mitosis, and the magnitude of the pulse correlates with labile Zn^{2+} and the amount of Zn^{2+} in the media. The nuclear localized zinc dead sensor did not show the same rise in FRET ratio, confirming that the FRET ratio increase corresponds to an increase in labile nuclear Zn^{2+}. We also observed that the Zn^{2+} pulse peaked earlier when the concentration of labile Zn^{2+} and Zn^{2+} in the media increased (Figure 2.5A, 2.5C). In contrast, the cytosolic and nuclear zinc dead sensor did not show a peak shift with increased Zn^{2+}, indicating that this shift is due to Zn^{2+} dynamics after mitosis and not volumetric changes during mitosis.

2.4.3 MTF-1 knockdown results in higher levels of labile Zn^{2+}

After identifying a pulse of labile Zn^{2+} early in G1, we set out to determine whether proteins involved in zinc homeostasis could alter the labile Zn^{2+} pool and Zn^{2+} dynamics. We speculated that the metal regulatory transcription factor, MTF-1, could play an active role in changing Zn^{2+} dynamics over the course of the cell cycle. MTF-1 is a Zn^{2+} binding transcription factor that binds to metal-responsive elements in the genome to promote transcription of target genes such as metallothioneins (MTs) and ZnT1 that are responsible for sequestering and exporting excess Zn^{2+} to maintain zinc homeostasis, respectively (18, 206). Knockdown of MTF-1 would be expected to alter the buffering capacity of cells in elevated Zn^{2+} by interfering with the induction of MT expression (206).

To determine how knockdown of MTF-1 affected cell proliferation and the labile Zn^{2+} pool, we developed stable cell lines using two lentiviral constructs encoding shRNAs, one against *mtf1* to knock down the endogenous protein (MTF-1 KD) and another with non-specific scrambled shRNA as control (Scr Ctrl). Western blot analysis of MTF-1 expression in these cell lines showed a significant decrease in MTF-1 in KD cells compared to Scr Ctrl and WT cells (Figure 2.6A; MTF-1/α-Tubulin protein level: 1 (WT), 0.96 (Scr Ctrl) and 0.55 (MTF-1 KD); $^*p < 0.05$ for Scr Ctrl vs. KD). As expected, downstream expression of MTs is not induced in KD cells upon treatment with 40 µM $ZnCl_2$ for 48 h, whereas Scr Ctrl cells successfully induce MTs in high Zn^{2+} (Figure 2.6A). We also noticed that MTF-1 KD decreased basal levels of MT, even in the absence of excess Zn^{2+}, as has been previously reported (206). Next, we performed a cell proliferation assay on KD and Scr Ctrl cells with zinc deficient (ZD) and zinc enriched (ZR) media for 48h. The same number of cells were plated on day 0, and the number of viable cells was determined after 48 hours with CellTiter-Glo. This assay revealed that the number of viable cells in both cell lines was less in ZD media compared to MM media, consistent with previous work; however, there was no difference between the two cell lines. On the other hand, there were significantly less MTF-1 KD cells compared to Scr Ctrl in elevated Zn^{2+} (ZR30, $^*p = 0.011$; ZR50 $^{****}p<0.0001$, Figure 2.6B). This result was confirmed by fluorescence image analysis from long term time-lapse images of cells grown for 24h vs. 48h in differential zinc media (Figure 2.6C). Taken together, these results demonstrate that knockdown of MTF-1 lowers basal levels of MT and renders cells unable to induce metallothionein expression in elevated zinc. Further, MTF-1 KD compromises cellular proliferation in high Zn^{2+}.

To determine whether knockdown of MTF-1 alters the intracellular cytosolic labile Zn^{2+} pool, we used the NES-ZapCV2 sensor and *in situ* calibrations to quantify the concentration of labile Zn^{2+} in the cytosol. Briefly, Scr Ctrl and MTF-1 KD cells were grown in MM and ZR50 media for 24h, followed by an *in situ* calibration and conversion of FRET ratios to Zn^{2+} concentrations, as described in Methods. MTF-1 knockdown significantly increases the labile Zn^{2+} pool (Figure 2.7). For Scr Ctrl cells grown in MM, the median cytosolic $[Zn_{rest}]$ was 0.29 nM and 50% of the

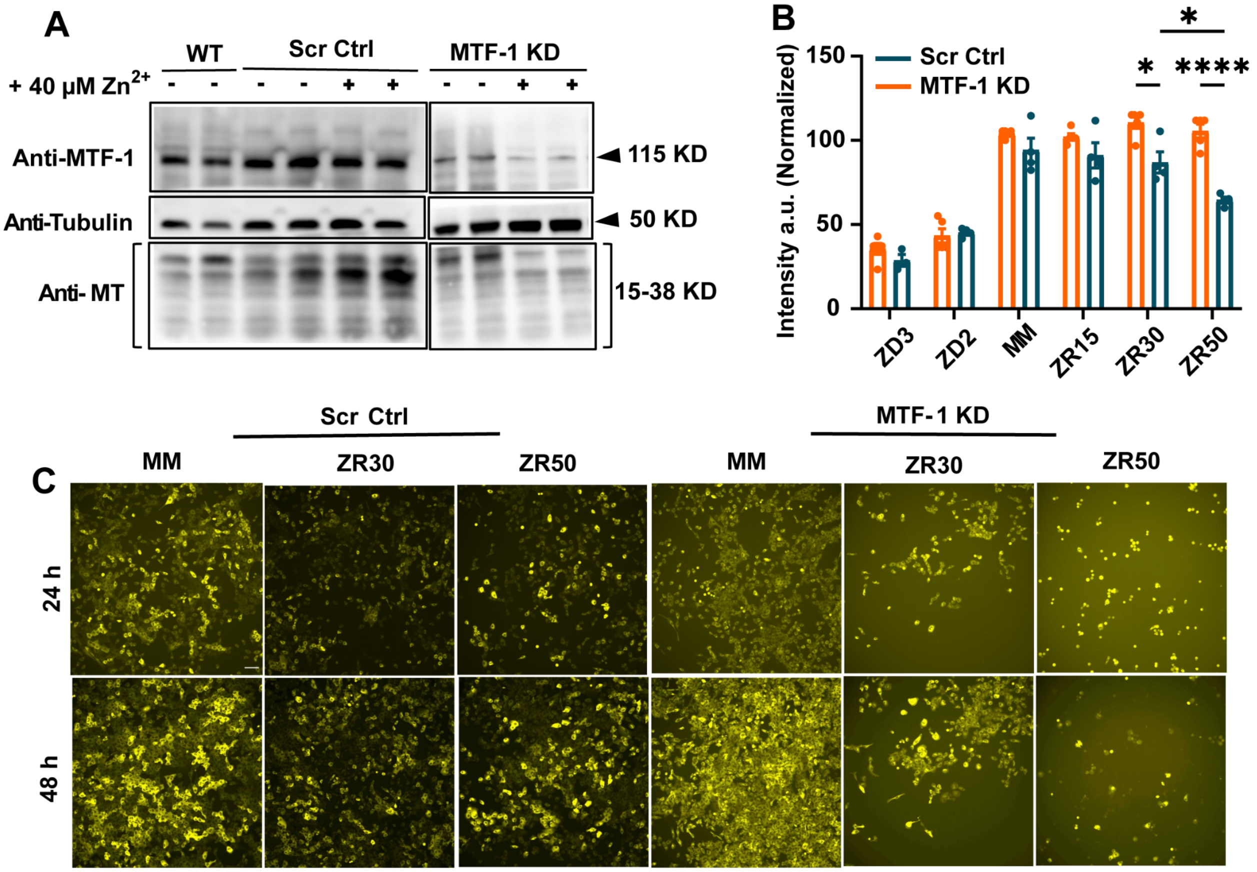

Figure 2.6: MTF-1 knockdown results in less cell proliferation under high nutritional Zn^{2+} condition. (A) Western blots for MTF-1 and MT in MCF10a wild-type (WT), scrambled control (Scr Ctrl), and MTF-1 knockdown (KD) cells show lower MTF-1 expression in KD cells compared with WT and Scr Ctrl cells. MT levels are higher in Scr Ctrl cells than MTF-1 KD cells upon treatment with 40 μM Zn2+ for 48 h compared with the no zinc condition. Duplicates were run per condition. Blots for WT and Scr Ctrl cells were run on a single gel, whereas blot for MTF-1 KD cells was run on a separate gel. (B) CellTiter-Glo proliferation assay was performed on Scr Ctrl and MTF-1 KD cells grown for 48 h in different medium conditions. Cells were plated at a similar density in four biological replicates (n = 4) and technical triplicate. Intensity data were normalized to intensity of Scr Ctrl cells in MM condition. Each dot represents the mean of four technical replicates, and the plot shows the mean ± SEM of all biological replicates. Statistical analyses was performed using two-way ANOVA with Tukey-Kramer test ($*p < 0.05$, $****p < 0.0001$). (C) Fluorescence images of Scr Ctrl and MTF-1 KD cells grown in MM, ZR30, and ZR50 media for 24 and 48 h shows lower proliferation in KD cells with ZR30 and ZR50 compared with Scr Ctrl cells. Scale bar: 100 μm.

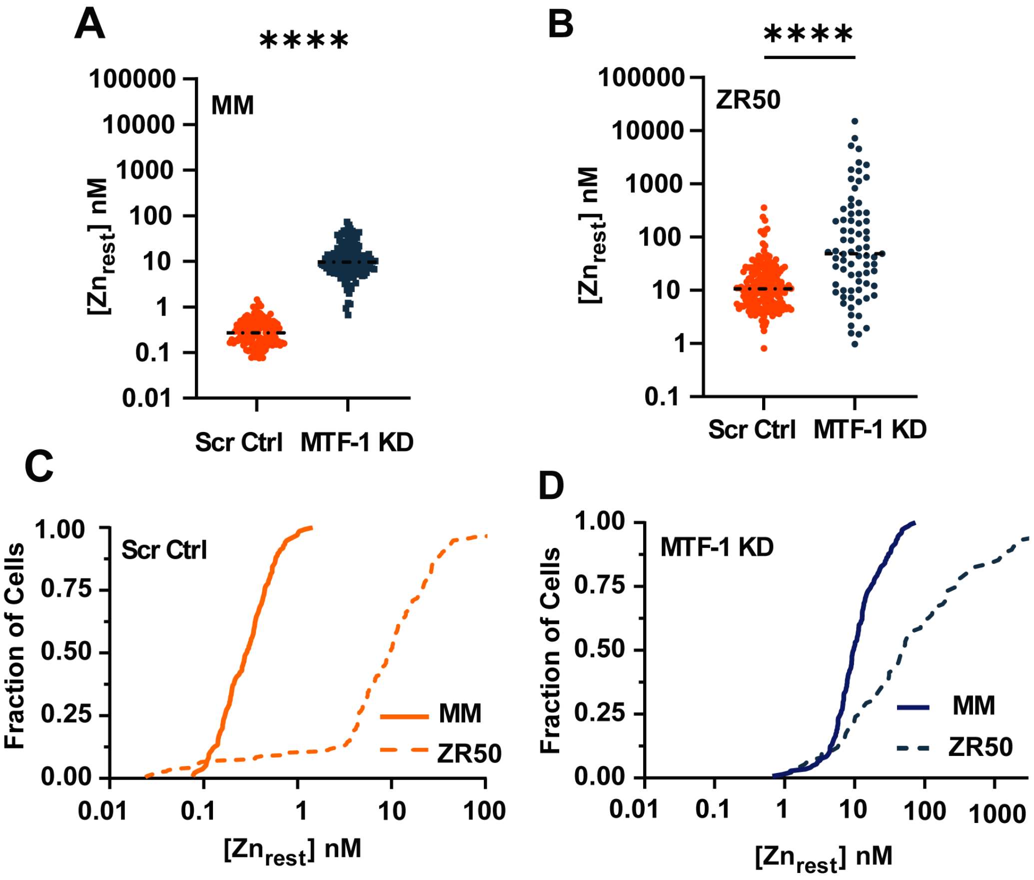

Figure 2.7: MTF-1 KD cells have higher resting zinc than Scr Ctrl cells. FRET calibration experiments on MCF10a Scr Ctrl and MTF-1 KD cells stably expressing H2B-HaloTag and NES-ZapCV2 FRET sensor were carried out to quantify the labile zinc pool. (A and B) Scatterplots showing a direct comparison of cytosolic resting Zn^{2+} [Zn_{rest}] in Scr Ctrl and MTF-1 KD cells grown for 24 h in MM and ZR50 media, respectively. Fractional saturation (FS) and dynamic range (DR) of the sensor were calculated, and [Zn^{2+}] was quantified from each experiment as described in the Methods section (Figures 2.2 and 2.8). Each dot on the scatter plot represents [Zn_{rest}] of a single cell plotted on a log scale. Only values within FS: 0–1 and DR: 1.35–1.65 ranges were considered for calculating [Znrest]. For statistical analysis, cells were pooled from two biological replicates for Scr Ctrl cells in MM (131 cells) and ZR50 (200 cells) and for MTF-1 KD cells in MM (193 cells) and ZR50 (82 cells). Statistical analyses were performed using non-parametric unpaired two-tailed Mann Whitney test (with 99% confidence level) (n = 3 biological replicates, ****$p \leq 0.0001$). (C and D) Cumulative fractional distribution plots of cytosolic [Znrest] for Scr Ctrl cells grown in MM and ZR50 and for MTF-1 KD cells grown in MM and ZR50 conditions, respectively. Values along the x axis are truncated for better display of distribution of data points.

values were between 0.17 – 0.45 nM (quartile 1, Q1 and quartile 3, Q3, respectively; Figure 2.7A, 2.7C). We noted that there was a broad, non-normal distribution of [Zn_{rest}] values from individual cells, so we report the median, Q1-Q3 quartile range, and use a non-parametric unpaired two-tailed Mann Whitney test as a statistical test. The value of 0.29 nM agrees with prior studies of cytosolic [Zn_{rest}] in mammalian cells (13, 14, 48, 132). In comparison, MTF-1 KD cells grown in MM exhibited a significantly higher median [Zn_{rest}] of 9.67 nM and Q1-Q3 of 6.31 to 17.53 nM demonstrating that MTF-1 plays an important role in maintaining resting Zn^{2+} levels in cells.

When cells were grown in elevated Zn^{2+} (ZR50), labile Zn^{2+} increased. As shown in Figure 2.7B and 2.7C, MTF-1 KD cells had significantly higher [Zn_{rest}] compared to Scr Ctrl cells. The corresponding median cytosolic Zn^{2+} in Scr Ctrl was 9.62 nM compared to 48.5 nM for MTF-1 KD. The Q1 to Q3 ranges were 4.50-21.13 nM and 12.09-284.96 nM, respectively for Scr Ctrl and MTF-1 KD. We note that fractional saturation values for ZapCV2 in Scr Ctrl cells increased from 0.25 ± 0.08 (in MM) to 0.70 ± 0.09 (in ZR50) as depicted in Figure 2.8. On the other hand, MTF-1 KD cells increased from 0.64 ± 0.11 in MM to 0.77 ± 0.15 in ZR50. In the ZR50 condition, the sensor is close to the saturation limit and hence labile Zn^{2+} may be underestimated. These results demonstrate that MTF-1 is critical for allowing cells to regulate cytosolic Zn^{2+} levels in response to increasing Zn^{2+} in the media.

2.4.4 Depletion of MTF-1 changes how cells respond to Zn^{2+} perturbation

Given that MTF-1 knockdown elevated cytosolic Zn^{2+}, we wanted to define how MTF-1 knockdown affected the ability of cells to respond to Zn^{2+} perturbation. Cells were grown in MM for 24h, followed by addition of $ZnCl_2$ or TPA. Addition of 2 or 3μM TPA (ZD2 and ZD3, respectively) led to a rapid decrease in the FRET ratio of NES-ZapCV2, indicating a decrease in labile Zn^{2+}. There were no significant differences between the MTF-1 KD cells or the Scr control in the ZD conditions. This result was expected, since MTF-1 generally regulates the cellular

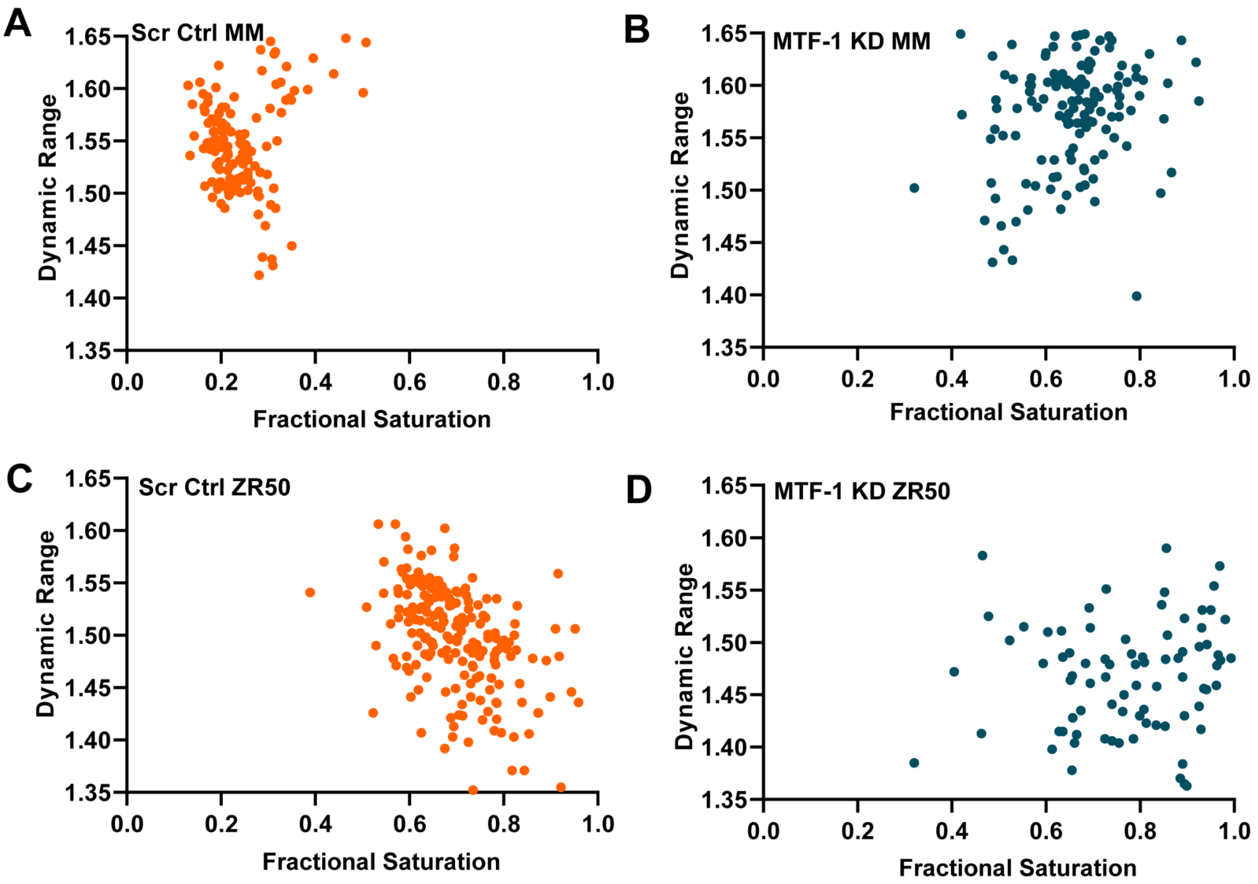

Figure 2.8: Plots of dynamic range (DR) versus fractional saturation (FS) from intracellular FRET calibration experiments. Each dot represents data from a single cell. Panel (A) and (B) depict data from Scr-Ctrl and MTF-1 KD cells grown in MM for 24h; where n = 131, and 193 cells pooled from 3 biological replicates, respectively. Panel (C) and (D) shows plots for Scr-Ctrl and MTF-1 KD cells grown in ZR50 for 24h; where n = 200, and 82 cells pooled from 3 biological replicates, respectively. Only values within the FS: 0-1 and DR: 1.35-1.65 range were considered for calculating [Zn_{rest}]. Dynamic range: R_{max}/R_{min}; Fractional saturation: $(R-R_{min}) / (R_{max}-R_{min})$ where R, R_{min} and R_{max} represent the average resting, minimum and maximum FRET ratio.

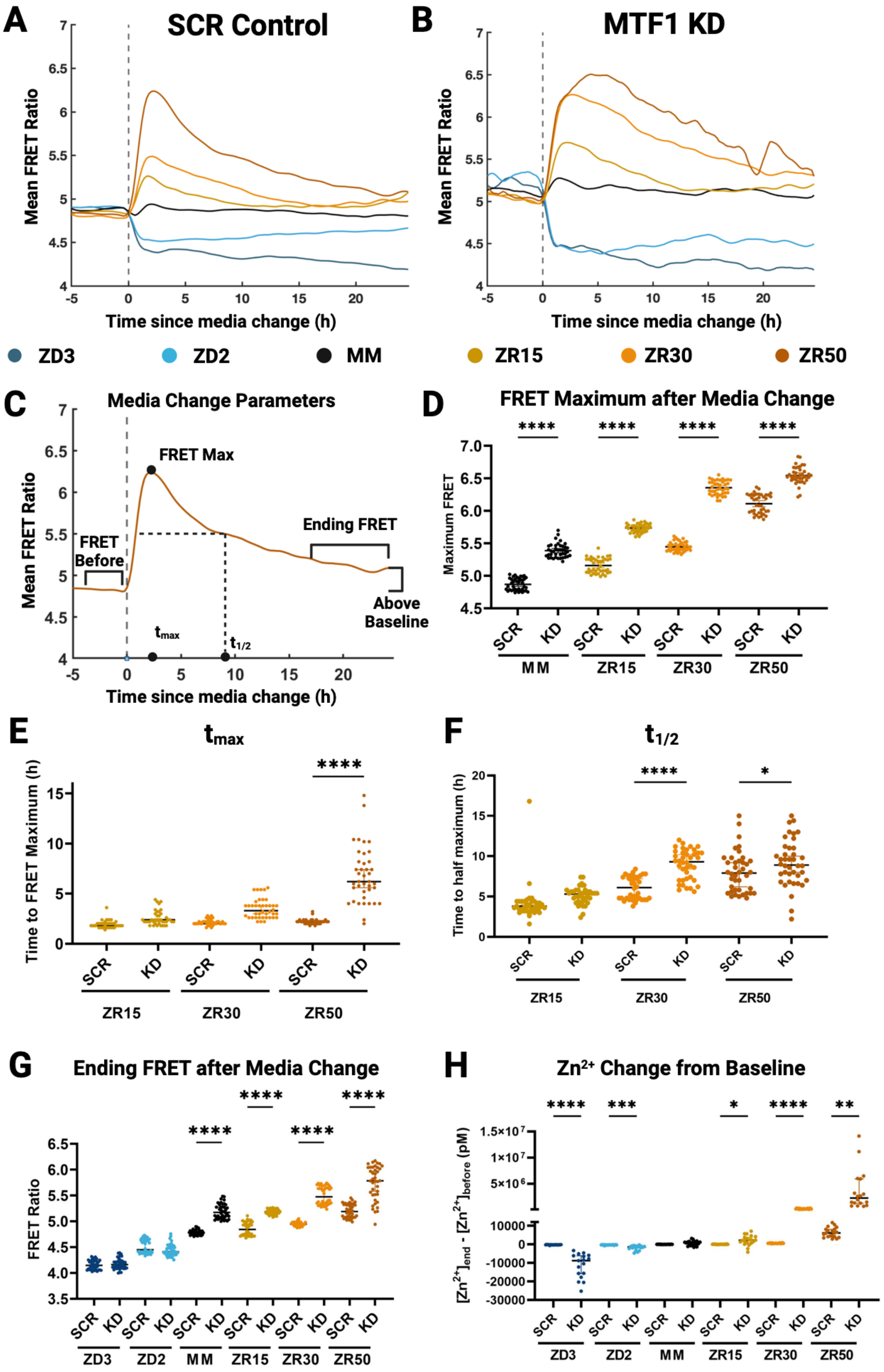
A
SCR Control
Mean FRET Ratio
Time since media change (h)
B
MTF1 KD
Mean FRET Ratio
Time since media change (h)
ZD3
ZD2
MM
ZR15
ZR30
ZR50
C
Media Change Parameters
FRET Max
FRET Before
Ending FRET
Above Baseline
t_{max}
$t_{1/2}$
Mean FRET Ratio
Time since media change (h)
D
FRET Maximum after Media Change
Maximum FRET
****
****
****
****
SCR
KD
MM
ZR15
ZR30
ZR50
E
t_{max}
Time to FRET Maximum (h)
****
SCR
KD
ZR15
ZR30
ZR50
F
$t_{1/2}$
Time to half maximum (h)
****
*
SCR
KD
ZR15
ZR30
ZR50
G
Ending FRET after Media Change
FRET Ratio
****
****
****
****
SCR
KD
ZD3
ZD2
MM
ZR15
ZR30
ZR50
H
Zn^{2+} Change from Baseline
$[Zn^{2+}]_{end} - [Zn^{2+}]_{before}$ (pM)
****
***
*
****
**
1.5×10^7
1×10^7
5×10^6
10000
0
-10000
-20000
-30000
SCR
KD
ZD3
ZD2
MM
ZR15
ZR30
ZR50

Figure 2.9: Depletion of MTF-1 changes labile zinc dynamics after perturbation of available media zinc. (A and B) Mean traces of FRET ratio before and after zinc perturbation in MTF-1 KD or Scr Ctrl cells. Cells were grown in MM, then changed to different zinc media (indicated by vertical dotted line). One representative biological replicate is shown, and the remaining biological replicates are shown in Figure 2.10. (C) Parameters used to identify changes in free zinc dynamics after perturbation. Maximum FRET, ending FRET, and t_{max} are calculated from 20 subsampled mean FRET traces. (D) Maximum FRET after media change between different zinc levels and MTF-1 status. (E) Time to FRET maximum after media change. (F) Time for FRET ratio trace to decay to half the maximum value after media change (t1/2). (G) Ending FRET ratio after media change. Ending FRET is calculated by taking the average of the final 30 time points of the mean FRET traces. (H) Difference in cytosolic zinc at the end of timelapse. Difference calculated by subtracting the cytosolic zinc at the end of the timelapse from the cytosolic zinc level before the media change. Comparisons conducted with one-way ANOVA, with follow-up t tests, which are plotted. $*p < 0.05$, $****p < 0.0001$. NS indicates $p > 0.05$. Figure created with BioRender. Cells in this experiment were stably expressing NES-ZapCV2, H2B-HaloTag, and either a Scr shRNA or an MTF-1 KD shRNA. Cells were plated with similar density in two biological replicates (n = 2) across five wells in each replicate.

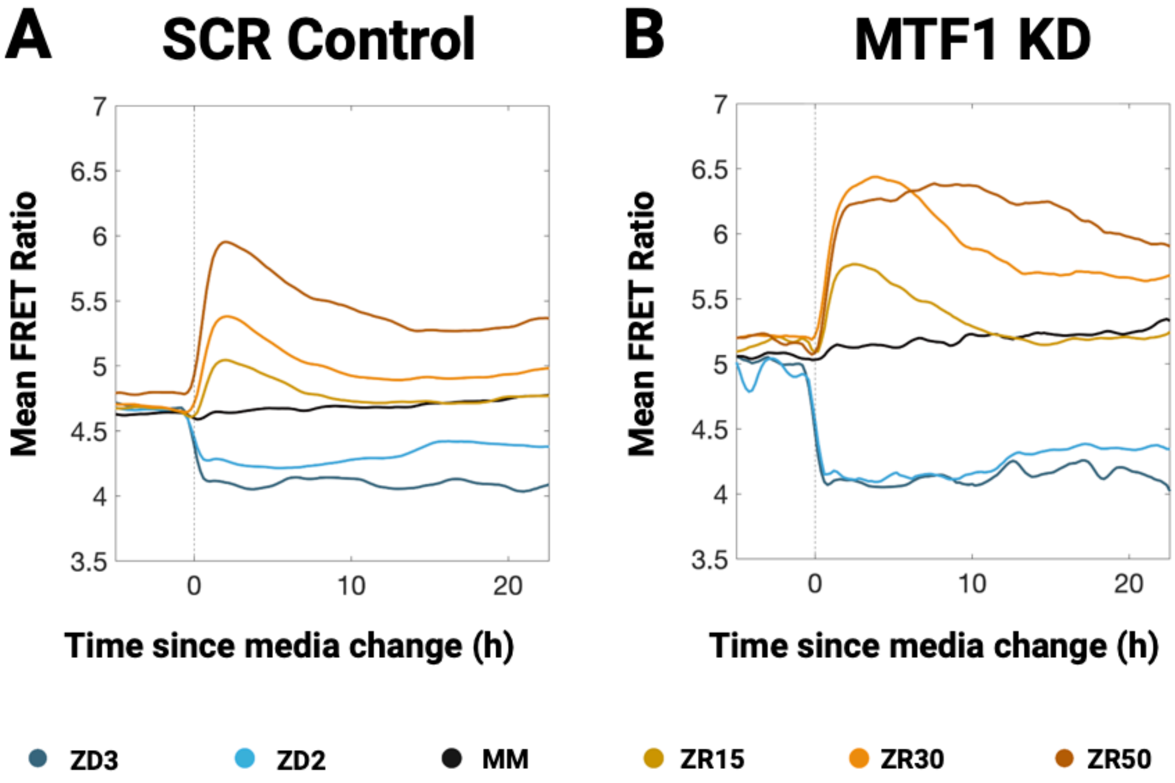

Figure 2.10: Second biological replicate of media change experiment. Mean traces of FRET ratio before and after zinc perturbation in SCR control (A) or MTF-1 knockdown cells (B). Cells were grown in MM, then changed to different zinc media. The dotted line indicates the frame at which the media was changed.

response to high Zn^{2+}. When Scr Ctrl cells were exposed to elevated Zn^{2+} (ZR15, ZR30, ZR50), there was a rise in labile Zn^{2+} lasting approximately two hours, followed by a decrease, where Zn^{2+} approaches the initial resting level before the media change (Figure 2.9A and Figure 2.10). Depletion of MTF-1 impairs the cell's ability to reestablish homeostasis after Zn^{2+} elevation (Figure 2.9B, and Figure 2.10).

To quantify aberrations in how cells handle high Zn^{2+} upon depletion of MTF-1, we took subsamples of 100-300 single-cell FRET ratio traces, and averaged these FRET ratio traces to get a subsampled mean FRET trace (Figure 2.9C). From this trace, we extracted several parameters to describe the response curves. These included the maximum FRET ratio after the media change (FRET max), time at which this maximum is reached (t_{max}), time for the FRET ratio curve to decay to half of the maximum value ($t_{1/2}$), ending FRET ratio at the end of the time-lapse, and the change in the concentration of Zn^{2+} (compared to baseline) at 24 hours. This process was repeated 20 times for different randomly subsampled mean FRET ratio traces.

We identified several interesting patterns in Zn^{2+} dynamics after Zn^{2+} perturbation. We found that cells deficient in MTF-1 reached a higher maximum FRET ratio after an increase in media Zn^{2+} (Figure 2.9D), likely due to decreased buffering capacity and decreased ability to lower cytosolic Zn^{2+} via ZnT1. Generally, the time to the FRET ratio maximum was not significantly different between MTF-1 KD and Scr Ctrl cells (Figure 2.9E), except for the ZR50 condition where it took longer to reach FRET max (6 hours vs. 2 hours). The decay of the FRET signal after media change took significantly longer in MTF-1 KD cells in high Zn^{2+} conditions (Figure 2.9F). As a consequence, 24 hours after media change, the MTF-1 KD cells displayed a higher FRET ratio, and hence a higher Zn^{2+} concentration than prior to perturbation (Figure 2.9G, 2.9H). Combined, these results indicate that MTF-1 is necessary for cells to efficiently restore homeostasis after elevation of Zn^{2+}.

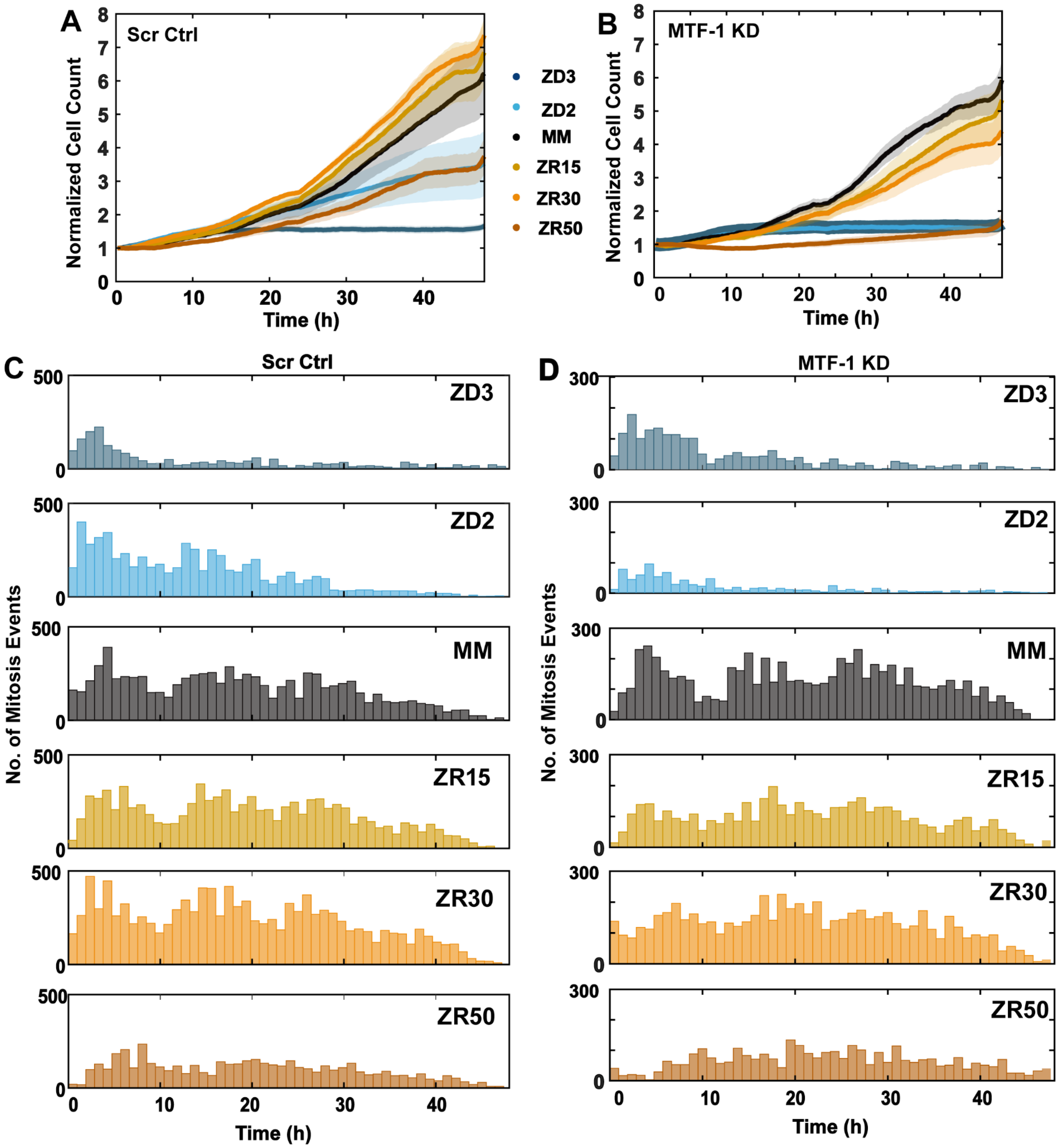

Figure 2.11: MTF-1 KD compromises cell proliferation in high Zn^{2+}. (A and B) Proliferation of MCF10a Scr Ctrl and MTF-1 KD cells expressing NES-ZapCV2 and H2B-HaloTag in different zinc conditions over 48 h. Each line represents the average of four wells normalized to initial plating density. Shaded areas represent standard deviation. (C and D) Histograms show the number of mitosis events of MCF10a Scr Ctrl and MTF-1 KD cells expressing NES-ZapCV2 over time. Scr Ctrl or MTF-1 KD cells were plated with similar cell density in two biological replicates (n = 2) across five wells in each replicate.

2.4.5 MTF-1 knockdown compromises proliferation in high Zn^{2+}

Given that MTF-1 plays an important role in regulating the cellular response to Zn^{2+} elevation, we set out to determine whether MTF-1 knockdown affected Zn^{2+} dynamics during the cell cycle. We carried out long term imaging on Scr Ctrl and MTF-1 KD cells treated with MM, low zinc and high zinc media and tracked asynchronously cycling cells for multiple days. As shown in Figure 2.11, the Scr Ctrl and MTF-1 KD cells proliferated similarly in the MM condition, similar to our bulk results in Figure 2.6B. The Scr Ctrl cells showed lower proliferation in ZD2 and ZD3 and higher proliferation in ZR15, ZR30 (Figure 2.11A, C), similar to WT MCF10a cells in Figure 2.11C and previous studies. Finally, Scr Ctrl cells showed decreased proliferation in the ZR50 condition, suggesting that if Zn^{2+} levels are too high proliferation is impaired (Figure 2.11A). MTF-1 KD cells displayed a dose dependent decrease in proliferation with increasing zinc in the media (Figure 2.11B), indicating that MTF-1 is essential for maintaining a balance of Zn^{2+} that supports proliferation. When we plotted the single cell FRET tracks as a function of time and followed mitosis events, we observed several trends. As expected, mitosis events stopped within 15h for cells grown in ZD2 and ZD3. In addition, we found that mitoses are generally distributed throughout the imaging window in both KD and Scr Ctrl cells in MM and ZR conditions (Figure 2.11C, 2.11D; Figure 2.12). The one exception is that for MTF-1 KD cells in ZR50, there are very few mitosis events within the first 10 hours of the timelapse. Overall, the number of mitosis events in MTF-1 KD cells is lower in all zinc conditions than Scr Ctrl cells, further indicating that mis-regulated Zn^{2+} homeostasis in MTF-1 knockdown cells results in perturbed cell proliferation. Finally, the number of mitosis events is decreased for Scr Ctrl ZR50 and all MTF-1KD ZR conditions, indicating that if Zn^{2+} levels get too high, cells are unable to undergo mitosis.

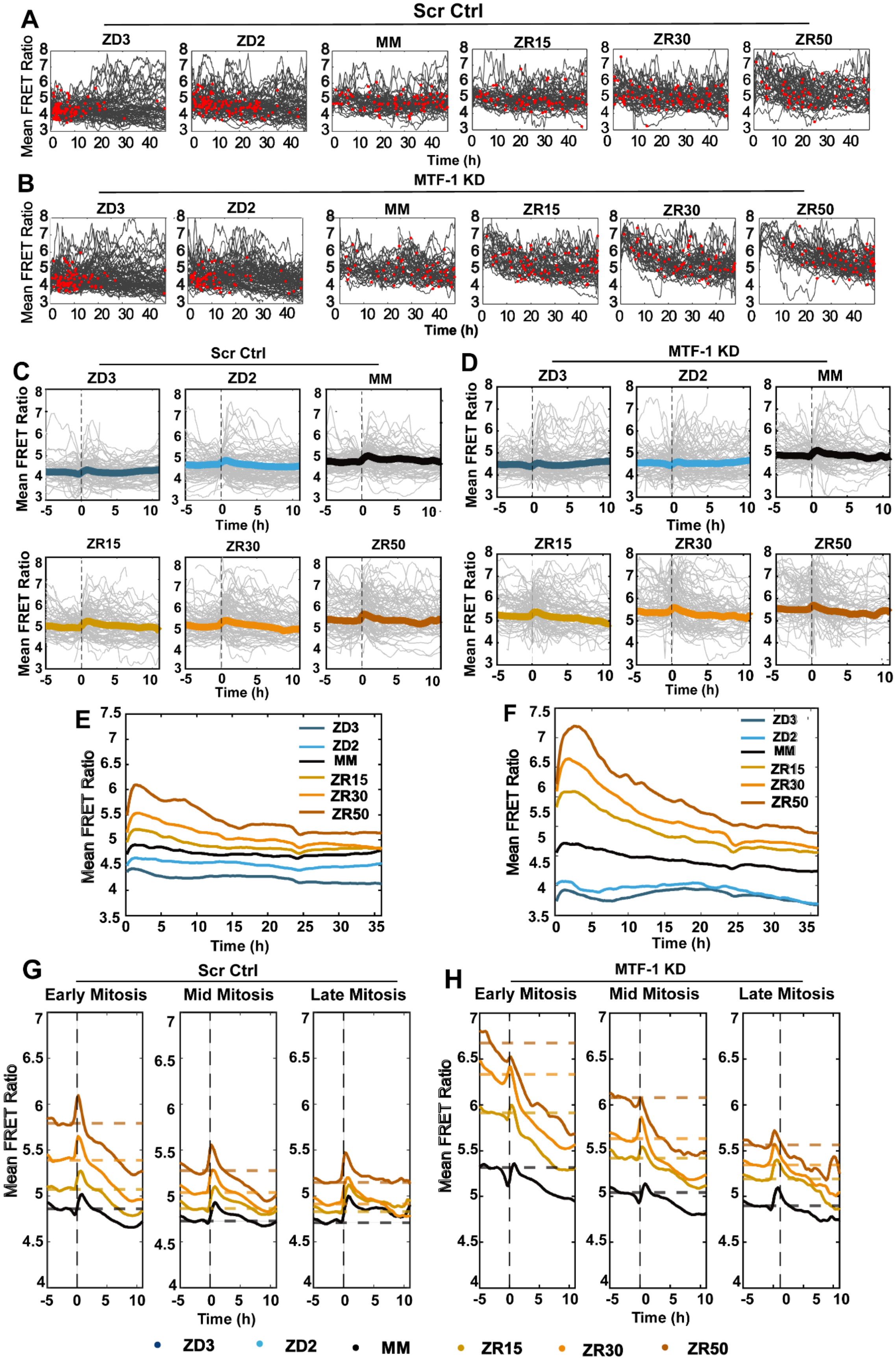
A
Scr Ctrl
ZD3
ZD2
MM
ZR15
ZR30
ZR50
Mean FRET Ratio
Time (h)
B
MTF-1 KD
ZD3
ZD2
MM
ZR15
ZR30
ZR50
Mean FRET Ratio
Time (h)
C
Scr Ctrl
ZD3
ZD2
MM
ZR15
ZR30
ZR50
Mean FRET Ratio
Time (h)
D
MTF-1 KD
ZD3
ZD2
MM
ZR15
ZR30
ZR50
Mean FRET Ratio
Time (h)
E
Mean FRET Ratio
Time (h)
ZD3
ZD2
MM
ZR15
ZR30
ZR50
F
Mean FRET Ratio
Time (h)
ZD3
ZD2
MM
ZR15
ZR30
ZR50
G
Scr Ctrl
Early Mitosis
Mid Mitosis
Late Mitosis
Mean FRET Ratio
Time (h)
H
MTF-1 KD
Early Mitosis
Mid Mitosis
Late Mitosis
Mean FRET Ratio
Time (h)
● ZD3
● ZD2
● MM
● ZR15
● ZR30
● ZR50

Figure 2.12: Zn^{2+} pulse, mitosis, and altered Zn^{2+} dynamics following mitosis in MCF10a Scr Ctrl and MTF-1 KD cells expressing NES-ZapCV2. (A, B) Single cell traces showing FRET ratios of MCF10a Scr Ctrl and MTF-1 KD cells expressing NES-ZapCV2 over time. Red dots indicate a mitosis event over time. One hundred random traces containing mitosis events across five wells are plotted in each condition. (C, D) Single-cell traces of MCF10a Scr-Ctrl and MTF-1 KD cells after alignment to mitosis are represented in gray (n=100 randomly selected cells per plot). Average FRET ratios of all traces are overlaid in color in a 15 h window around mitosis. (E, F) Mean FRET ratio of Scr-Ctrl and MTF-1 KD cells expressing NES-ZapCV2 aligned to time (at t = 0, media was changed to the respective conditions). (G,H) Mean FRET ratio aligned to mitosis (at t = 0) from all cell tracks aligned to mitosis in early (frames 1-60), mid (frames 61-119) and late (frames 120-200) stages of imaging time frame for Scr Ctrl and MTF-1 KD cells. Cells were plated with similar cell density in two biological replicates (n=2) across five wells in each replicate.

2.4.6 MTF-1 knockdown alters the Zn^{2+} pulse following mitosis

Aligning the single cell FRET tracks to mitosis permits more detailed analysis of how MTF-1 knockdown affects the Zn^{2+} pulse at mitosis (Figure 2.12). All conditions show a zinc pulse immediately following mitosis, and the magnitude of the pulse correlates with the amount of Zn^{2+} in the media and in the cytosol. We categorized the mitosis events into early, mid, and late depending on their occurrence with respect to media change (at time t = 0). Because it takes more than 20 hours for MTF-1 KD cells to establish a steady state level of Zn^{2+} after perturbation, we focused on late mitosis events to compare the Zn^{2+} pulse between Scr Ctrl and MTF-1 KD (Figure 2.12). As expected, the magnitude of the FRET ratio peak increases with increasing Zn^{2+} in the media and in the cytosol. In elevated Zn^{2+} MTF-1 KD cells reach a significantly higher FRET ratio during the Zn^{2+} pulse compared to Scr Ctrl cells (Figure 2.13A, 7B). To compare the magnitude of the Zn^{2+} pulse, we converted the FRET ratio to Zn^{2+} concentration, revealing that in MM in Scr Ctrl cells there is an 8x increase in Zn^{2+} (197 to 1628 pM), while in MM in MTF-1 KD cells there is a 3x increase in Zn^{2+} (448 to 1398 pM) (Table 1). In ZR conditions, the concentration of Zn^{2+} at the peak of the pulse reaches nM levels (39 nM for Scr Ctrl in ZR15 up to a high of 88 nM for MTF-1 KD in ZR50). Overall, MTF-1 KD cells show a higher concentration of Zn^{2+} at rest and higher concentration of Zn^{2+} at the peak of the pulse (Figure 2.13C,D; Table 1). The peak FRET after mitosis shifts earlier as Zn^{2+} increases (Figure 2.13A, B, Figure 2.5E).

2.4.7 High Zn^{2+} does not induce apoptosis

High Zn^{2+} has been shown to induce apoptosis (207), so it is possible that reduced cell numbers in high Zn^{2+} result from cell death as opposed to reduced proliferation. To evaluate this possibility, we performed an Annexin-V apoptosis assay. We observed that upon treatment with 6 μM camptothecin, a DNA damaging drug, for 12h ~50% of cells were apoptotic (combined early and late apoptosis). However, the majority of Scr Ctrl and KD cells grown in MM, ZR15, ZR30 for

Table 1: Concentration of cytosolic Zn^{2+} during Zn^{2+} pulse

Zinc Conditions	**DR**	**$[Zn^{2+}]$ pM**			
		SCR Resting	**SCR Peak**	**KD Resting**	**KD Peak**
ZD3	1.65	1	3	5	13
	1.55	**2**	**5**	**10**	**26**
	1.45	3	11	23	62
ZD2	1.65	46	235	16	21
	1.55	**96**	**544**	**32**	**42**
	1.45	247	1655	77	102
MM	1.65	91	640	196	558
	1.55	**197**	**1628**	**448**	**1398**
	1.45	535	5878	1334	4912
ZR15	1.65	241	1401	1239	3080
	1.55	**559**	**3928**	**3417**	**9807**
	1.45	1710	17210	14484	56815
ZR30	1.65	427	2293	2533	9455
	1.55	**1043**	**6932**	**7795**	**38767**
	1.45	3497	35712	41779	439906
ZR50	1.65	1703	10801	7712	17821
	1.55	**4915**	**45971**	**30011**	**88894**
	1.45	22900	586030	293011	1984589

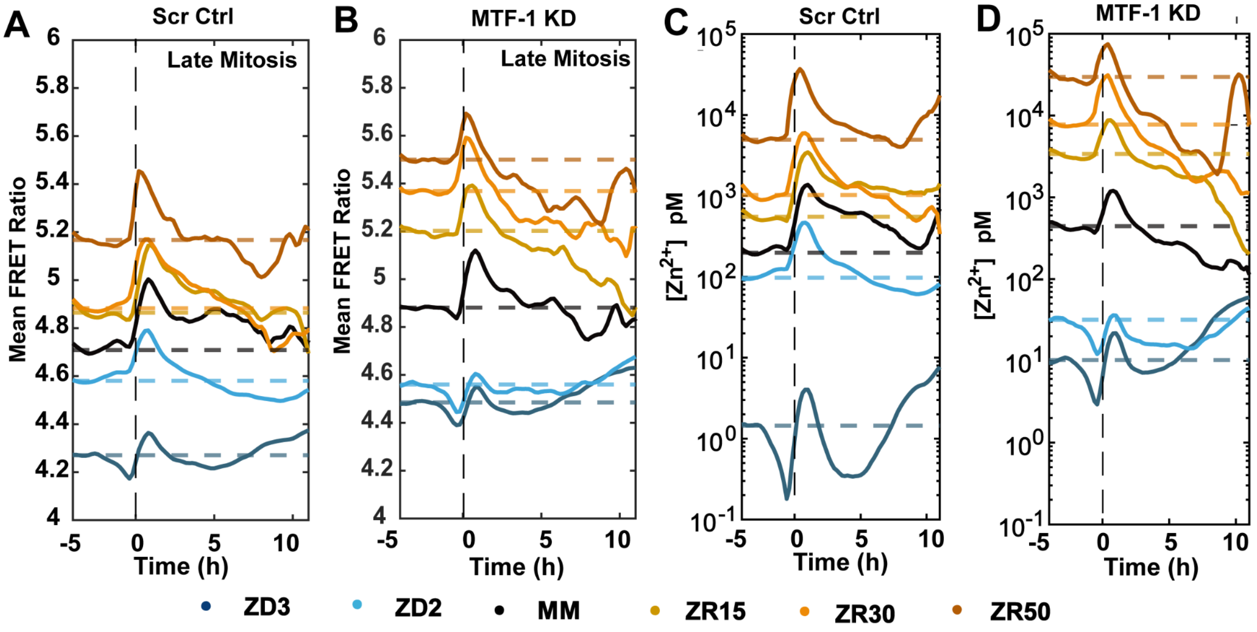

Figure 2.13: MTF-1 KD increases the magnitude of the Zn^{2+} pulse and alters Zn^{2+} dynamics following mitosis. (A and B) Average FRET ratios of all traces aligned to mitosis showing late mitosis events (from the last 120–200 frames into the time series). Horizontal dashed line refers to the resting FRET ratio before mitosis, and vertical dashed line denotes alignment to mitosis (t = 0). (C and D) Corresponding conversion of average FRET ratio to $[Zn^{2+}]$ from all the late mitosis events considering a mean DR of 1.55 for ZapCV2 sensor expressed in Scr Ctrl and MTF-1 KD cells. The dashed line denotes the resting to $[Zn^{2+}]$ level (n = 2, two biological replicates across five wells in each replicate).

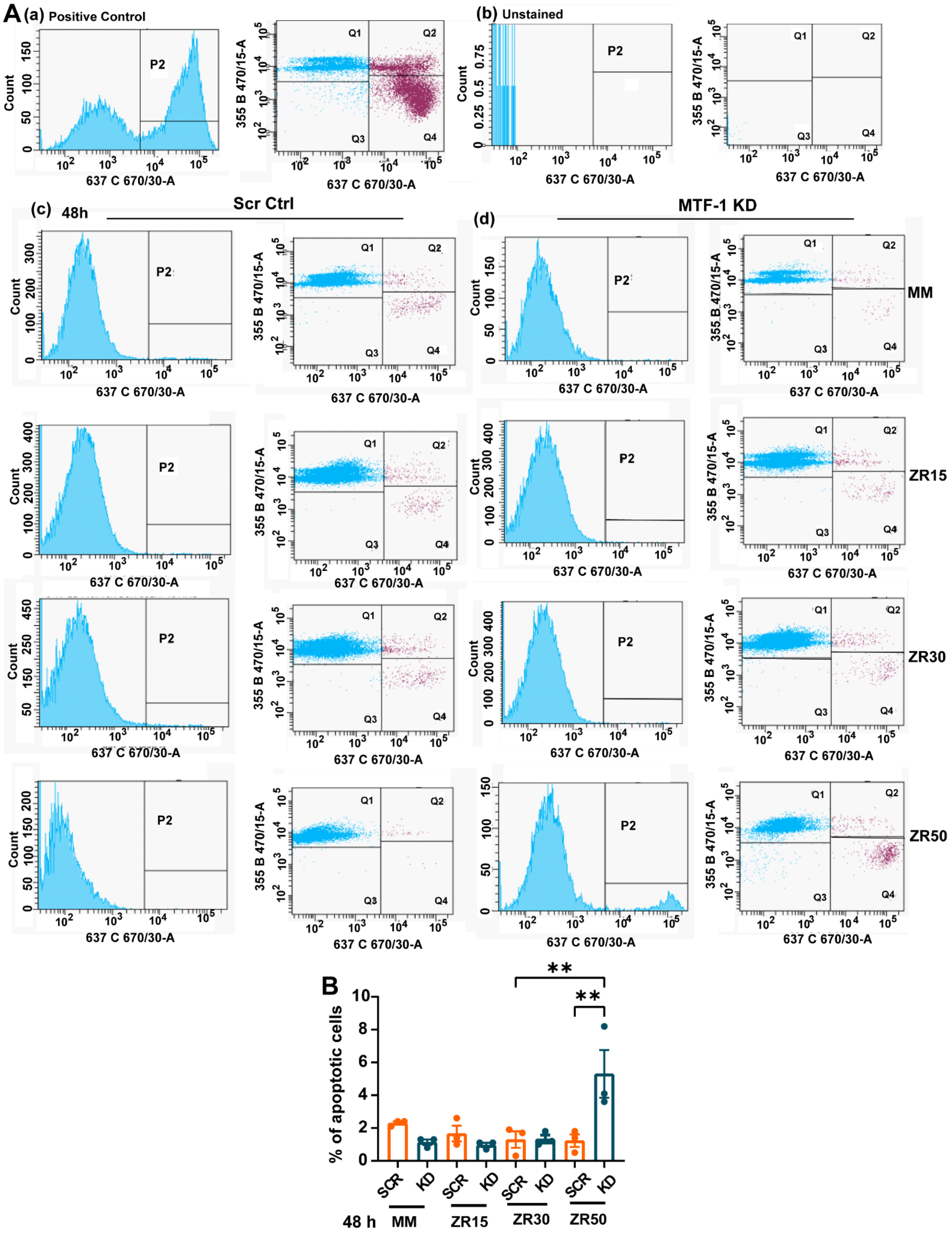
A
(a) Positive Control
(b) Unstained
(c) 48h
Scr Ctrl
(d)
MTF-1 KD
Count
P2
Q1
Q2
Q3
Q4
637 C 670/30-A
355 B 470/15-A
MM
ZR15
ZR30
ZR50
B
% of apoptotic cells
**
**
SCR
KD
48 h
MM
ZR15
ZR30
ZR50

Figure 2.14: MTF-1 KD cells undergo comparatively higher apoptosis than Scr-Ctrl cells in ZR50 condition. Apoptosis assay using flow cytometry after staining with Annexin V-Alexa 647/ Hoechst 33342. Assay was performed on MCF10a Scr Ctrl and MTF-1 KD cells grown for 48h in ZD3, ZD2, MM, ZR15, ZR30 and ZR50 media. As a positive control, MCF10a wildtype (WT) cells were treated with Camptothecin (6 µM) for 12h before the assay. Panel A (a, b, and c): (left) Representative intensity plots for Alexa 647; and (right) scatter plots of Hoechst 33342 (y-axis) verses Annexin V Alexa 647 (x-axis) for MCF10a WT stained, WT unstained, Scr Ctrl, and MTF-1 KD cells respectively. P2 population defines total apoptotic cells including early apoptotic (Q2) and late apoptotic cells (Q4). (B) Percentage of total apoptotic cells i.e. P2 population at different zinc conditions. Data are presented as mean ± SEM (n=3 biological replicate). Statistical analyses were performed with ordinary one-way ANOVA where ** indicates $p < 0.01$.

48h were non-apoptotic (Figure 2.14). Only 5.3 ± 2.5% of MTF-1 KD cells were apoptotic in ZR50 media at 48h, indicating that while apoptosis is slightly increased in ZR50 media in MTF-1 KD cells, the amount of apoptosis is not sufficient to explain the decreased proliferation of cells under this condition.

2.4.8 Cells emerging from serum starvation show different dynamics of labile Zn^{2+} compared to normally cycling cells.

There are many reports suggesting that cell synchronization techniques such as serum starvation or contact inhibition induce stress in cells, altering their ability to proliferate like asynchronously cycling cells (79, 104, 105). For example, in one study, contact inhibition and serum starvation increase replication stress (105). We subjected cells expressing H2B-HaloTag, NES-ZapCV2, and DHB-mCherry, a sensor of CDK2 activity and commonly used tool to track cell cycle progression (78), to serum starvation to test whether the dynamics of labile Zn^{2+} are the same for naturally cycling cells and cells re-entering the cell cycle following serum starvation (Figure 2.15A). After serum starvation for 48 hours, we found that cells were not synchronized in G_0, but existed in a mixed population (Figure 2.15B). To extract populations of tracks that progressed similarly over time, we clustered the populations using k-medoid clustering, with dynamic time warping as the similarity function. We identified four clusters of cell behavior after serum starvation (Figure 2.15C). Serum starvation induced quiescence, as defined by low CDK2 activity, in only 30% of cells (Figure 2.15B-C). After serum resupply, the mitosis events of this population were far less synchronized, indicating that although these cells were ostensibly paused in G_0, they did not re-enter the cell cycle synchronously. 30% of cells had persistently high CDK2 activity. This population of cells was the most synchronized and divided robustly at 10 and again at 25 hours after resupply. Using the FRET traces from this population, we detected an increase in labile Zn^{2+} following the synchronized mitosis events even though the pulse was spread due to

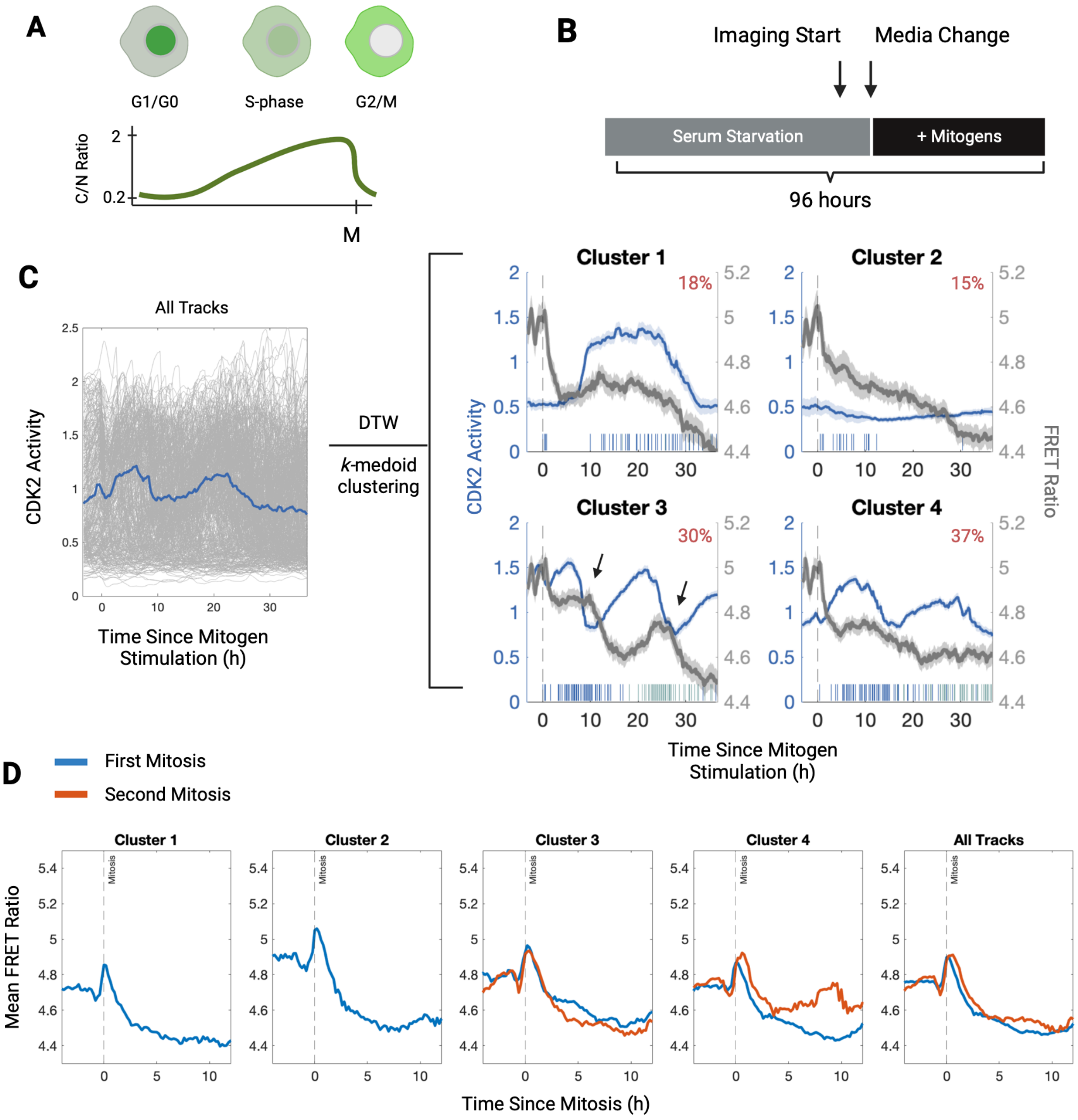
A
G1/G0
S-phase
G2/M
C/N Ratio
2
0.2
M
B
Imaging Start
Media Change
Serum Starvation
+ Mitogens
96 hours
C
All Tracks
CDK2 Activity
Time Since Mitogen Stimulation (h)
DTW
k-medoid clustering
Cluster 1
18%
Cluster 2
15%
Cluster 3
30%
Cluster 4
37%
FRET Ratio
Time Since Mitogen Stimulation (h)
D
First Mitosis
Second Mitosis
Cluster 1
Cluster 2
Cluster 3
Cluster 4
All Tracks
Mitosis
Mean FRET Ratio
Time Since Mitosis (h)

Figure 2.15: Serum starvation leads to 4 major populations of cells at different stages of the cell cycle, and each shows a similar Zn^{2+} pulse when aligned to mitosis. (A) A cartoon of the DHB-based CDK2 reporter. The cytoplasmic to nuclear ratio (C/N) measures CDK2 activity at that time point. As the cell progresses through the cell cycle, the DHB-mCherry reporter is phosphorylated by CDK2 and translocates to the cytosol. During mitosis, DHB-mCherry returns to the nucleus and C/N decreases to its lowest point in G1 or G0. (B) Schematic of the imaging experiment. Cells were serum starved for 48 hours, then imaged for 4 hours before resupplying serum for an additional 44 hours. (C, left) CDK2 traces of all tracks after 48 hours of serum starvation; note the heterogeneity of the population. Blue line indicates median CDK2 activity of all synchronized tracks. (C, right) After clustering using k-medoids clustering and Dynamic Time Warping for similarity, four clusters emerged. The blue line indicates median CDK2 activity of all traces in that cluster. The left axes are the median CDK2 activities and the shaded regions are the 95% confidence intervals. The right axes are the mean FRET ratios and the shaded regions are the 95% confidence intervals. Mitosis events are marked as dashes on the horizontal axis (dark blue is first mitosis, light blue is second mitosis). The population percentage of that cluster is in the upper right hand corner of each graph in red. Arrows in Cluster 3 indicate broad Zn^{2+} peaks. (D) Mean FRET traces aligned to mitosis for each cluster. First mitoses are marked in blue, second mitoses are marked in orange. The vertical dashed line indicates the mitosis frame.

temporal noise in the mitoses. After aligning FRET traces to the first and second waves of mitoses, we were able to resolve the Zn^{2+} pulse in early G1 (Figure 2.15D). Labile Zn^{2+} elevation was difficult to discern in all other clusters of cells, but the pulse was visible when the mitosis events were aligned (Figure 2.15E). Together, these data demonstrate that it is difficult to resolve Zn^{2+} dynamics in cells emerging from serum starvation due to the lack of synchronized re-entry into the cell cycle. Therefore, live-cell imaging is preferable to synchronization when studying cell cycle dynamics, and orthogonal confirmation of cell cycle status is imperative to define cell cycle state.

2.5 Discussion

Successful completion of the eukaryotic cell cycle involves carefully coordinated temporal changes in major signaling modulators such as proteins, transcription factors, and even labile metal ions (82, 84, 208, 209). Based on our studies of Zn^{2+} and cell proliferation (13), we have demonstrated that Zn^{2+} is one of the many key players necessary for successful completion of cell division. In mammalian cells, cytosolic labile Zn^{2+} is in the picomolar range (122, 132, 136) while human serum contains 12–15 μM Zn^{2+} (3). However, the cytosolic Zn^{2+} pool is not static but can change in response to different stimuli (e.g. activation of mast cells by IgG stimulation(210)), signaling events (e.g. Ca^{2+} dynamics (11, 50, 56, 136)), and environmental perturbations (e.g. changes in the Zn^{2+} concentration in extracellular media (14)). In this paper we set out to determine whether labile Zn^{2+} changes over the course of the cell cycle. Using fluorescent reporters and long-term live cell imaging, coupled with quantitative computational analysis, we measured both cytosolic and nuclear Zn^{2+} in a heterogeneous asynchronously cycling population for the first time. We report a Zn^{2+} pulse immediately following mitosis that lasts for 2 hours into early G1 phase; cytosolic Zn^{2+} rises from 197 pM to 1628 pM at the zinc peak in minimal media. The magnitude of the Zn^{2+} pulse is correlated with the amount of labile Zn^{2+}, which in turn correlates with the total amount of Zn^{2+} in media. In moderate Zn^{2+} deficient conditions, Zn^{2+} rises from 1 pM to 3 pM, and proliferation is compromised.

There are two previous studies that specifically measured Zn^{2+} during the cell cycle. The first was an XFRM study on fixed cells that revealed total zinc increases 3-fold in mitotic cells (205). The second was a direct measurement of labile Zn^{2+} using the FluoZin-3 AM fluorescent probe, that showed broad increases in Zn^{2+} in a bulk population of cells at 3 and 12 hours after release from serum starvation (48). These time frames were inferred to correlate with early G1 and the G1/S transition. To compare our results to this previous work, we examined Zn^{2+} dynamics when serum was resupplied to cells that had been starved of serum for 48 hours. Using a CDK2 cell cycle reporter (78) our results reveal serum starvation does not lead to synchronization of the population in G_0, an observation that has been seen previously for PC12 cells (211). When the dynamics of individual cell tracks as a function of time were clustered, we observed four populations. The two most prevalent populations of cells (accounting for 67% of the population) show broad peaks in zinc dynamics, similar to what was observed in the study by Li and Maret. However, these broad peaks can't be correlated to cell cycle phases based on time since serum resupply, the approach used by Li and Maret. Our results reveal the necessity of single cell measurements for identifying how labile Zn^{2+} changes in different phases of the cell cycle.

We also showed that the zinc-regulatory protein MTF-1 affects the magnitude of this Zn^{2+} pulse. Notably, cells with too low or too high a Zn^{2+} pulse show compromised proliferation, suggesting that maintaining Zn^{2+} levels and dynamics are important for cell cycle regulation. We speculate that cells need to meet or exceed the Zn^{2+} pulse requirement during mitosis to fulfill daughter cell Zn^{2+} requirements in early G1 and that cells possess a mechanism of remodeling of labile Zn^{2+} in daughter cells. In support of this idea, MT and ZnT1 have been previously shown to be necessary in proliferating cells (26, 59, 202–204). Further, MT has been shown to translocate to the nucleus as cells transition from quiescence to G_1 transition and again early in S phase of the cell cycle, and MT concentration increases in late G1 phase and at the G_1/S transition (26). However, as discussed below, the Zn^{2+} pulse still exists when MTF-1 is knocked down, and MT levels are dramatically decreased, so there are likely to be additional Zn^{2+} regulatory proteins necessary for remodeling Zn^{2+} during the cell cycle.

MTF-1 is the Zn^{2+} regulatory transcription factor that mediates the high Zn^{2+} response by tuning expression of ZnT1 and MT. Knockdown of MTF-1 decreased resting levels of MT, prevented the induction of MT in elevated Zn^{2+}, and significantly increased resting cytosolic labile Zn^{2+}. Our results are consistent with previous studies and also add new details related to the role of MTF-1 in Zn^{2+} homeostasis. Previous work has shown that homozygous MTF-$1^{-/-}$ knockout embryos show a 4-6-fold reduction of ZnT1 mRNA and undetectable MT mRNA (206). Additionally, steady state levels of ZnT1 and MT-I mRNAs were significantly reduced in MTF-1 knockout mouse embryonic fibroblasts (MEFs) compared with wild-type MEFs and 100 μM Zn^{2+} did not increase the level of ZnT1 or MT (206). Thus, it is clear that MTF-1 plays an important role not just in modulating MT and ZnT1 expression in response to high Zn^{2+}, but also regulating basal levels of these proteins. Our work shows that MTF-1 also regulates basal levels of Zn^{2+}. The 33-fold increase in labile Zn^{2+} in minimal media conditions could result from decreased buffering capacity due to decreased MT levels, decreased export due to decreased ZnT1 levels, or both. As expected, knockdown of MTF-1 compromised cells' ability to respond to elevated Zn^{2+}, indicating that both MT buffering and ZnT1 export are important for allowing cells to restore homeostasis after Zn^{2+} elevation. It is important to note that our shRNA did not completely knock down MTF-1 and so residual MTF-1 could contribute to zinc regulation. However, other factors, such as zinc transporters may become increasingly important when the cellular buffering capacity decreases.

Given the role of MTF-1 in helping cells maintain Zn^{2+} homeostasis, we examined how MTF-1 knockdown affected Zn^{2+} dynamics during the cell cycle. Cells with decreased MTF-1 levels, and hence decreased MT expression, still experienced a Zn^{2+} pulse after mitosis. The main consequence of MTF-1 knockdown is increased concentration of Zn^{2+} at the pulse peak for cells in elevated Zn^{2+}. In minimal media, Zn^{2+} increases to just over 1 nM in both Scr Ctrl and MTF-1 KD cells. But in zinc rich conditions, Zn^{2+} peaks at 3.9 nM for Scr Ctrl and 9.8 nM for MTF-1 KD (ZR15) and increases up to 46 nM for Scr Ctrl and 89 nM for MTF-1 KD in ZR50. While we don't know the source of Zn^{2+} that comprises the pulse, we speculate that it is likely being imported from external media, given that the magnitude of the pulse tracks with Zn^{2+} in the media and that Zn^{2+} can't be released from a cellular buffer in MTF-1 KD cells given that the buffering capacity is greatly diminished. Our defined media and MTF-1 knockdown experiments suggest that cells require a minimum Zn^{2+} pulse to proliferate, but also that if Zn^{2+} levels are too high, cells can't undergo mitosis. MTF-1 KD cells grown in ZR50 fail to proliferate in the early stages of the time-lapse until free zinc drops below a FRET ratio of 6.4, or approximately 4 μM free Zn^{2+} (Figure 2.11B, 6D, Figure 2.12D). In addition, proliferation is compromised for MTF-1 KD in ZR30 as there are fewer mitosis events in this condition (Figure 2.11B). Scr Ctrl cells in ZR50 have a Zn^{2+} pulse of 46 nM and show reduced proliferation (Figure 2.11). The elevated levels of Zn^{2+} used in this study don't induce cell death but perhaps induce cells to enter a reversible quiescent state until cells can restore an appropriate labile level. This could explain the lag in mitosis events observed in MTF-1 KD grown in high zinc conditions.

Using long-term live-cell imaging, fluorescent sensors, and computational tools, we identified a transient increase in Zn^{2+} in early G1 which we have dubbed the "Zn^{2+} pulse." This pulse scales with the concentration of zinc in the media. Further, we characterized the effects of MTF-1 knockdown on resting labile Zn^{2+} and the Zn^{2+} pulse. Knockdown of this key zinc regulatory transcription factor increases both the resting labile Zn^{2+} and the magnitude of the Zn^{2+} pulse. Cells deficient in MTF-1 respond to high media Zn^{2+} by pausing cellular proliferation until labile

Zn^{2+} decreases below 4 mM and proliferation can restart. These observations lay the groundwork for further study of zinc's role in regulating cellular proliferation.

2.6 Materials and Methods

RESOURCE AVAILABILITY

Lead contact

Further information and requests for resources and reagents should be directed to and will be fulfilled by the lead contact, Amy Palmer (amy.palmer@colorado.edu).

Materials availability

Plasmids generated in this study have been deposited to Addgene. Reagents used in this study are mentioned in the Key resource table.

Table 2: Key resource table

REAGENT or RESOURCE	SOURCE	IDENTIFIER
Antibodies		
Anti-MTF1 (H-300) rabbit polyclonal primary	Santa Cruz Biotechnology	Sc-48775
Anti-MT rabbit (FL-61) polyclonal IgG primary	Santa Cruz Biotechnology	Sc-11377
Anti-α-Tubulin mouse monoclonal primary	Santa Cruz Biotechnology	Sc-5266
Goat anti-mouse (H + L) IgG secondary	Novus Biotechnology	NB7539
Goat anti-Rabbit (H + L) IgG secondary	Novus Biotechnology	NB7160
Chemicals, peptides, and recombinant proteins		
Tris(2-pyridylmethyl) amine 98% (TPA)	Sigma-Aldrich	723134
Zinc chloride, anhydrous, 99.95% (metals basis)	Alfa Aesar	87900
Zinc chloride, 0.1 M solution	Sigma-Aldrich	39059
Chelex-100, sodium form	Sigma-Aldrich	C7901

Nonidet P-40	Sigma-Aldrich	74385
Sodium deoxycholate	Sigma-Aldrich	D6750
Protease and Phosphatase Inhibitor Cocktail (PPi)	Thermo Scientific	78441
(S)-(+)-Camptothecin, ≥90% (HPLC), powder	Sigma-Aldrch	C9911
Janelia Fluor 669 Halo-Tag dye (JF669)	Laboratory of Luke Lavis, Janelia Research Campus	N/A
DMEM/F12, HEPES	Thermo Fisher Scientific	11330057
Horse Serum, New Zealand origin	Thermo Scientific	16050122
Hydrocortisone	Sigma-Aldrich	H4001
FluoroBrite DMEM	Fisher	A18967-01
Gibco EGF Recombinant Human Protein	Thermo Fisher Scientific	PHG0313
Ham’s F12 phenol red	Sigma Aldrich	N6658
Cholera Toxin	Sigma-Aldrich	C8052
Pen/Strep	Gibco	15140-122

0.05% Trypsin-EDTA(1X)	Gibco	25300-120
Hoechst 33258	Sigma-Aldrich	861405
Critical commercial assays		
Annexin V Conjugates for apoptosis detection	ThermoFisher	A23204
CellTiter-Glo 2.0 Cell Viability Assay	Promega	G9241
Amersham ECL Prime Western Blotting Detection Reagent	GE Healthcare	RPN2232
Pierce™ BCA Protein Assay Kit	Thermo	S-11791
Deposited data		
Image analysis code	This work	https://github.com/samholtzen/live-cell-zinc-sensor.git
Experimental models: Cell lines		
Human: MCF10a	ATCC	
Human: MCF10a + PB-NES ZapCV2 and PB-H2B- mCherry (stable)	Lo., et.al. PMID: 32014109	CRL-10317; RRID:CVCL_0598
Human: MCF10a + PB-NLS ZapCV2 and PB-H2B- mCherry (stable)	This work	N/A

Human: MCF10a + PB-NES ZapCV2 and PB-H2B-HaloTag + Scrambled *mtf1*- mCherry (stable)	This work	N/A
Human: MCF10a + PB-NLS Zinc-dead and PB-H2B- mCherry (stable)	This work	N/A
Human: MCF10a + PB-NES Zinc-dead and PB-H2B- mCherry (stable)	This work	N/A
Human: MCF10a + PB-NES ZapCV2 and PB-H2B-HaloTag + shRNA *mtf1* knockdown-mCherry (stable)	This work	N/A
Human: MCF10a + PB-NES ZapCV2 and PB-H2B-HaloTag + CSII-EF-DHB-mCherry	This work	N/A
Recombinant DNA		
Plasmid: PB-H2B-HaloTag (used for stable cell line generation)	Grimm, BJ., et. al.; PMID: 28869757	N/A
Plasmid: PB-H2B-mCherry (used for stable cell line generation)	Published in previous Palmer lab paper; PMID: 32014109	N/A

Plasmid: PB-NES-ZapCV2 (used for stable cell line generation)	Published in previous Palmer lab paper; PMID: 27959493	N/A
Plasmid: PB-NLS-ZapCV2 (used for stable cell line generation)	This work	Nuclear FRET sensor in Piggybac vector; NES sequence was replaced by NLS sequence; Submitted to Addgene
Plasmid: PB-NES-Zinc-dead (used for stable cell line generation)	This work	Nuclear Zinc dead sensor in Piggybac vector; Zinc binding sequence is replaced by non-binding domain; Submitted to Addgene
Plasmid: PB-NLS-Zinc-dead (used for stable cell line generation)	This work	Nuclear Zinc dead sensor in Piggybac vector; Zinc binding sequence is replaced by non-binding domain

Plasmid: MTF1.34 human shRNA (used for MTF-1 KD mCherry stable cell line generation)	This work GeneCopoeia	HSH011543-34-LVRU6MP Plasmid containing shRNA targeted to MTF-1 gene; *Target sequence:* CCAACTCTGTCCTAACTAATA; Submitted to Addgene
Plasmid: Used for MTF-1 Scrambled – mCherry stable cell line generation	This paper GeneCopoeia	CSHCTR001-LVRU6MP Plasmid containing non-specific scrambled shRNA; Target sequence: n/a
Plasmid: CSII-EF-DHB-mCherry	Laboratory of Sabrina Spencer, CU Boulder	CDK2 kinase translocation Sensor
Software and algorithms		
BD FACSDiva Version 8	BD Biosciences	N/A
Adobe Illustrator CS	Adobe	N/A
MATLAB 2017a and VR2020b	Mathworks	N/A
Prism Version 9.2.0	GraphPad	N/A
Cell segmentation and tracking pipeline	Elliptrack	PMID: 32755578

Data and code availability

The image analysis code is accessible in GitHub (https://github.com/samholtzen/live-cell-zinc-sensor.git). Time-lapse imaging data used in this current study are not publicly available but are available from the corresponding author on request. Protocols are also available upon request.

Cell culture

MCF10a cells were procured from ATCC and maintained in full growth medium (FGM) which consists of DMEM/F12 medium (FGM) supplemented with 5% horse serum, 1% penicillin/strepomycin antibiotics, 20 ng/mL EGF, 0.5 µg/mL hydrocortisone, 100 ng/mL cholera toxin, and 10 µg/mL insulin. Cells were passaged with a 0.05% trypsin-EDTA solution. To generate the defined minimal medium (MM), we removed excess Zn^{2+} from horse serum and insulin by incubating serum and insulin solutions with Chelex-100 for 12h, followed by sterile filtration to remove Chelex-100 resin. Minimal media (MM) consisted of 50:50 Ham's F12 phenol red free/FluoroBrite DMEM with 1.5% Chelex 100-treated horse serum, 10 µg/ml Chelex 100-treated insulin, 1% pen/strep antibiotics, 20 ng/mL EGF, 0.5 µg/ml hydrocortisone, and 100 ng/ml cholera toxin. We previously quantified the metal content of MM containing Chelex-100-treated serum to MM containing serum that was not treated with Chelex-100. The ICP-MS results are presented in Lo et al in Figure 1-Supplement 1 and show that Chelex-treatment leads to a reduction in zinc (from 2.18 to 1.46 µM) and nickel (from 0.178 to 0.012 µM), but no significant changes in other metals. ZD media was generated by adding 2 or 3 µM TPA for ZD2 and ZD3, respectively. ZR media was generated by supplementing MM with 15 µM $ZnCl_2$, 30 µM $ZnCl_2$, and 50 µM $ZnCl_2$ diluted from a 0.1 M $ZnCl_2$ stock solution, for ZR15, ZR30, and ZR50, respectively. Serum starvation media contains 50:50 Ham's F12 phenol red

Table 3: Plasmid Sequences

Plasmid	Sequence
PB-NLS-ZapCV2	NLS sequence: atgcctaaaaaaaaacgtaaagttgaagatgcttcggatccc
	Zinc binding Zap1 fragment: gtcggcgagctgcacgccgccgtccatgagctcgataccatgttgacaattaatatggttcactatggaacatgtatcatctccaaggaaatcacagtcctcccaattatgagctaatggttccatagggtgtttgaaatcttgagagacatgatccttcaaaagatgtctttgtaggtcaaatagtgagctacaagactcaggacattctttccatttgtgttttaagtcattgttttt
PB-NES ZapCV2 “zinc dead”	NES sequence: atgcttcaacttcctcctcttgaacgtcttactctttcggatc
	‘Zinc dead’ Zap1 fragment: aaaaacaacgacctgaaggccaagtggaaggaggcccccgagagcgccagcagcctgttcgacctgcagcgcgccctgctgaaggacgccgtgagccaggacttcaaggcccccatggagcccctggccgccaactgggaggacgccgacttcctgggcgacgacaccgccagcatcgtgaacgccatcaacgcccaggccggcatcgagctggagctc
PB-NLS ZapCV2 “zinc dead”	NLS sequence: atgcctaaaaaaaaacgtaaagttgaagatgcttcggatccc
	‘Zinc dead’ Zap1 fragment: aaaaacaacgacctgaaggccaagtggaaggaggcccccgagagcgccagcagcctgttcgacctgcagcgcgccctgctgaaggacgccgtgagccaggacttcaaggcccccatggagcccctggccgccaactgggaggacgccgacttcctgggcgacgacaccgccagcatcgtgaacgccatcaacgcccaggccggcatcgagctggagctc

free/FluoroBrite DMEM, 1% pen/strep antibiotics, 20 ng/mL EGF, 0.5 µg/ml hydrocortisone, and 100 ng/ml cholera toxin and 3% (w/v) bovine serum albumin. For imaging experiments, cells were grown and imaged in MM, ZD, or ZR media, except in the serum starvation experiment, when they were grown and imaged in serum starvation or MM. All cells were grown in a humidified incubator at 37°C and 5% CO_2. Cell lines were routinely tested and confirmed to be mycoplasma negative by PCR.

Plasmids and cell lines

We generated MCF10a cell lines expressing PB-H2B-mCherry or PB-H2B-HaloTag and one of the following zinc sensor constructs: PB-NES ZapCV2, PB-NLS ZapCV2, PB-NES ZapCV2 “zinc dead”, or PB-NLS ZapCV2 “zinc dead”. The NLS-ZapCV2 plasmid was generated by replacing NES sequence with NLS sequence (Table 3). The “zinc dead” sensors were created by replacing all cysteine and histidine residues in the zinc binding domain with alanine in (Table 3). Stable cell lines were generated using the PiggyBac transposase system. Briefly, plasmids were transfected via TransIT-LT1 (Mirus Bio), according to manufacturer’s instructions, using 0.5 µg plasmid of interest and 2 µg Super PiggyBac transposase by electroporation. Cells were selected with G418 (0.4 mg/mL for H2B plasmid). and blasticidin (0.4 mg/mL, for zinc sensor plasmid). MCF10a cells expressing NES-ZapCV2 and H2B-HaloTag were virally transfected with CSII-EF lentiviral vector cloned with plasmid containing DHB (aa994–1087) (78) fused to mCherry. MCF10a cell lines expressing MTF-1 KD shRNA or scrambled control shRNA were generated by viral transduction. Briefly, HEK293T cells were transiently transfected with plasmid containing either MTF1.34 human shRNA (5 µg) or scrambled shRNA (5 µg) and Lenti-X fourth-generation lentiviral packaging plasmids PsPAX2 (4.5µg), and PmD2.G (0.5 µg) in OptiMEM. This was followed by viral amplification in HEK293T cells for 48 h. Successful transfection was verified via mCherry fluorescence marker. Viral particles were harvested from HEK293T cells 48 hours after transfection via filtering through 0.45 µm syringe PES (polyethersulfone) filters and the virus-containing media supplemented with polybrene (8 µg/mL) was added to MCF10a cells stably expressing NES-ZapCV2 and H2B-HaloTag and incubated for 48h. Stable cell lines used for imaging were generated by antibiotic selection (puromycin: MTF-1.34 human shRNA, scrambled shRNA). Validation of MTF-1 knockdown was established by western blot. For cell cycle experiments, stable MTF-1 KD and Scr Ctrl cells were sorted on BD FACSAria Fusion with the following optics: CFP: Ex 445 nm, Em 470/15 nm; YFP: Ex 488 nm, Em 530/30 nm; and mCherry Ex 561 nm, Em 610/20 nm.

Western Blot

MTF-1 and MT expression of MCF10a WT, Scr-Ctrl and MTF1-KD cells in MM and in 40 µM $ZnCl_2$ was assessed via Western blotting. Cells were plated in 10 cm dishes in minimal media (MM) with a seeding density of 2 x 10^6. Cells were harvested at 75% confluency. For Zn^{2+} enrichment assay, media was replaced with MM containing 40 µM $ZnCl_2$ after 24h and cells were harvested after 48h of Zn^{2+} treatment. Proteins from WT, Scr-Ctrl and MTF1-KD cells in MM and ZR conditions were isolated by lysing the cells in RIPA buffer (1% Nonidet P-40, 10% Sodium deoxycholate, 1 M Tris-HCl (pH 8.0), 5M NaCl, 10% SDS) with 1X PPi and quantified with a BCA (bicinchoninic acid) assay. Protein (30 µg) was separated using 4-20% gradient pre-cast SDS polyacrylamide gel (Mini-PROTEIN TGX precast gel, BIO-RAD, catalogue no. 456-1095) in 1X Tris/Glycine Buffer (BIO-RAD, catalogue no. 1610771) and transferred to a PVDF (polyvinylidene difluoride) membrane (Cytiva, catalogue no. 10600023. The membrane was cut into three parts: top part, MTF-1 protein, ~115 KDa; middle part, α-Tubulin, 50 KDa; and bottom part MT proteins,15-38 KDa. Blots were then blocked with 5% milk in TBST (tris-buffered saline with 0.1% Tween-20) solution and treated with primary antibodies (1:500 anti MTF-1, 1:1000 anti-MT, 1:1000 anti-tubulin in 5% milk in TBST) for 1h at room temperature. After washing four times with

TBST, the corresponding secondary antibody (goat anti mouse:1:20K in 5% milk in TBST; goat anti-rabbit 1:10K in 1% milk in TBST) was added to respective blots. Blots were exposed to Amersham ECL Prime Western Blotting Detection Reagent (Thermo Scientific) for 3 min to visualize the presence of bound antibodies and imaged on ImageQuant LAS4000 imager (GE Healthcare Life Sciences).

Live cell imaging

For long term live cell imaging, MCF10a WT cells expressing NES/NLS ZapCV2 and zinc dead sensor were counted with a Countess II Automated Cell Counter (Thermo Fisher Scientific, Waltham, MA) and plated at a density of 4000 cells/well for ZD, MM, ZR15, and ZR30 conditions in minimal medium for 24 hr before imaging in glass bottom 96-well plates (P96-1.5H-N, Cellvis, Mountain View, CA). For the serum starvation experiment, MCF10a cells expressing NES-ZapCV2, H2B-HaloTag, and DHB-mCherry were plated at a density of 4000 cells/well in serum starvation media and allowed to synchronize for 48h before imaging. Scr Ctrl and MTF-1 KD cells were plated at a density of 3,500 cells/well for MM, ZR15, ZR30 and ZR50 conditions and plated at 4000 cells/well for ZD3, ZD2 condition. After plating the cells, the plate was kept undisturbed in the biosafety cabinet for 45 minutes to ensure cells settle at the center of wells. This starting density was chosen to avoid significant contact inhibition during the imaging period for ZD and ZR conditions. In all imaging experiments other than the media change experiment and serum starvation experiment, cells were imaged in MM and 2X media of each condition (ZD, MM, ZR) was added immediately prior to imaging. For the media change experiment (Figure 2.9), cells were imaged in MM for 24h first and then 2X respective MM, ZR and ZD medium was added and imaging was continued for another 24 hours. Cells expressing Halo-Tag construct were incubated with 5 nM JF669 Halo-Tag dye for 15 min and washed twice before imaging. For the serum starvation experiment, cells were imaged in serum starvation media for 4 hours, then the media was changed to MM for an additional 44h.

Images were collected using a Nikon Ti-E High Content Analysis inverted microscope with a Lumencor SPECTRA X light engine (Lumencor, Beaverton, OR) and Hamamatsu Orca FLASH-4.0 V2 cMOS camera (Hamamatsu, Japan). Images were collected in time lapse series every 12 min with a 10X air, 0.45 NA Plan Apo objective lens (Nikon Instruments, Melville, NY). During imaging, cells were in a controlled environmental chamber surrounding the microscope (Okolab Cage Incubator, Okolab USA INC, San Bruno, CA) at 37°C, 5 % CO_2 and 90 % humidity. Filter sets (excitation = Ex, emission = Em) used for live-cell imaging were as follows: CFP Ex: 440, 455 dichroic, Em: 480/20, power 50, exposure 500 ms; YFP Ex: 508, 518 dichroic, Em: 540/21; CFP/YFP FRET Ex: 440, 455 dichroic, Em: 540/21, power 50, exposure 500 ms; mCherry Ex: 555, 597 dichroic, Em: 595/40, power 50, exposure 200 ms; and Cy5 Ex: 640, 640 dichroic, Em: 705/22, power 50, exposure 500 ms.

FRET sensor calibration and analysis

In situ calibrations involve measuring the resting FRET ratio (R) in individual cells followed by addition of the cell permeable Zn^{2+} chelator TPA which removes any Zn^{2+} bound to the sensor, resulting in the minimum FRET ratio (R_{min}). Subsequently, the sensor is saturated by addition of excess Zn^{2+}, saponin, and pyrithione to measure the maximum FRET ratio (R_{max}). Sensor calibrations of MCF10a cells stably expressing PB-NES-ZapCV2 or PB-NES-dead-ZapCV2 were performed using the Nikon Ti-E HCA. Cells were grown for 24 h in either MM, or ZR (50 µM $ZnCl_2$) media. Before starting the experiment, cells were incubated with 10 nM JF669-HaloTag dye for 15 min in phosphate free HEPES-buffered Hanks' Balanced Salt Solution (HHBSS) buffer and washed thrice. Cells were then equilibrated at room temperature in a phosphate-free HHBSS buffer for 30 min. For collection of R_{rest}, cells were imaged for CFP-YFP FRET (power 20, 200 ms exposure) and CFP (power 20, 200 ms exposure) every 30 s for several min. To collect R_{min}, 100 μM TPA in 1mL of phosphate-free HHBSS was added to the cells in 1mL of phosphate-free HHBSS (final concentration 50 μM TPA). Cells were imaged for 5 min at 30 s intervals. Cells were then washed three times with phosphate-, calcium-, and magnesium-free HHBSS pH 7.4 to remove TPA. Finally, cells were treated with 104 nM buffered Zn^{2+} solution, 0.001% saponin, and 750 nM pyrithione in phosphate-free HHBSS for collection of R_{max}, as previously described. All experiments were performed in replicates (n=3 biological replicates). The average R_{rest} and R_{min} were calculated by averaging across the time points collected. The maximum FRET ratio achieved after Zn^{2+} addition was used as R_{max}. Images were either background corrected by drawing a region of interest in a dark area of the image and subtracting the average fluorescence intensity of the background from the average intensity of each channel or the images were background subtracted and processed via a MATLAB pipeline.

FRET ratios for each cell were calculated with the following equation:

$$FRET\ ratio\ = \frac{I_{CFP\ ex\ YFP\ em}}{I_{CFP\ ex\ CFP\ em}}$$

Where $I_{CFP\ ex\ YFP\ em}$ is the background-corrected intensity in the FRET channel, and $I_{CFP\ ex\ CFP\ em}$ is the background-corrected intensity of the donor channel.

The dynamic range (DR) of the sensor in each condition was calculated as:

$$DR\ = \frac{R_{max}}{R_{min}}$$

The fractional saturation (FS) of the sensor in each condition was calculated as:

$$FS\ = \frac{R_{rest}\ -\ R_{min}}{R_{max}\ -\ R_{min}}$$

Finally, Zn^{2+} concentrations were calculated using the following equation:

$$[Zn^{2+}]_{free}\ = K_d\left[\frac{R_{rest}\ -\ R_{min}}{R_{max}\ -\ R_{rest}}\right]^{\frac{1}{n}}$$

where the dissociation constant (K_d) = 5.3 ± 1.1 nM and n = 0.29 (Hill coefficient) were reported previously.

Calculation of [Zn^{2+}] during the Zn^{2+} pulse

To estimate the mean free Zn^{2+} during the Zn^{2+} pulse, as well as the lower and upper limits of this estimate, we used equation **(3)** where dissociation constant (K_d) = 5.3 nM, Hill coefficient (n) = 0.29, minimum FRET ratio (R_{min}) is the FRET ratio of ZD3 treatment, and a dynamic range (DR) = 1.45, 1.55, 1.65 for estimating upper bound, mean, and lower bound of free zinc, respectively (Table 1). These numbers are based on the calibrations of ZapCV2 in Figure 2.6.

CellTiter-Glo luminescent viability assay

MCF10a Scr-Ctrl and MTF-1 KD cells stably expressing NES-ZapCV2 and H2B-HaloTag were plated at a density of 3500 cells/well in a glass bottom black 96 well plate in minimal media. After 24h, 100μL media was removed from each well and replaced with 100 μL of 2X concentration of ZD3, ZD2, fresh MM, ZR15, ZR30 and ZR50 media. After 48h of incubation, 100 μL media was again removed and 100 μL of 1:1 solution of CellTiter-Glo cocktail A&B was added. The 96 well plate was shaken on a gel rocker for 30 min for proper mixing and luminescence was recorded on a Molecular Devices SpectraMax iD3 plate reader. Background luminescence intensity was recorded from wells with no cells. To quantify the cell viability, the luminescence intensity was background subtracted and the mean luminescence was calculated from triplicate measurements. All results were normalized to the average luminescence intensity from Scr-Ctrl cells grown in minimal media.

Annexin V apoptosis assay

MCF10a WT, Scr-Ctrl and MTF-1 KD cells were plated in minimal media in 6 well plates at a similar density. After 24 h, Scr-Ctrl and MTF-1 KD cells were treated with ZR15, ZR30 or ZR50 and incubated for either 24 h or 48h. MCF10a WT cells were incubated with an apoptosis inducing agent, camptothecin (6 µM, positive control) for 12h. After incubation, the respective media were transferred to properly labeled tubes which was then followed by PBS(1X) washes and trypsinization for 10 min. After trypsinization, the media was collected and the cell suspension was centrifuged for 5 min at 1000 rpm. Cell pellets from the positive control, MM and ZR conditions were treated with Hoechst 33258 (0.1 µg/mL in PBS) and Annexin V Alexa Fluor 647 apoptosis assay reagents for 30 min. After 30 min of incubation, cells were analyzed on a BD FACSAria Fusion instrument and data were processed with BD FACSDiva v8 software (BD Biosciences, San Jose, CA). DAPI: Ex 355 nm, Em 470/15 nm, Alexa 647 nm: Ex 637 nm, Em 670/30 nm. Depending on the response with the positive control, a gate was selected which describes the P2 Annexin V positive population. The P2 population defines total apoptotic cells including early apoptotic (Q2) and late apoptotic cells (Q4) which was then used to determine the percentage of apoptotic cells in different conditions.

Image Processing

Live-cell imaging experiments were analyzed using the EllipTrack cell tracking pipeline in MATLAB 2017a and 2020b on the institutional computing cluster (182). Briefly, EllipTrack requires several generalized parameters for cell segmentation, tracking and event identification. The advanced parameters were unchanged from the original code accessible on Github. The parameters that were fine-tuned are listed below:

<u>Training data</u>: Training data sets for the EllipTrack event predictions were made using at least 500 events across each time series for both H2B-HaloTag and H2B-mCherry.

Segmentation: We used a nuclear radius of 12 pixels as the average size of one cell. The ellipse that is fitted to this nucleus was required to be at least 25 pixels in area. Images were log transformed and a blob detection algorithm was used to identify nuclei with a blob threshold of -0.075. Objects were separated using a watershed algorithm and ellipses were fitted to each object.

Prediction of events: Mitoses were inferred based on morphological properties of each object before and after a potential mitosis event. Migration and migration speed was inferred using a density-dependent migration speed from the training data.

Track linking: All tracks greater than 10 frames were kept, and tracks were allowed to skip at most two frames.

Signal extraction: Intensity information from nuclear localized reporters was extracted using the nuclear mask. The intensity of cytoplasmic sensors was calculated in a three-pixel wide cytosolic ring around the nuclear mask.

Data Analysis

Mother and daughter tracks from the output structure of EllipTrack were linked together by at least one mitosis event. Tracks containing CFP, FRET (CFP excitation YFP emission), H2B intensity, and mitosis information were smoothed using a moving mean of a five-frame window, then fed into a custom pipeline. This pipeline is available at https://github.com/samholtzen/live-cell-zinc-sensor.git. The tracks were then processed as laid out below.

Proliferation: EllipTrack approximates nuclei as ellipses and uses these fitted ellipses for cell tracking. Since one MCF10a cell virtually always contains one nucleus, we used the number of ellipses at each frame as a proxy for cell count. To correct for plating density, the cell count of the entire time lapse was divided by the first frame.

FRET Calculation: Since ZapCV2 is a FRET-based sensor, we calculated the FRET ratio in the following manner:

$$FRET\ ratio\ = \frac{I_{CFP\ ex\ YFP\ em}}{I_{CFP\ ex\ CFP\ em}}$$

Where $I_{CFP\ ex\ YFP\ em}$ is the background-corrected intensity in the FRET channel, and $I_{CFP\ ex\ CFP\ em}$ is the background-corrected intensity of the donor channel. Tracks with a FRET ratio of greater than 8 or less than 3 at any point in the time-lapse were discarded from further analyses.

Average FRET Ratio: To identify long-term changes in labile Zn^{2+} levels in cells cultured in media containing different amounts of Zn^{2+}, we averaged the FRET ratio of single cell tracks across the entire time-lapse. Cells were then aligned to mitosis using all mitosis events detected by EllipTrack in each condition. The average FRET ratio of these aligned tracks at each timepoint was plotted. The resting FRET ratio was calculated by taking the average FRET ratio of frame -20 to frame -10 relative to mitosis to avoid any fluctuations immediately before mitosis. The peak FRET ratio was calculated by taking the maximum FRET ratio of the ten frames after mitosis, including the mitosis frame. Data analysis was done in MATLAB and GraphPad Prism.

Serum Starvation Analysis: The cytoplasm/nucleus (C/N) ratio for the DHB-mCherry sensor was calculated by taking the background corrected signal in the cytosol and dividing it by the background corrected signal in the nucleus. Tracks had to exist for the full time-lapse in order to be considered for analysis. Tracks also had to have a CDK2 activity of between 0.2 and 2, as was determined by analyzing the dynamic range of this particular construct. Cells finally had to have signal from both the NES-ZapCV2 sensor and the DHB-mCherry sensor. Clustering of DHB-mCherry signals using k-medoids and pairwise dynamic time warping (DTW) was done in MATLAB using standard parameters. The median DHB-mCherry signal and the mean FRET signal were plotted along with the 95% confidence interval. Each track was aligned to either the first and second mitoses and the average FRET ratio was plotted accordingly.

Quantification and statistical analysis

All statistical analyses were done in GraphPad prism. Figures were created in either Biorender or Adobe Illustrator. Two-way ANOVA with Tukey-Kramer test was performed in Figure 2.6. Statistical analyses were performed on the medians using non-parametric unpaired two-tailed Mann Whitney test (with 99% confidence level) in Figure 2.7. All other statistical analyses were done using a one-way ANOVA followed by multiple t-tests. Multiple hypothesis correction was applied using the Dunn-Šidák method. Significance was determined using an alpha value of 0.05.

For Figure 2.9D-F, analyses were conducted using subsampling, similar to bootstrapping. A sampling of 100-300 random tracks from each time lapse was passed through a function that averaged the tracks and extracted maximum FRET, time of maximum FRET, and steady-state FRET for this average track. This was done 20 times to generate 20 subsampled data points per condition.

2.7 Acknowledgements

I would like to acknowledge NIH Director’s Pioneer Award DP1-GM114863 (A.E.P.), NIGMS MIRA R35 GM139644 (A.E.P), and Anna and John J. Sie Foundation Postdoctoral fellowship (M.N.L) for generous financial support. I thank the University of Colorado Flow

Cytometry Core, which performed cell sorting, the University of Colorado Biochemistry Cell Culture Core (specifically Theresa Nahreini) for assistance with cell culture, and the BioFrontiers Computing Core and BioFrontiers IT for providing High Performance Computing resources. I thank Dr. Luke Lavis (HHMI Janelia) for the JF669-HaloTag dye.

Chapter 3: Transient Zn^{2+} deficiency induces replication stress and compromises daughter cell proliferation

3.1 Publication Status

Holtzen, S. E.; Navid, E.; Kainov, J.; Palmer, A.E.; “Transient Zn^{2+} deficiency induces replication stress and compromises daughter cell proliferation” Manuscript in revision at Proceedings of the National Academy of Sciences.

Conceptualization, Methodology, A.E.P. and S.E.H.; Investigation, S.E.H, E.N., J.K.; Writing – Original Draft S.E.H.; Writing – Review and Editing A.E.P. and S.E.H.; Formal Analysis, S.E.H.; Software, S.E.H; Funding Acquisition, Supervision, Project Administration, A.E.P.

3.2 Abstract

Cells must replicate their genome quickly and accurately, and they require metabolites and cofactors to do so. Ionic zinc (Zn^{2+}) is an essential micronutrient that is required for hundreds of cellular processes, including DNA synthesis and adequate proliferation. Deficiency in this micronutrient impairs DNA synthesis and inhibits proliferation, but the mechanism is unknown. Using fluorescent reporters to track single cells via long-term live-cell imaging, we find that Zn^{2+} is required at the G1/S transition and during S-phase for timely completion of S-phase. A short pulse of Zn^{2+} deficiency impairs DNA synthesis and increases markers of replication stress. These markers of replication stress are reversed upon resupply of Zn^{2+}. Finally, we find that if Zn^{2+} is removed during the mother cell’s S-phase, daughter cells enter a transient quiescent state, maintained by sustained expression of p21, which disappears upon reentry into the cell cycle. In summary, short pulses of mild Zn^{2+} deficiency in S-phase specifically induce replication stress, which causes downstream proliferation impairments in daughter cells.

3.3 Introduction

The mammalian cell cycle is composed of several mostly irreversible ratchet-like steps that prepare a cell for division (212–214). Mother cells must grow and license origins of replication in G1, replicate their genome efficiently and accurately in S-phase, and ensure that each genome is duplicated once and only once in G2 before dividing into two daughter cells. In response to stress, loss of adhesion, DNA damage, or mitogen withdrawal, cells may elongate any one of these phases or temporarily leave the cell cycle and enter a quiescent state after division, termed G0 (80, 215–217). Cells constantly evaluate their intra- and extracellular state, including metabolite, nutrient and energy balance, and integrate these signals to make go/no-go decisions at the transition between each of these phases (80, 218, 219).

Ionic zinc (Zn^{2+}) is required for human health (220). Ten percent of human genes are predicted to encode proteins that have one or more Zn^{2+} binding sites, where Zn^{2+} is suggested to play a role in structure stabilization, catalysis, or signaling (9). Recently, we established that Zn^{2+} is an important and enigmatic signaling ion in regulation of cellular processes. For example, cells transiently increase their cytosolic labile Zn^{2+} in early G1, and require optimal labile Zn^{2+} for proliferation (10). Further, elevation of cytosolic Zn^{2+} activates flux through the mitogen-activated protein kinase (MAPK) pathway, and induces changes in transcription in mouse hippocampal neurons (12, 14). At a cellular level, deficiency of this essential micronutrient can cause a loose constellation of varied symptoms such as DNA synthesis impairment, oxidative stress, and apoptosis (100, 109, 112, 154). Several studies have attempted to dissect how Zn^{2+} deficiency can cause its hallmark effects in humans through the lenses of DNA synthesis, cell cycle protein expression and the DNA damage response (100, 102, 103, 199). In all of these studies, researchers found that Zn^{2+} deficient cells are unable to proliferate.

Early studies identified the requirement of Zn^{2+} for DNA synthesis and proliferation in several cell types (100, 102), and determined that treating cells with an extracellular Zn^{2+} chelator inhibits proliferation through inhibition of cyclin mRNA expression (103). More recent work has determined that MCF10a cells experiencing mild Zn^{2+} deficiency bifurcate into two populations after cell division depending on how long they were Zn^{2+} deficient before dividing (13). In the first population, cells enter quiescence and are able to enter the cell cycle again upon resupply of Zn^{2+}. This population seems to increase in abundance with the duration of Zn^{2+} deficiency. In the second population, cells are able to pass the restriction point, only to stall in a proliferative state characterized by hyperphosphorylation of the Rb protein, indicating these cells are indeed committed to another cell cycle but unable to complete it.

These studies pose several unanswered questions. Since cells bifurcate into two populations after division depending on how long cells were exposed to Zn^{2+} deficiency, is Zn^{2+} required at specific phases of the cell cycle, or do cells integrate time spent in Zn^{2+} deficiency to determine cell fate? What causes Zn^{2+} deficient cells to accrue DNA damage and show decreased DNA synthesis? Finally, what molecular processes contribute to the daughter cell proliferation/quiescence decision? Using a combination of fluorescent reporters for single-cell tracking, long term live-cell imaging, immunofluorescence, and flow cytometry, we show that Zn^{2+} is required at the G1/S transition and in S-phase for timely S-phase completion. We then show that a short pulse of mild Zn^{2+} deficiency reversibly inhibits DNA synthesis, leads to accumulation of replication protein A subunit 2 (RPA2) foci, and activates the S-phase checkpoint. Analysis of likely causes of replication stress implicates an essential role for Zn^{2+} in the function of DNA polymerase. Finally, we show that Zn^{2+} deficiency in the mother cell's S-phase induces temporary daughter cell quiescence through sustained expression of p21. Together, our results indicate that acute, mild, and temporary Zn^{2+} deficiency in S-phase, but not other cell cycle phases, causes reversible replication stress, which leads to daughter cell entry into quiescence after division.

3.4 Results

3.4.1 Zn^{2+} is required at the G1/S transition and in S-phase for normal S-phase progression

Zn^{2+} deficient cells show a bifurcation in cell fate after cell division, shifting their fate away from proliferation and towards quiescence with increased duration of Zn^{2+} withdrawal (13). To simulate mild Zn^{2+} deficiency, previous work used the membrane permeable Zn^{2+} chelator tris(2-pyridylmethyl)amine (TPA) in culture media, which lowers the labile Zn^{2+} levels in MCF10a cells from 80 pM to 1 pM (10, 13). In this study, two factors confound the interpretation: the timing and the duration of the treatment. To address this, we used a pulse-chase treatment strategy coupled with the FUCCI (CA) sensor, which is able to resolve cell cycle phase boundaries and therefore allow accurate measurement of cell cycle phase lengths (175). The sensor is composed of two fluorescent proteins fused to fragments of human Cdt1 and Geminin proteins, which are reciprocally ubiquitinated and degraded in a cell cycle phase specific manner (Figure 3.1A) (175). Using long-term live-cell imaging, we tracked MCF10a cells through several cell divisions using a published pipeline (182), extracted single-cell fluorescence intensities of the two probes and identified the cell cycle phase at each frame (Figure 3.1B).

We pulsed MCF10a cells expressing the FUCCI (CA) sensor with Zn^{2+} deficient media containing 3μM TPA for 2 or 4 hours, then chased with Zn^{2+} adequate media. After cell tracking and signal extraction, we were able to identify changes in cell cycle phase lengths as a function of Zn^{2+} deficiency duration. If Zn^{2+} was withdrawn from cells at the G1/S transition and in S-phase, cells had significantly longer S-phases than untreated cells (Figure 3.1C,E-F). This effect increased with the duration of Zn^{2+} withdrawal. If Zn^{2+} was withdrawn and replaced while cells were still in G1, there was no effect on the subsequent S-phase, indicating that Zn^{2+} is not

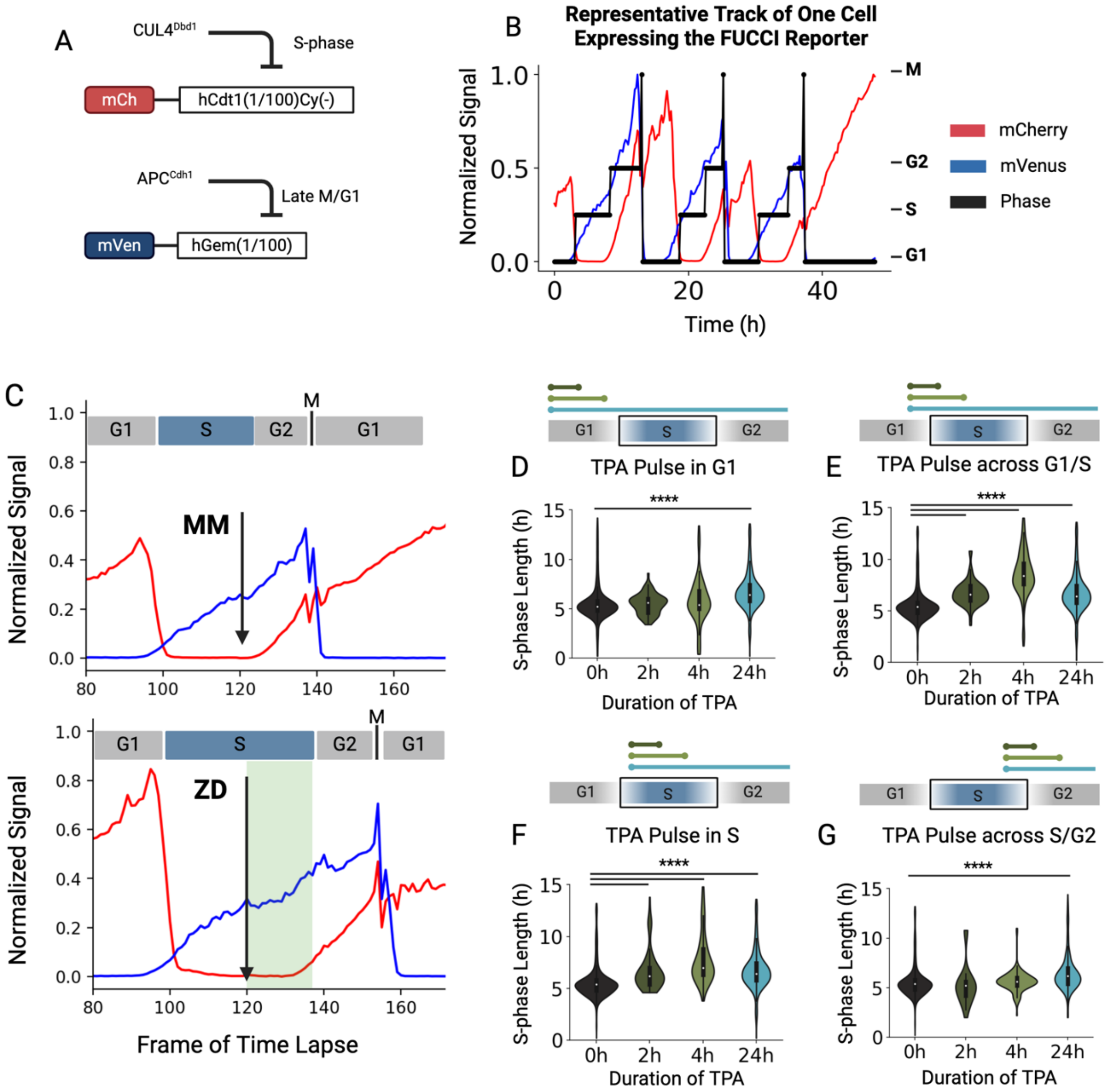

Figure 3.1: Cells treated with Zn^{2+} deficient media across the G1/S transition and during S-phase have an elongated S-phase. (A) A schematic of the FUCCI (CA) sensor mechanism of operation. The mCherry and mVenus fluorescent proteins are conjugated to fragments of the human Cdt1 and human Geminin proteins, which are reciprocally targeted for degradation by the $CUL4^{Dbd1}$ and APC^{Cdh1} ubiquitin ligases during S-phase and G1, respectively. (B) A representative track of a cell expressing the FUCCI (CA) sensor throughout three cell cycles. The mCherry and mVenus intensities are min-max normalized. The cell cycle phases assigned *in silico* are shown as the black stair-step lines. (C) Representative traces of cells treated with MM media (top) or ZD media (bottom) during S-phase. Shaded area represents the duration and timing of ZD exposure. (D) S-phase lengths of cells exposed to ZD media during G1, and whose Zn^{2+} was resupplied in G1. (E) S-phase lengths of cells exposed to ZD media across the G1/S transition. (F) S-phase lengths of cells exposed to ZD during S-phase, and whose Zn^{2+} was resupplied in S-phase. (G) S-phase lengths of cells exposed to ZD across the S/G2 transition. **** = $p<0.001$. n=3 biological replicates. Colored bars above the cell cycle phase diagrams indicate the timing and duration of the Zn^{2+} deficiency pulse.

required in G1 for timely S-phase completion (Figure 3.1D). Similarly, if Zn^{2+} was withdrawn in S-phase and resupplied in G2, S-phase was not elongated, implying that Zn^{2+} is not required in late S-phase for timely S-phase progression (Figure 3.1G). Together, these data illustrate a specific Zn^{2+} requirement at the G1/S transition and in S-phase for timely S-phase progression, and that a process at this stage is disrupted when deprived of adequate Zn^{2+}.

3.4.2 Zn^{2+} deficient cells show impaired DNA synthesis

After 24 hours of Zn^{2+} deficiency, proliferative daughter cells show strongly impaired DNA synthesis rates compared to Zn^{2+} replete cells (13). Other studies have shown that Zn^{2+} is required for DNA synthesis in a number of cell types (100, 102). Since we saw an impaired S-phase in mother cells exposed to pulses of Zn^{2+} deficiency, we wanted to determine whether this elongated S-phase is coupled with inhibited DNA replication. We therefore used a pulse of 5-ethynyl-2′-deoxyuridine (EdU) coupled with click-chemistry mediated addition of a fluorescent dye and flow cytometry to measure DNA synthesis rate of single cells (4). In brief, cells were incubated with the Zn^{2+} chelator TPA for two or four hours, then exposed to EdU to measure incorporation of EdU within a defined time window. After fixation and counterstaining with DAPI for DNA content, we were able to identify DNA synthesis rate in single cells (221). We found that two hours of Zn^{2+} deficiency inhibits DNA synthesis by half, and that this inhibition is also observed during a four hour pulse of Zn^{2+} deficiency (Figure 3.2A-B). Resupply of Zn^{2+} fully reverses the DNA synthesis inhibition, demonstrating this DNA synthesis defect is reversible (Figure 3.2B).

3.4.3 Zn^{2+} deficient cells show signs of replication stress

Impaired DNA synthesis during S-phase is termed replication stress, and can be due to several disparate factors such as DNA adducts (222, 223), nucleotide depletion (219, 224), or inhibition of the DNA polymerase (225, 226). Inhibition of the DNA polymerase and DNA lesions

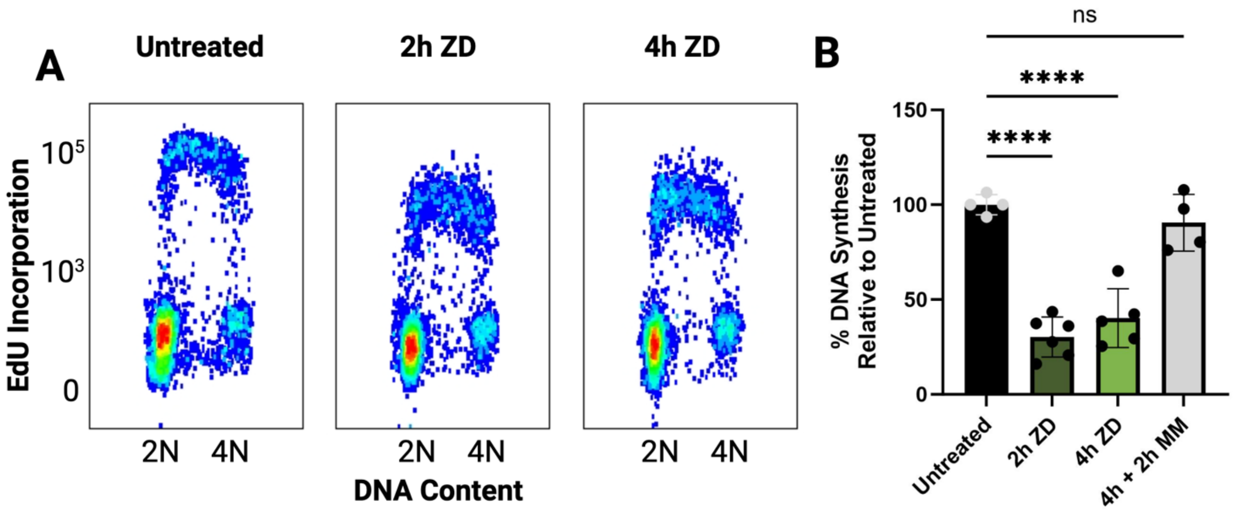

Figure 3.2: Zn^{2+} deficient cells show impaired DNA synthesis. (A) Flow cytometry plots showing Zn^{2+} adequate and Zn^{2+} deficient cells treated with the nucleotide analog EdU to probe DNA synthesis rate, then counterstained with the DNA content dye DAPI. Each point represents a single cell. (B) Quantification of the plots in A. Each point is the median EdU signal of S-phase cells (EdU+) in one replicate. All data was then normalized to the untreated condition. Error bars represent the 95% confidence interval. *** = $p < 0.005$, **** = $p < 0.001$. $n \geq 4$ biological replicates.

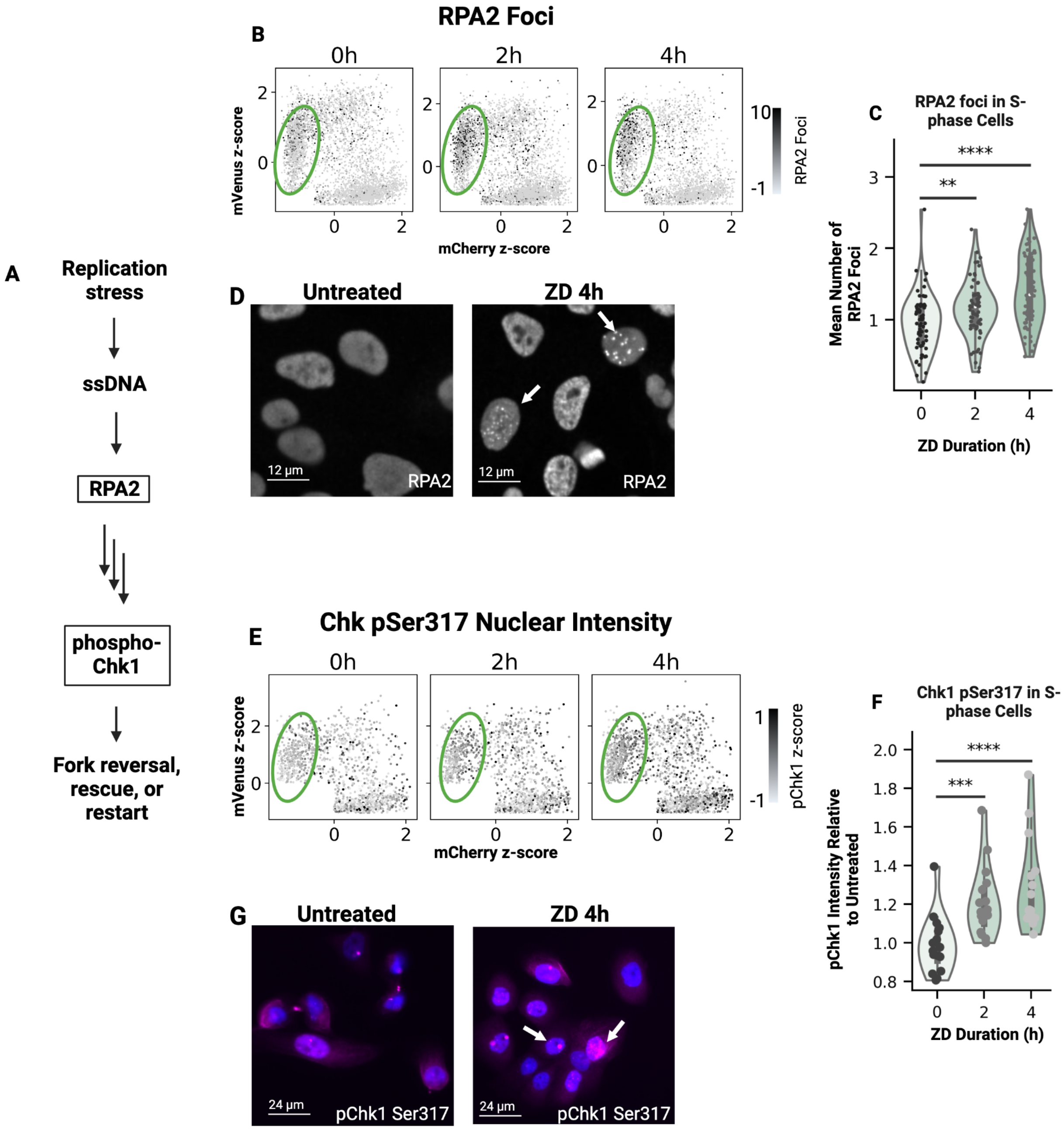
A
Replication stress
ssDNA
RPA2
phospho-Chk1
Fork reversal, rescue, or restart
B
RPA2 Foci
0h
2h
4h
mVenus z-score
mCherry z-score
RPA2 Foci
10
-1
C
RPA2 foci in S-phase Cells
Mean Number of RPA2 Foci
ZD Duration (h)
****
**
D
Untreated
ZD 4h
12 μm
RPA2
E
Chk pSer317 Nuclear Intensity
0h
2h
4h
mVenus z-score
mCherry z-score
pChk1 z-score
1
-1
F
Chk1 pSer317 in S-phase Cells
pChk1 Intensity Relative to Untreated
ZD Duration (h)
****
***
G
Untreated
ZD 4h
24 μm
pChk1 Ser317

Figure 3.3: Acute Zn^{2+} deficiency increases replication stress markers. (A) Pathway of sensing and response to replication stress. Replication stress causes accumulation of single-stranded DNA (ssDNA), which is coated by RPA2. Downstream proteins sense this accumulation and signal activation of Chk1 via phosphorylation, which activates effector proteins to stabilize and restart replication forks. (B) Quantitative imaging-based cytometry plots of mean nuclear fluorescence of the mCherry and mVenus construct of the FUCCI (CA) sensor on the horizontal and vertical axes, respectively. Each point is one cell, and the gray level of each point corresponds to the number of RPA2 foci it has. Green ovals indicate cells in S-phase. (C) Quantification of RPA2 foci in S-phase cells after treatment with Zn^{2+} deficient media. Each point is the average number of RPA2 foci in S-phase cells in one well of a 96-well plate. (D) Representative images of RPA2 foci in untreated cells and cells treated with Zn^{2+} deficient media for 4h. White arrows indicate cells with RPA2 foci. (E) Quantitative imaging-based cytometry plots of mean nuclear fluorescence of the mCherry and mVenus construct of the FUCCI (CA) sensor on the horizontal and vertical axes, respectively. Each point is one cell, and the gray level of each point corresponds to its mean nuclear phospho-Chk1 (Ser317) intensity. Green ovals indicate cells in S-phase. (F) Quantification of pChk1 signal in S-phase cells after treatment with Zn^{2+} deficient media. Each point is the average phospho-Chk1 (Ser317) signal in S-phase cells in one well of a 96-well plate. (G) Representative images of phospho-Chk1 (Ser317) signal in untreated cells and cells treated with Zn^{2+} deficient media for 4h. Blue indicates nuclear DAPI staining. Magenta indicates phospho-Chk1 Ser317 signal. White arrows indicate cells with phospho-Chk1 (Ser317) signal. ** = $p < 0.01$, *** = $p < 0.005$, **** = $p < 0.001$. $n \geq 2$ biological replicates.

can lead to uncoupling of the Cdc45, Mcm2–7, GINS (CMG) helicase from DNA polymerase (227, 228). This leads to long tracts of single-stranded DNA, which are rapidly coated by RPA2 (Figure 3.3A). In order for functional uncoupling between the CMG helicase and DNA polymerase to occur, the helicase must be active and the polymerase must be stalled (228, 229). To determine whether the CMG helicase is still active, but the polymerase is stalled by low Zn^{2+}, we measured whether RPA2 foci accumulate, which indicates single-stranded DNA accumulation. To do this, we pulsed cells expressing the FUCCI (CA) sensor with Zn^{2+} deficient media, then fixed and stained them for RPA2. To identify the cell cycle phases of each fixed cell, we used a Gaussian mixture model (GMM) with the *z*-score normalized mVenus and mCherry signal in each cell, then assigned each cell cycle phase by hand (Figure 3.4).

Exposure of cells to a 2 or 4 hr pulse of Zn^{2+} deficiency induced an increase in the number of RPA2 foci in S-phase cells, which increased with the duration of treatment (Figure 3.3B-D). RPA2 foci, much like DNA synthesis impairment, were resolved with resupply of Zn^{2+} (Figure 3.5). Because RPA2-bound single-stranded DNA leads to activation of the ATR-Chk1-p53 signaling pathway (228), we probed phosphorylation of the kinase at Ser317 by immunofluorescence. We found that a 2 hr or 4 hr pulse of Zn^{2+} deficiency increased Chk1 phosphorylation in S-phase along with RPA2 foci accumulation and DNA synthesis impairment (Figure 3.3E-G). These results indicate that RPA2 accumulation is accompanied by increased signaling through the Chk1 pathway in response to transient Zn^{2+} deficiency in S-phase.

3.4.4 Zn^{2+} deficiency does not cause double-stranded breaks, origin under-licensing, replication fork slowing, or an imbalance in the nucleotide pool

Since replication stress can be due to replication origin under licensing in G1 (105), it is possible that Zn^{2+} deficiency impaired licensing, which in turn could contribute to the accumulation

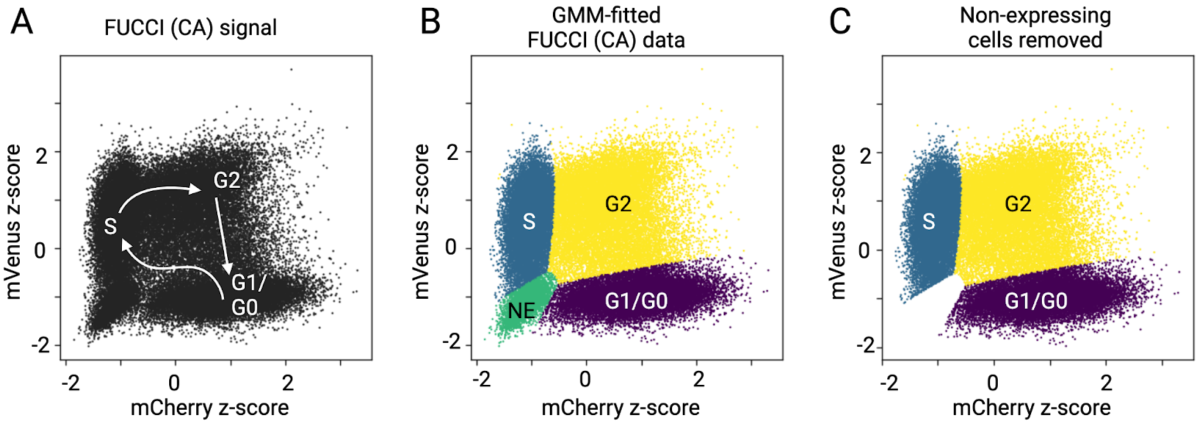

Figure 3.4: A Gaussian Mixture Model identifies cell cycle phases in fixed cells expressing the FUCCI (CA) sensor. (A) Quantitative imaging-based cytometry plots showing the z-score of mean nuclear fluorescence of single cells expressing the FUCCI (CA) sensor. Cells with low mVenus intensity and high mCherry intensity are in G1/G0. Cells with high mVenus intensity and low mCherry intensity are in S-phase. Cells with both high mVenus and mCherry intensities are in G2. Arrows indicate the trajectory of cells throughout the cell cycle in pseudotime. (B) A Gaussian mixture model was fitted to the data in A and cell cycle phases were color coded and assigned by hand. (C) Cells with low mVenus and low mCherry intensities were removed from further analysis.

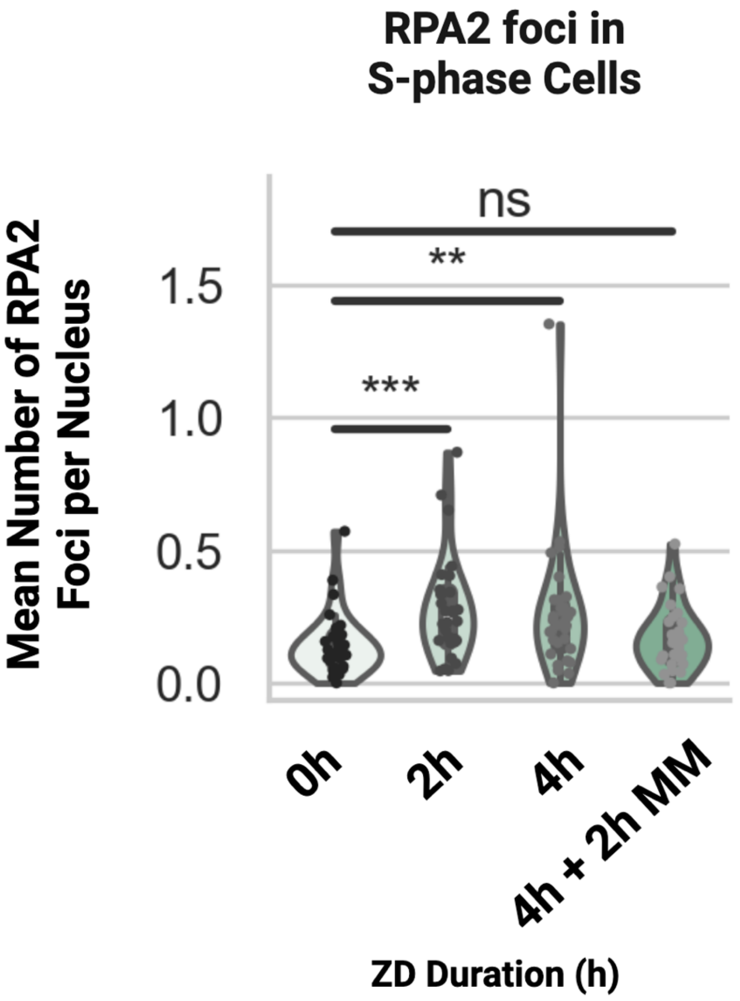

Figure 3.5: RPA2 foci in Zn^{2+} deficient cells resolve after resupply of Zn^{2+}. Violin plots of mean number of RPA2 foci per nucleus for cells in S-phase as determined by immunofluorescence. Zn^{2+} deficient duration on the horizontal axis. *** = $p < 0.005$, ** = $p < 0.01$, ns = not significant. n = 3 biological replicates.

of RPA2 foci. We tested whether Zn^{2+} deficiency causes under licensing of origins using a flow cytometry assay that probes for chromatin-bound MCM2 described previously (105). Transient Zn^{2+} deficiency did not cause under licensing of replication origins, further supporting that the MCM2 helicase is loaded at replication origins and is functional and that Zn^{2+} deficiency is not interfering with S-phase preparation (Figure 3.6).

ATR-Chk1 activation can decrease rates of DNA synthesis in response to replication stress (229). To determine whether the ATR-Chk1 signaling axis globally inhibited DNA replication under conditions of Zn^{2+} deficiency, we co-treating cells with Zn^{2+} deficient media and the Chk1 inhibitor CHIR-124 for 4 hours. After calculating the median EdU incorporation of each sample compared to the untreated controls, we found that, although DNA synthesis rate was slightly higher in cells treated with CHIR-124, it was not a full rescue as was the case with Zn^{2+} resupply (Figure 3.6E, Figure 3.2B). Therefore, Chk1 activation seems to be a consequence of Zn^{2+} deficiency-induced DNA synthesis impairment, not a cause of it.

Double-stranded breaks (DSBs) are genotoxic lesions that activate the DSB repair pathway mediated by the ATM/Chk2 signaling axis and repair the damage using non-homologous end joining or homologous recombination. DSBs in S-phase can induce replication stress through the ATM/Chk2 signaling axis, or through co-activation of Chk1 and Chk2 (216, 229, 230). To determine whether acute Zn^{2+} deficiency induces double-stranded breaks, we treated FUCCI(CA) expressing cells with Zn^{2+} deficient media and probed for 53BP1, a central player in the double-stranded break response, in fixed cells using immunofluorescence. We found that 4 hour Zn^{2+} deficiency does not increase 53BP1 foci relative to the untreated control in any cell cycle phase (Figure 3.7A). Further, we determined that 24 hour Zn^{2+} deficiency does not activate the checkpoint kinase Chk2 relative to the untreated control, indicating that Zn^{2+} deficiency does not

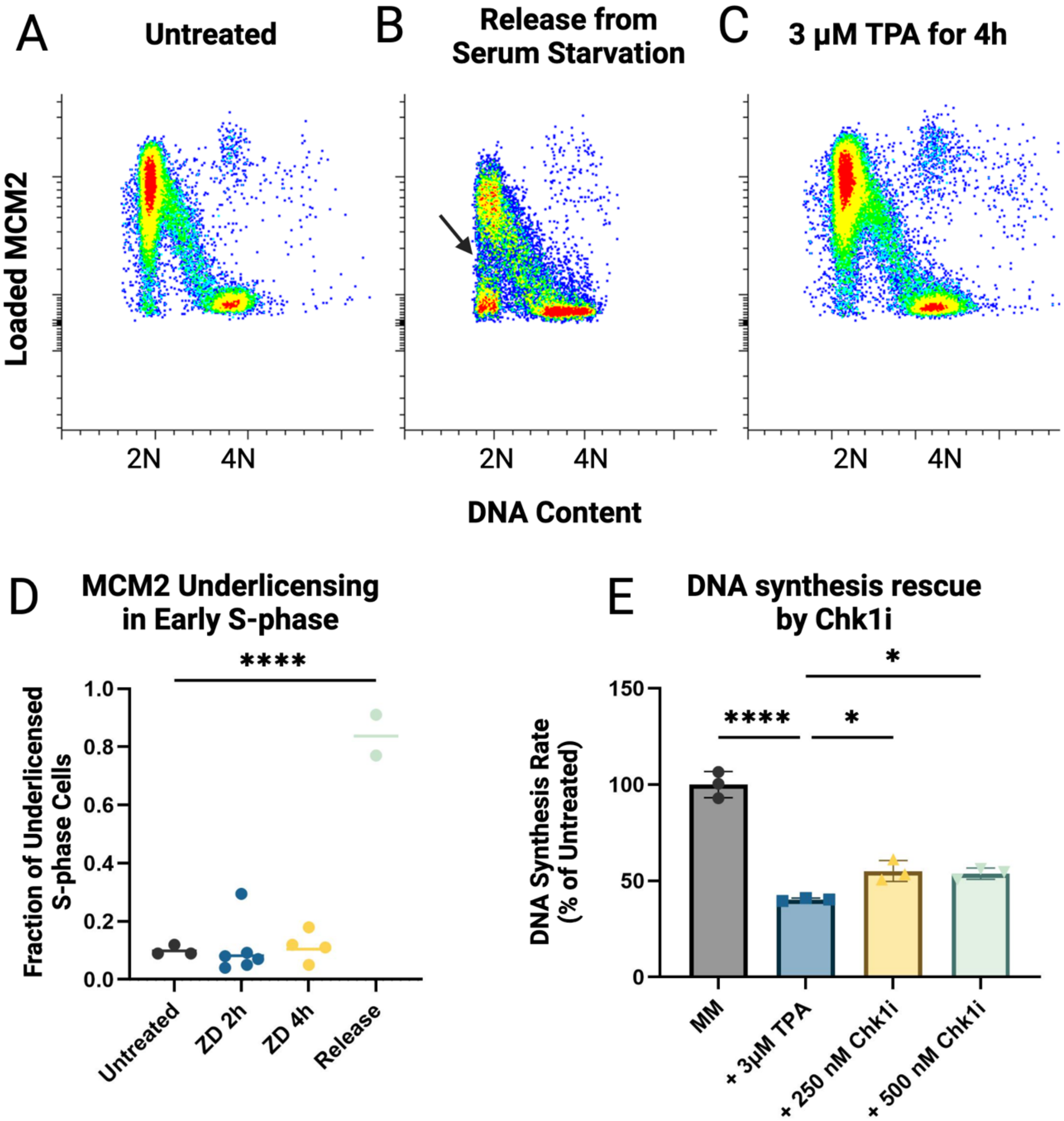

Figure 3.6: Zn^{2+} induced DNA synthesis impairment is not due to under licensing of origins of replication, nor is it fully due to origin firing inhibition by Chk1. (A) Flow cytometry plots of untreated cells showing chromatin loaded MCM2 and DNA content using single nuclei stained with an anti-MCM2 antibody and DAPI. Graphs show characteristic increase in MCM2 loading during G1, and decreased MCM2 loading throughout S-phase. (B) Flow cytometry plots of cells released from serum starvation showing chromatin loaded MCM2 and DNA content. Cells released from serum starvation show under licensing of replication origins, as shown with the arrow, and as shown previously. (C) Flow cytometry plots of Zn^{2+} deficient cells showing chromatin loaded MCM2 and DNA content. (D) Fraction of under-licensed S-phase cells in each condition using a previously established analysis scheme (105). (E) Quantification of DNA synthesis rate like that shown in Figure 3.2B. Cells were treated with 3μM TPA for 4h, or 3μM TPA and the Chk1 inhibitor CHIR-124, then probed for DNA synthesis rate using EdU. Each point is the median EdU signal of S-phase cells, normalized to untreated control. Error bars represent the 95% confidence interval. * = $p<0.05$, **** = $p < 0.001$. $n \geq 2$

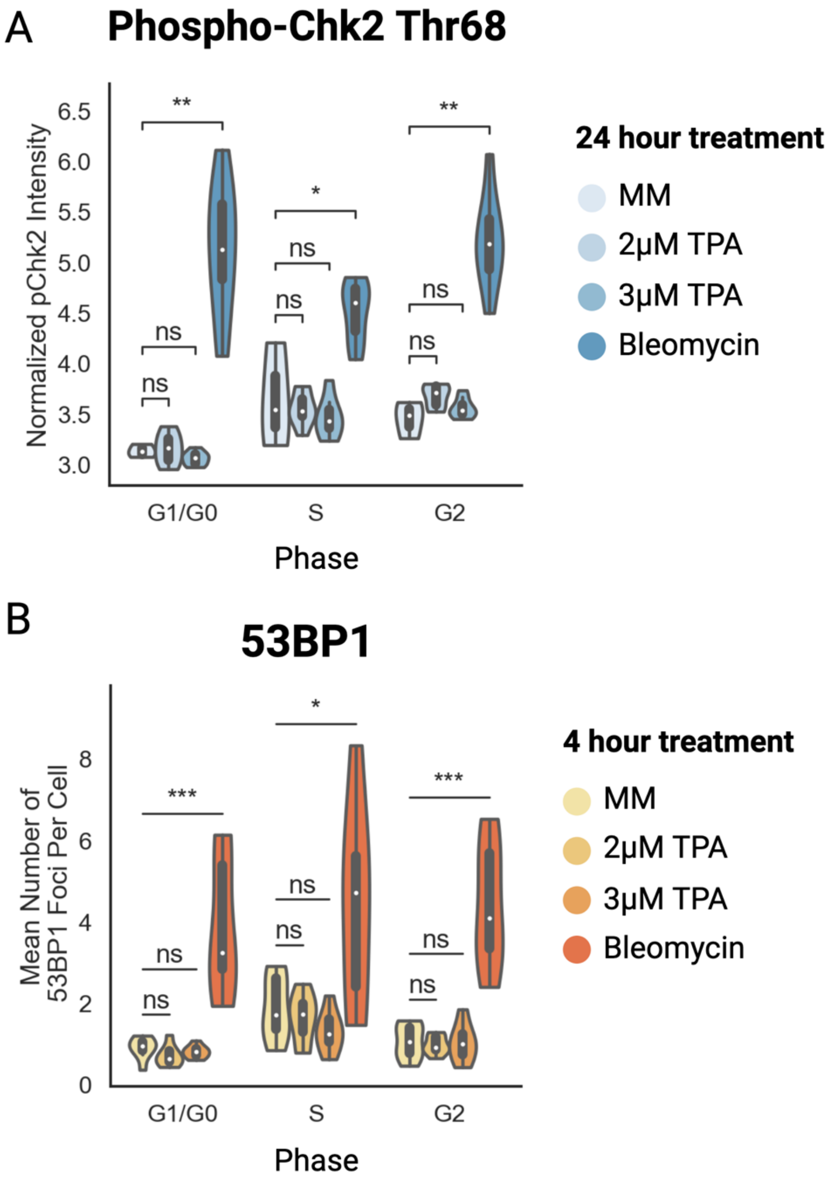

Figure 3.7: Zn^{2+} deficiency does not activate Chk2 nor does it induce double-stranded breaks (A) Quantification of 53BP1 foci in each cell cycle phase after four hour treatment with Zn^{2+} deficient media. Each data point is the average number of 53BP1 foci in cells in that phase in one well of a 96-well plate. Bleomycin 4μM is used as a positive control. (B) Quantification of phospho-Chk2 (Thr68) signal in S-phase cells after 24 hour treatment with Zn^{2+} deficient media. Each data point is the average log transformed nuclear Chk1 phospho-Thr68 in cells in that phase in one well of a 96-well plate. Bleomycin 4μM is used as a positive control. * = $p < 0.05$, ** = $p < 0.01$, *** $p < 0.005$. n = 3 replicates. Cell cycle phases identified using nuclear FUCCI (CA) signal and a Gaussian mixture model (GMM).

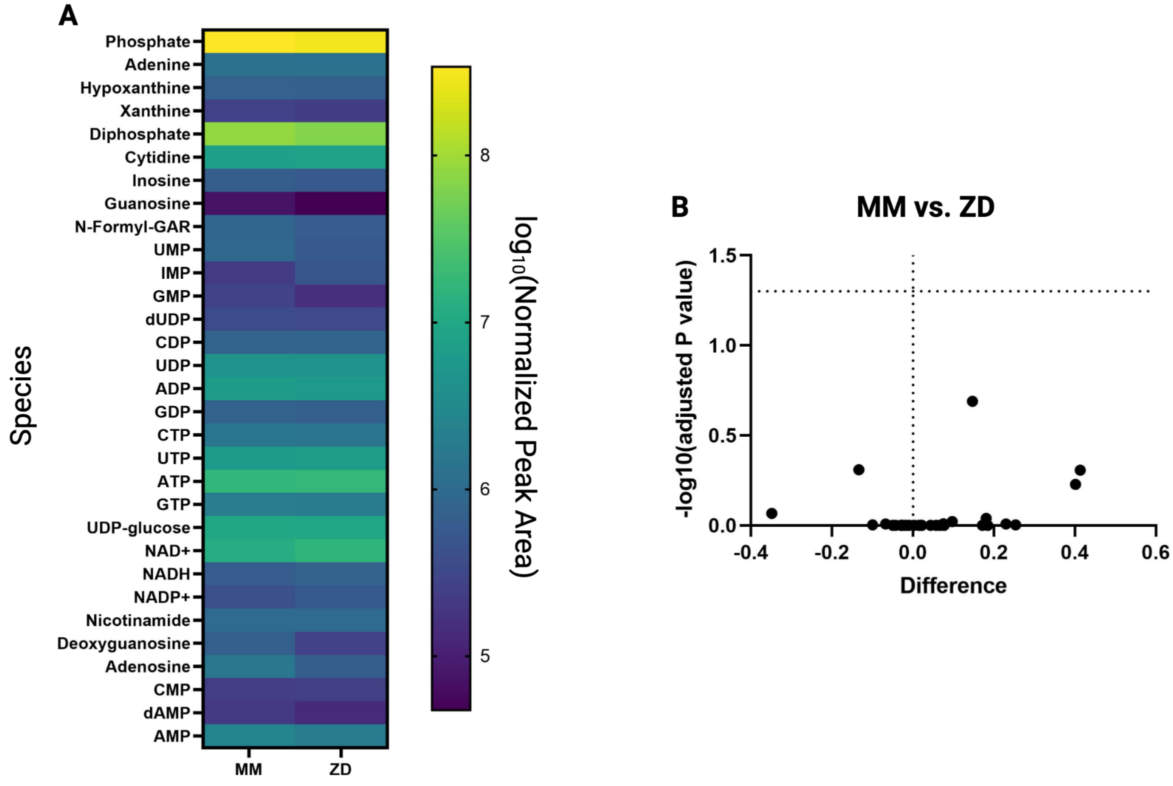

Figure 3.8: Zn^{2+} does not cause imbalance or depletion of nucleotides or their precursors. (A) Heatmap of the average log$_{10}$ peak area of each metabolite involved in the nucleotide biosynthesis pathway. MM indicates untreated cells, and ZD indicates cells treated with 3μM TPA for four hours. (B) A volcano plot showing changes in relative abundance of each species, and the adjusted P value for each. The P-values are adjusted using the Benjamini-Hochberg multiple hypothesis correction. The horizontal dotted line indicates threshold for significance. No species exceeds the adjusted P-value threshold of 0.05. Each condition contains n=5 biological replicates.

exert its effects through double-stranded break repair signaling, but rather through replication stress signaling (Figure 3.7B).

An imbalance in the intracellular nucleotide pool can activate the replication stress pathway via Chk1 (219, 224). To determine if acute Zn^{2+} deficiency changes the nucleotide pool, we conducted untargeted metabolomics of polar metabolites. We found that, although there were small changes in nucleotide precursors, there was no change in the concentrations of free nucleotides, nor in their deoxy counterparts (Figure 3.8). This indicates that Zn^{2+} deficiency does not impair DNA synthesis through depletion or imbalance of the nucleotide pool.

3.4.5 Transient Zn^{2+} deficiency during S-phase of the mother cell impairs proliferation of daughter cells

Cells integrate internal and external signals during the mother cell cycle in order to dictate daughter cell proliferation after division (80, 96). Since replication stress in the mother cell can inform daughter cell proliferation (215), we sought to identify the consequences of Zn^{2+}-deficiency-induced mother cell replication stress on daughter cell proliferation. To do this, we used an analysis technique presented in Min et al (80). This technique takes advantage of a CDK2 activity sensor's ability to resolve cell cycle commitment (Figure 3.9A) (78). After division, cells take on three fates: In the first, cells are born with a high CDK2 activity and hyper-pRb, which indicates that they are born committed to another cell cycle (Figure 3.9A, $CDK2^{inc}$, blue). In the second, cells are born with a low CDK2 activity, but cross the 0.5 arbitrary unit (AU) threshold and commit to another cell cycle sometime later (Figure 3.9A, $CDK2^{emerge}$, yellow). In the third, cells are born with a CDK2 activity below 0.5 and remain there for the rest of the time-lapse, indicating they are in a quiescent state that is not reversed during the time-lapse (Figure 3.9A, $CDK2^{low}$, red). Cell traces from asynchronously cycling cells can be aligned to mitosis such that the three populations

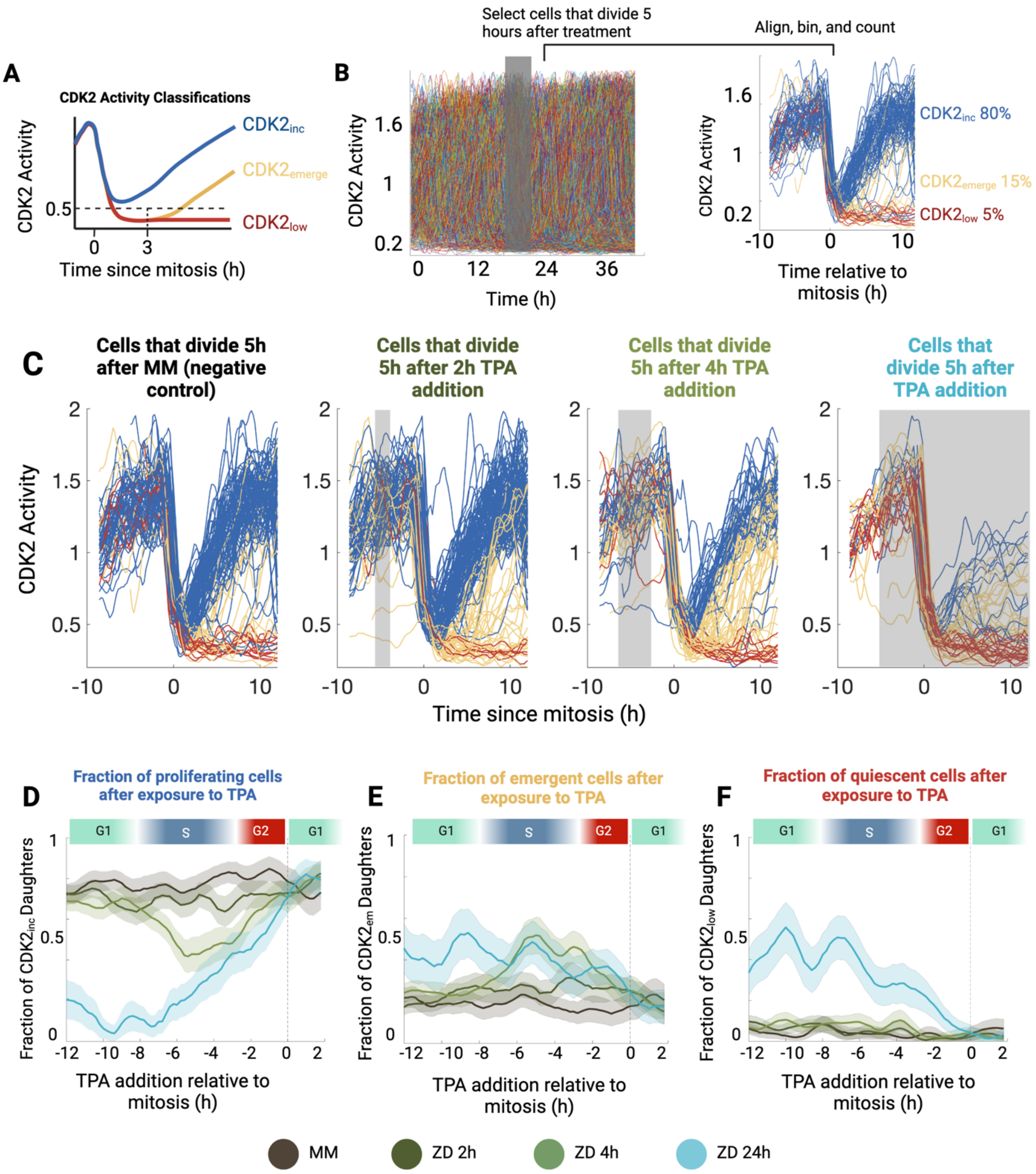
A
CDK2 Activity Classifications
CDK2 Activity
0.5
0
3
Time since mitosis (h)
CDK2inc
CDK2emerge
CDK2low
B
Select cells that divide 5 hours after treatment
Align, bin, and count
CDK2 Activity
1.6
1
0.2
0
12
24
36
Time (h)
-10
0
10
Time relative to mitosis (h)
CDK2inc 80%
CDK2emerge 15%
CDK2low 5%
C
Cells that divide 5h after MM (negative control)
Cells that divide 5h after 2h TPA addition
Cells that divide 5h after 4h TPA addition
Cells that divide 5h after TPA addition
CDK2 Activity
2
1.5
1
0.5
-10
0
10
Time since mitosis (h)
D
Fraction of proliferating cells after exposure to TPA
E
Fraction of emergent cells after exposure to TPA
F
Fraction of quiescent cells after exposure to TPA
G1
S
G2
G1
Fraction of CDK2inc Daughters
Fraction of CDK2em Daughters
Fraction of CDK2low Daughters
1
0.5
0
-12
-10
-8
-6
-4
-2
0
2
TPA addition relative to mitosis (h)
MM
ZD 2h
ZD 4h
ZD 24h

Figure 3.9: Zn^{2+} deficiency in the mother cell S-phase causes proliferation pause in daughter cells. (A) Schematic of the CDK2 activity sensor classifications. $CDK2^{inc}$ indicates a CDK2 activity that is higher than 0.5 after mitosis. $CDK2^{emerge}$ indicates a brief pause in G0, then entry into G1. $CDK2^{low}$ indicates an induction into quiescence that persists for the rest of the movie. (B) Analysis scheme of the CDK2 activity pulse-chase experiment. Cells are binned according to the time they divide relative to their treatment with TPA. Cells are then binned according to their CDK2 activity after division. Gray shaded area indicates treatment timing and duration. (C) Single-cell traces of cells expressing the CDK2 sensor aligned to mitosis. All cells shown were treated with Zn^{2+} deficient media 5 hours before mitosis. The duration of this pulse is indicated by the gray rectangle in each plot. Cells are color-coded based on their CDK2 activity 15 frames after anaphase. Each plot contains 100 single cell traces. (D) Plot of fraction of proliferating daughter cells as a function of mother cell age at treatment addition. Dashed line indicates mitosis. Light colored bands represent 95% confidence intervals. (E) Plot of fraction of $CDK2^{emerge}$ daughter cells as a function of mother cell age at treatment addition. Dashed line indicates mitosis. Light colored bands represent 95% confidence intervals. (F) Plot of fraction of $CDK2^{low}$ daughter cells as a function of mother cell age at treatment addition. Dashed line indicates mitosis. Light colored bands represent 95% confidence intervals. n=2 biological replicates. Each time point contains the average and 95% CI of at least 20 individual cell traces.

in each mitosis “slice” can be identified and expressed as a fraction. This is repeated for all frames of the time lapse to yield a map of when TPA acts to influence cell fate after division (Figure 3.9B).

We used the FUCCI (CA) sensor to identify the boundaries between the phases relative to mitosis (Figure 3.10). To illustrate this process, we selected cells that divided five hours after TPA addition from each treatment group and identified the distribution of cell fates after division. As shown previously (71, 80, 215), we found that 80% of untreated MCF10a cells increase their CDK2 activity immediately after mitosis, indicating that they are born committed to the cell cycle (Figure 3.9C). The other 20% enter a brief resting state, deemed CDK2^{emerge}. Pulses of varying lengths of Zn^{2+} deficient media five hours before cell division leads to progressive loss of the CDK2^{inc} population (blue), and a concomitant increase in the proportion of CDK2^{emerge} cells (Figure 3.9C). Finally, if Zn^{2+} deficient media was added during S-phase and kept until the end of the time lapse, cells bifurcate into two populations, where the majority either enter the CDK2^{emerge} or CDK2^{low} cell fate (Figure 3.9C). This agrees with previous research (13).

After repeating this analysis for all frames of the time lapse, we found that 80% of MCF10a cells are born proliferative, regardless of when minimal media was resupplied, which agrees with prior research (71, 80, 215). In contrast, cells that are pulsed with the Zn^{2+} chelator TPA during S-phase (five hours before mitosis) for two or four hours show a decrease in proliferative daughter cells (Figure 3.9C). This decrease is accompanied by a proportional increase in the fraction of CDK2^{emerge} daughter cells, indicating that if cells lack Zn^{2+} in S-phase, they enter a transient state of low CDK2 activity after cell division (Figure 3.9E). Critically, these cells do not enter a permanent CDK2^{low} state after division, indicating that they are not quiescent to the end of the time lapse, but are instead in a transient state of cell cycle exit (Figure 3.9F). Importantly, beginning the pulse of Zn^{2+} deficiency after the S/G2 boundary or before mid S-phase has no effect on the proliferation of daughter cells. In contrast, the cells that are treated with TPA until the end of the time lapse show a strong propensity to be either CDK2^{emerge} or CDK2^{low} after

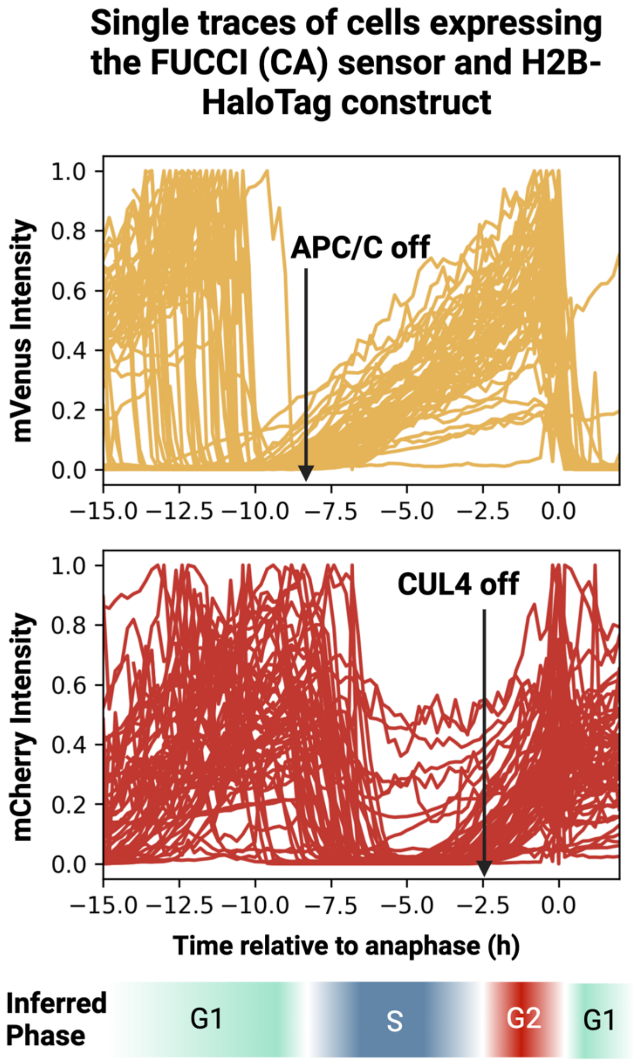

Figure 3.10: The FUCCI (CA) sensor can identify cell cycle phase transitions at a population level. (Top) Single-cell traces of the mVenus component of the FUCCI (CA) sensor aligned to mitosis. The black arrow indicates the time at which the population of cells enters S-phase, as evidenced by the buildup of the mVenus signal. (Middle) Single-cell traces of the mCherry component of the FUCCI (CA) sensor aligned to mitosis. The black arrow indicates the time at which the population of cells enters G2, as evidenced by the buildup of the mCherry signal. (Bottom) The inferred phase of the cell cycle as a function of time relative to mitosis.

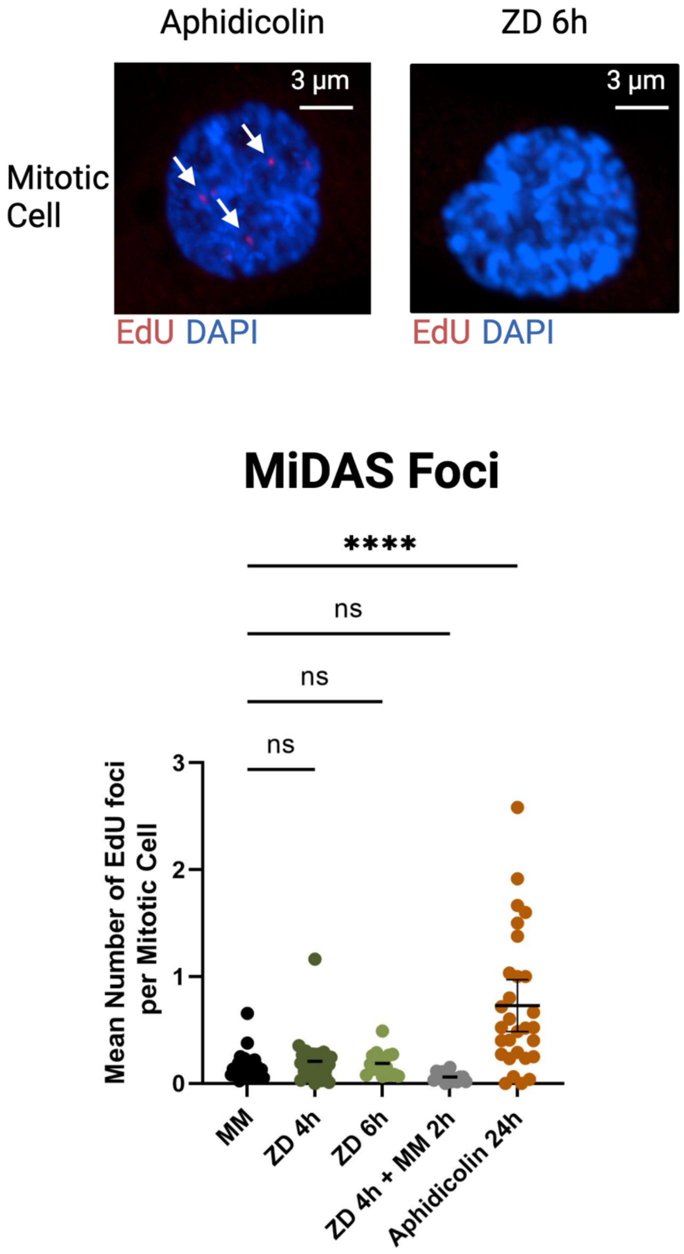

Figure 3.11: Neither Zn^{2+} deficiency nor Zn^{2+} resupply stimulates mitotic DNA synthesis (MiDAS). (Top) Representative images of mitotic cells treated with either 0.2 μM aphidicolin for 24h or Zn^{2+} deficiency for 6 hours. Note the red EdU foci in the aphidicolin treatment (white arrows) and absence thereof in the Zn^{2+} deficient treatment. (Bottom) Quantification of MiDAS foci. Each dot represents average MiDAS foci in one well of a 96-well plate. Error bars represent the 95% confidence interval. **** = $p < 0.001$, n ≥ 2 biological replicates.

division, as shown previously (Fig 3.9E-F) (13). The distribution of fates shifts toward the CDK2^{low} population the longer a cell is in Zn^{2+} deficient media (Figure 3.9E-F). Of note, the transmission of replication stress through mitosis is not accompanied by mitotic DNA synthesis (MiDAS) (Figure 3.11), which marks the transmission of unresolved replication stress to daughter cell quiescence (231, 232). These data demonstrate that cells pulsed with TPA during S-phase enter a transient CDK2^{emerge} state after division, implying that the replication stress and DNA synthesis inhibition due to low Zn^{2+} conditions are directly impacting daughter cell proliferation.

3.4.6 Sustained p21 expression maintains cell cycle pause induced by Zn^{2+} deficiency

Transient Zn^{2+} deficiency in the mother cell S-phase causes a proliferative pause in the daughter cells (Figure 3.9). The tumor suppressor p21, among other such proteins, acts as a competitive inhibitor of the active Cyclin E-CDK2 complex (212), and thus is one factor that can prevent cells from entering the cell cycle. p21 acts to maintain the quiescent state in both unperturbed cells and cells who inherit damaged DNA from mother cells (71, 96, 218). If Zn^{2+} is depleted in G1 of the mother cell (approximately 12 hours before mitosis), daughter cell proliferation is not significantly different from the daughters of Zn^{2+} adequate cells (Figure 3.12A). If Zn^{2+} is depleted in S-phase approximately 6 hours before mitosis, and not resupplied prior to the end of S-phase (at approximately 2 hours prior to mitosis), the fraction of daughters born proliferative is reduced to approximately 45% (Figure 3.12A). We therefore hypothesized that transient Zn^{2+} deficiency in S-phase would induce a sustained p21 expression after division when compared to the untreated cells. We similarly hypothesized that transient Zn^{2+} deficiency during G1 would induce p21 expression dynamics similar to the untreated cells, since we do not see impaired proliferation. To test this, we used a cell line expressing the CDK2 activity sensor, H2B-mTurquoise2 as a nuclear marker, and a p21-mCitrine construct expressed at the endogenous

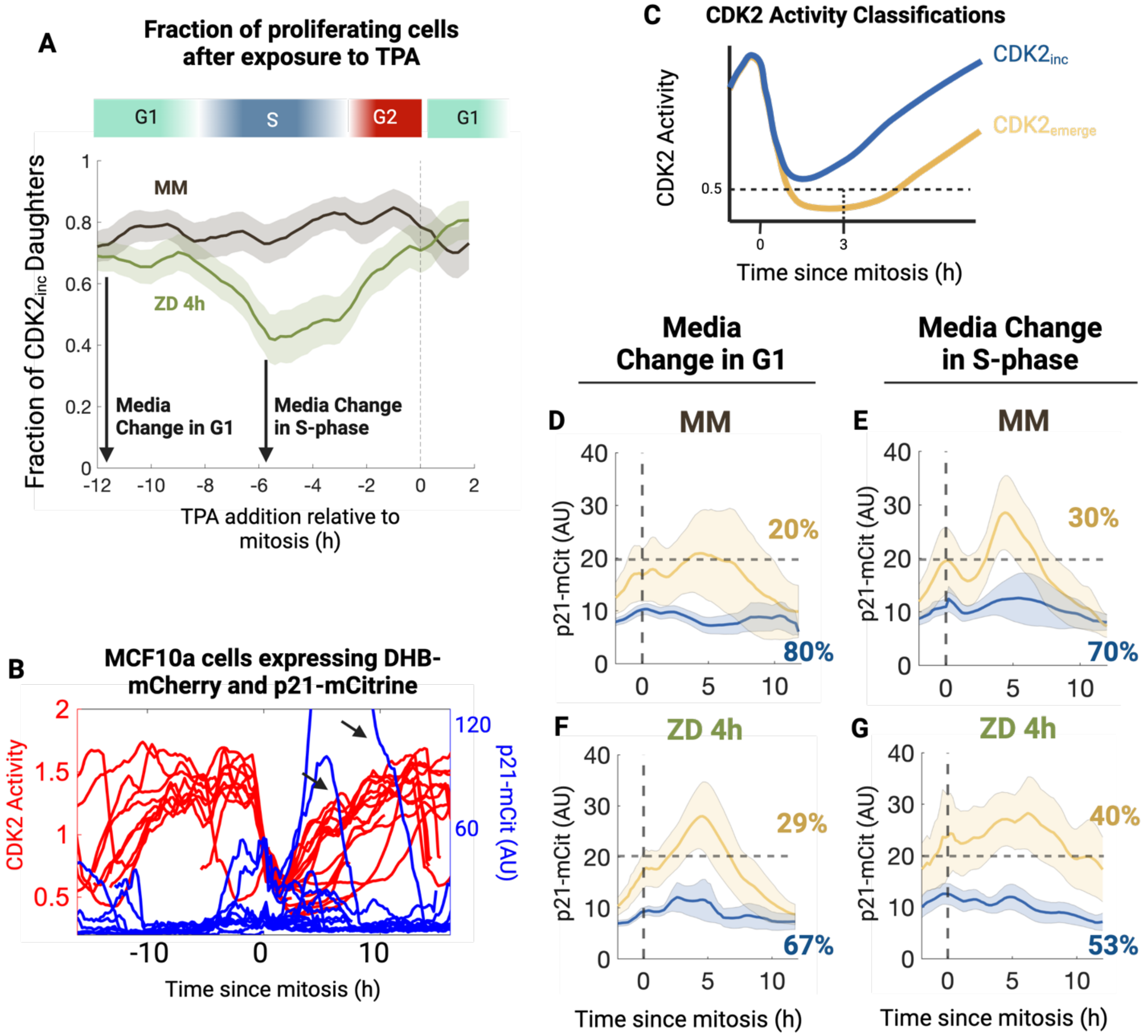

Figure 3.12: Transient Zn^{2+} deficiency during S-phase induces proliferation impairment accompanied by sustained p21 expression in G0. (A) Results from Figure 3.12D. Arrows indicate times relative to anaphase that induces normal daughter cell proliferation and impaired daughter cell proliferation, respectively. (B) Representative traces of cells expressing DHB-mCherry (red) and p21-mCitrine (blue) from the endogenous locus aligned to anaphase. n=10 single-cell traces. Eight traces are born with low p21 expression. Two traces (black arrows) show transiently increased p21 expression. (C) CDK2 activity classification scheme. Yellow traces indicate $CDK2^{emerge}$ population, blue traces indicate $CDK2^{inc}$ population. (D, F) Average p21 expression in cells that divided twelve hours after treatment with either Zn^{2+} deficient media or control media, color coded to show the $CDK2^{inc}$ (blue) and $CDK2^{emerge}$ (yellow) populations. Light bands indicate 95% confidence intervals. n = 2 biological replicates. (E, G) Average p21 expression in cells that divided six hours after treatment with either Zn^{2+} deficient media or control media, color coded to show the $CDK2^{inc}$ (blue) and $CDK2^{emerge}$ (yellow) populations. Light bands indicate 95% confidence intervals. n = 2 biological replicates.

locus (Figure 3.12B) (71). We treated these cells with Zn^{2+} deficient media for four hours, followed by a resupply of Zn^{2+} adequate media. We then analyzed cells that divided 12 and six hours after transient Zn^{2+} deficiency for changes in p21 dynamics in both $CDK2^{inc}$ and $CDK2^{emerge}$ populations.

Eighty percent of untreated cells are born as $CDK2^{inc}$ with low p21 expression (blue-colored traces) (Figure 3.12B,D,E), which also agrees with previously published work (71, 78). The other 20% of cells are born as $CDK2^{emerge}$ and show a transient increase in p21 that falls to basal expression after seven hours, followed by an increase in CDK2 activity and commitment to another cell cycle (Figure 3.12B,D). This also agrees with previously published results showing that in asynchronously cycling cells, a small population of cells accumulates DNA damage and pauses the cell cycle via expression of p21 (71). Similar to the untreated condition, when Zn^{2+} was depleted and resupplied in G1 (12 hours prior to anaphase), the $CDK2^{emerge}$ population shows comparable p21 dynamics to $CDK2^{emerge}$ cells in the untreated condition (Figure 3.12F). Although there are fewer proliferative cells in this population (Figure 3.12F), the p21 signal rises and returns to baseline with dynamics similar to the untreated cells. Therefore, a pulse of Zn^{2+} deficiency in G1 shows similar p21 dynamics to untreated cells. When Zn^{2+} is depleted and resupplied during S-phase, however, the fraction of cells born $CDK2^{emerge}$ increases to approximately 40%, which agrees with the data in Figure 3.9D. Further, this population shows sustained p21 expression that does not drop to basal levels for at least twelve hours after division (Figure 3.12E,G), indicating that the $CDK2^{emerge}$ state is being maintained by sustained p21 expression. This result indicates that Zn^{2+} deficiency induced replication stress during S-phase of the mother cell is inherited by daughter cells to cause temporary quiescence.

3.5 Discussion

Duplicating a genome is a daunting task, and requires careful monitoring of cell state (81). Human cells constantly sample their intra- and extracellular environment for growth factors, genotoxic stress, and metabolites and integrate these signals to determine whether to repair, grow, or die (80, 96, 219). Early work to identify the role of Zn^{2+} deficiency in the mammalian cell cycle revealed a loosely-related set of phenotypes ranging from DNA synthesis impairment (100) to oxidative stress (109, 112) to apoptosis (154, 207). None of these studies simulated mild, physiologically relevant Zn^{2+} deficiency, and instead relied on high concentrations of metal chelators and cell synchronization, which are known to disrupt cell cycle progression via stress responses (100, 102–105). Due to zinc's role in a multitude of cellular processes, it is often assumed that Zn^{2+} deficiency will induce pleiotropic effects on cells. To dissect whether Zn^{2+} acts during a specific cell cycle phase to impair proliferation, we used pulse-chase treatments along with fluorescent cell cycle reporters. We found that transient Zn^{2+} deficiency impaired S-phase progression, slowed DNA synthesis rates, and induced replication stress signaling, which contributed to a pause in the cell cycle of daughter cells. Importantly, transient Zn^{2+} deficiency during other phases of the cell cycle had no adverse effects. These results demonstrate a specific requirement for Zn^{2+} during S-phase, in contrast to the assumption that Zn^{2+} deficiency affects cellular processes pleiotropically.

Replication stress can be caused by DNA lesions and adducts (229), imbalanced nucleotides (219, 224), under-licensed replication origins (81, 105), inhibition of DNA polymerase (233), or endogenous stochastic uncoupling of replication forks (215). The results of many previous studies into Zn^{2+} and in the mammalian cell cycle revealed phenotypes that could be classified as "replication stress," including impaired DNA synthesis, increased DNA damage signaling and production of oxidative products (100, 102, 109). In this study, we found that when cells were treated with a short pulse of Zn^{2+} deficiency, there was no evidence of under licensing, nucleotide imbalance, or double-stranded breaks. Instead, we found that acute Zn^{2+} deficiency increases RPA2 recruitment to nuclear foci and activates the checkpoint kinase Chk1. RPA2 recruitment and Chk1 activation are both hallmarks of functionally uncoupled polymerase-helicase complexes (92, 228, 229), indicating that the helicase is still fully functional under conditions of Zn^{2+} deficiency.

The DNA polymerases Polα, Polδ, and Polε are protein complexes in the eukaryotic replisome responsible for synthesizing the genome, and the catalytic subunits of these complexes have at least one Zn^{2+} binding motif that appear to be critical for their function (234). For example, the zinc finger domain of the *S. cerevisiae* Polε is important for transducing DNA damage signaling through the S/M checkpoint pathway, and seems to impair signaling when mutated (235). Further, the C-terminal zinc finger of the *S. cerevisiae* Polδ is required for its association between other subunits of the Polδ complex, and mutation of the zinc finger abolishes activity *in vivo* (236). Finally, human Polα contains a C-terminal zinc finger, and treatment with cisplatin displaces the Zn^{2+} ion and inhibits its activity *in vitro* (237). In addition to the role of zinc fingers within the Pol subunits, there is evidence that suggests Zn^{2+} plays a role in stabilizing intermolecular interactions formed between proteins in these complexes (238). A handful of studies have even identified that depletion of Zn^{2+} from the *E. coli* DNA polymerase I impairs its activity (119, 239); however, studying the role of these zinc finger domains in mammalian cells is prohibitively difficult. Since the subunits of the DNA polymerase complex are essential, and knockout or mutation of these genes in human cells is lethal, it is not possible to mutate these Zn^{2+} fingers in mammalian cells. That said, the evidence presented here rules out other causes of replication stress, and suggests that DNA polymerase activity is sensitive to changes in the labile Zn^{2+} pool.

Replication stress in mother cells can be inherited by daughter cells to cause a pause in proliferation, accompanied by expression of p21 (96, 215, 218). Since impaired DNA synthesis, RPA2 foci accumulation, and Chk1 phosphorylation all decrease upon resupply of Zn^{2+}, we sought to determine whether the memory of this DNA damage signaling influences the daughter cell's proliferative fate. Cells exposed to a short pulse of TPA during the latter half of S-phase show an increase in cells entering a temporary CDK2 low state after cell division. These cells are able to re-enter the cell cycle after a pause in proliferation, indicating that the inherited damage is reversible, and very few cells enter a permanent state of quiescence. This pause is accompanied by sustained expression of the tumor suppressor p21, which agrees with previous reports of inherited cell fate due to replication stress in the mother cell (96, 215, 218).

Using long-term live-cell imaging, fluorescent tools, and single-cell analyses, we identified a specific requirement for Zn^{2+} in S-phase. If cells are deficient in this essential micronutrient while synthesizing DNA, they show hallmarks of replication stress and DNA synthesis impairment. Further, this Zn^{2+} deficiency-induced replication stress impairs proliferation in daughter cells, maintained by sustained p21 expression. Together, these data demonstrate that mild and temporary Zn^{2+} deficiency can impair DNA synthesis within two hours, and induce replication stress that is passed onto daughter cells after division.

3.6 Materials and Methods

Table 4: Materials table

Agent or Resource	**Source**	**Identifier**
Antibodies		
Anti-RPA32/RPA2 antibody [9H8]	Abcam	ab2175
Phospho Histone H3 (Ser10) (6G3) Mouse mAb	Cell Signaling Technology	9706L
Anti-phospho Histone H2A.X Ser139 mouse monoclonal antibody	Cell Signaling Technology	80312S
Anti-phospho Chk1 Ser317 rabbit	Abcam	ab226929
Anti-phospho Chk2 Thr68 rabbit	Thermo Scientific	PA5-17818
Purified mouse anti-human 53BP1	BD Biosciences	612523
Mouse anti-MCM2 monoclonal antibody	BD Biosciences	610700

Goat anti-rabbit (H+L) Alexa Fluor 647	Fisher Scientific	A21245
Goat anti-mouse (H+L) Alexa Fluor 647	Fisher Scientific	A21236
Chemicals, peptides, and recombinant proteins		
Tris(2-pyridylmethyl) amine 98% (TPA)	Sigma-Aldrich	723134
Chelex-100, sodium form	Sigma-Aldrich	C7901
Janelia Fluor 669 Halo-Tag dye (JF669)	Laboratory of Luke Lavis, Janelia Research Campus	N/A
DMEM/F12, HEPES	Thermo Fisher Scientific	11330057
Horse Serum, New Zealand origin	Thermo Scientific	16050122
Hydrocortisone	Sigma-Aldrich	H4001
Insulin	Life Technologies	12585-014
FluoroBrite DMEM	Fisher	A18967-01
Gibco EGF Recombinant Human Protein	Thermo Fisher Scientific	PHG0313
Ham’s F12 phenol red-free	Sigma-Aldrich	N6658

Cholera Toxin	Sigma-Aldrich	C8052
Pen/Strep	Gibco	15140-122
0.05% Trypsin-EDTA(1X)	Gibco	25300-120
Hoechst 33258	Sigma-Aldrich	861405
FAM azide, 6-isomer	Lumiprobe	B5130
5-Ethynyl-2'-deoxyuridine,95%	Sigma-Aldrich	900584-50MG
Alexa Fluor 647 azide	Lumiprobe	A6830
L-Ascorbic acid	Fisher Scientific	A61-25
Aphidicolin from Nigrospora sphaerica,>=98% (HPLC), powder	Sigma-Aldrich	A0781-1MG
Bleomycin, ready made solution	Sigma-Aldrich	B7216
4-Nitroquinoline N-oxide,≥98%	Sigma-Aldrich	N8141-250MG
CHIR-124 2mg	Selleck Chemicals	S2683
Critical Commercial Reagents		
TransIT-LT1	Mirus Bio	MIR 2300
Experimental models: cell lines		

Human: MCF10a	ATCC	CRL-10317
Human: MCF10a + H2B-HaloTag	Rakshit and Holtzen 2023 (10)	PMID: 37330912
Human: MCF10a + H2B-HaloTag + FUCCI (CA)	This work	N/A
Human: MCF10a + H2B-mTq2 + DHB-mVenus	Lo 2020 (13)	PMID: 32014109
Human: MCF10a + H2B-mTq2 + DHB-mCherry + p21-mCitrine	Moser 2018 (71)	PMID: 30111539
Recombinant DNA		
Plasmid: PB-H2B-HaloTag (used for stable cell line generation)	Grimm 2017 (240)	PMID: 28869757
mVenus-hGeminin(1/110)/pCSII-EF	Riken	RDB15271
mCherry-hCdt1(1/100)/pCSII-EF	Riken	RDB15442
Software and Algorithms		

BD FACSDiva Version 8	BD Biosciences	N/A
MATLAB 2017a and VR2020b	Mathworks	N/A
Prism Version 9.2.0	GraphPad	N/A
EllipTrack	Tian 2020 (182)	PMID: 32755578

Cell culture

MCF10a cells were procured from ATCC and maintained in full growth media (FGM). FGM is composed of DMEM/F12 media supplemented with 5% horse serum, 1% penicillin/streptomycin solution, 20 ng/mL EGF, 0.5 µg/mL hydrocortisone, 100 ng/mL choleratoxin, and 10 µg/mL of insulin. Cells were passaged at 80-90% confluency using 0.05% trypsin-EDTA to subconfluency. To remove excess Zn^{2+} from horse serum and insulin, we incubated serum and insulin solutions with Chelex-100 resin for 12 hours at 4ºC, followed by sterile filtration to remove resin. Our Zn^{2+} defined minimal media (MM) consists of 1:1 Ham's F12 nutrient mix:FluoroBrite DMEM, supplemented with 1.5% Chelex-100 treated horse serum, 10µg/mL Chelex-100 treated insulin, 1% penicillin/streptomycin solution, 20 ng/mL EGF, 0.5 µg/mL hydrocortisone, and 100 ng/mL cholera toxin. We previously quantified metal content of MM containing Chelex-100 treated serum, which showed that Chelex-treatment leads to a reduction in zinc (from 2.18 to 1.46 µM) and nickel (from 0.178 to 0.012 µM), but no significant changes in other metals. Unless otherwise stated, ZD media was generated by adding 3 µM TPA to MM. For imaging experiments, cells were grown and imaged in MM, with perturbations with ZD media at 37ºC and 5% CO_2. Cells used in experiments were less than passage number 15, and were routinely tested and confirmed to be mycoplasma negative by PCR.

Plasmids and cell lines

MCF10a cells expressing PB-H2B-HaloTag (240) and the FUCCI (CA) system were generated using lentiviral transduction. Briefly, HEK293T cells were transiently transfected with both the hGem-mVenus and hCdt1-mCherry plasmids, along with Lenti-X lentiviral packaging plasmids psPax2, PdM2.G in OptiMEM using the TransIT-LT1 transfection reagent (Mirus Bio). This was followed by viral amplification in HEK293T cells Successful transfection was verified via visualization of mCherry and mVenus fluorescence in the HEK293T cells. Viral particles were harvested 24 hours after transfection, filtered through 0.45 µm syringe polyethersulfone (PES) filters and then 1 mL was added to MCF10a cells stably expressing H2B-HaloTag and allowed to incubate for 48 hours along with 4 µg/mL polybrene. Stable cell lines used for imaging were then FACS sorted on a BD FACSAria Fusion for high mCherry and mVenus fluorescence relative to an non-transduced control using the following optics: YFP: Ex 488 nm, Em 530/30 nm; and mCherry Ex 561 nm, Em 610/20 nm.

Live-cell imaging

MCF10a cells expressing fluorescent reporters were counted using the Countess II Automated Cell Counter (Thermo Fisher Scientific) and plated in MM into glass bottom 96-well plates (Cellvis P96-1.5H-N) at a density as to ensure cells were subconfluent by the end of the time lapse. After plating, cells were left undisturbed in the biosafety cabinet for 30 minutes to properly adhere to the dish, then moved to the incubator to recover for at least 16 hours. Immediately before imaging, cells expressing H2B-HaloTag were stained with 5 nM JF669 dye (Luke Lavis, Janelia Research Campus) for 30 minutes, then washed once with prewarmed MM.

For the ZD pulse-chase experiment, acquisition was paused, half of the media was removed, and replaced with a 2X solution of prewarmed ZD media. To wash out the treatment, 90% of the media was removed from the well and replaced with prewarmed MM. For the “To End” condition, treatment media was not removed.

Time-lapse images were collected using a Nikon Ti-E High Content Analysis inverted microscope with a Lumencor SPECTRA X light engine (Lumencor) and Hamamatsu Orca FLASH-4.0 V2 scMOS camera (Hamamatsu). Images were collected every 12 minutes with a 10X 0.45 NA Plan Apo air objective lens (Nikon Instruments). During imaging, cells were kept in a controlled environmental chamber surrounding the microscope (Okolab Cage Incubator, Okolab) at 37ºC and 5% CO_2 and 90% humidity. Filter sets for live-cell imaging were as follows: CFP Ex: 440, 455 dichroic, Em: 480/20, power 50; YFP Ex: 508, 518 dichroic, Em: 540/21; mCherry Ex: 555, 597 dichroic, Em: 595/40; and JF669/Cy5 Ex: 640, 640 dichroic, Em: 705/22, power 50. Exposure times were adjusted to eliminate pixel saturation and to minimize exposure time, while still maintaining an adequate signal to noise ratio.

Time-lapse image processing

Live-cell imaging experiments were analyzed using the EllipTrack cell tracking pipeline in MATLAB 2017a and 2020b on the institutional computing cluster (182). Briefly, EllipTrack requires several generalized parameters for cell segmentation, tracking and event identification. The advanced parameters were unchanged from the original code accessible on Github, as recommended by the authors. Basic parameters were fine-tuned by hand using the built-in user interface. Separate training data sets for the EllipTrack event predictions were made using at least 500 events across each time series for both H2B-HaloTag and H2B-mTurquoise2 nuclear markers. We used a nuclear radius of 12 pixels as the average size of one cell. The ellipse that is fitted to this nucleus was required to be at least 25 pixels in area. Nuclear images were log transformed and a blob detection algorithm was used to identify nuclei with a blob threshold of -0.075. Objects were separated using a watershed algorithm and ellipses were fitted to each object. Mitoses were inferred based on morphological properties of each object before and after a potential mitosis event. Migration and migration speed were inferred using a density-dependent migration speed from the training data. All tracks greater than 10 frames were kept, and tracks were allowed to skip at most two frames. Tracking was spot-checked by eye using the visualize tracking (vistrack) movies generated by the script to ensure adequate tracking and minimize track loss or swapping. Mean intensity from nuclear localized reporters was extracted using the nuclear mask. The mean intensity of cytoplasmic sensors was calculated in a three-pixel wide cytosolic ring around the nuclear mask.

Flow Cytometry EdU Incorporation Assay

Cells were plated at sub-confluency in 6-well plates in MM and allowed to recover for at least 16 hours. Cells were treated with ZD media for 2-4 hours, co-treated with ZD media and 250 or 500 nM CHIR-124, or left untreated. Thirty minutes before harvesting, cells were pulse-labeled with 10 µM EdU for 30 minutes in the cell culture incubator. Cells were then harvested using 0.005% EDTA/Trypsin and pelleted at 300 x g for 5 minutes. Cells were fixed using 4% paraformaldehyde (PFA) and washed twice with phosphate buffered saline (PBS) + 1% bovine serum albumin (BSA) (B-PBS). Cells were permeabilized with 0.2% Triton-X100 for 15 minutes, then washed twice with B-PBS. Cells were then resuspended in a click solution consisting of 50µM FAM-Azide, 2 mM $CuSO_4$, and 50 mM L-ascorbic acid in PBS for 30 minutes in the dark. Cells were washed with B-PBS and stained with an analysis buffer (B-PBS with 1:10000 dilution of 1 mg/mL DAPI) for 1h. Cells were analyzed on a BD FACSCelesta outfitted with 405 and 488 nm optics. FACS files were exported and analysis was done in FlowJo or at floreada.io, a free open-source flow cytometry analysis tool. S-phase was identified by gating EdU+ cells. The median EdU signal was extracted from this population in all treatment conditions. These signals were then normalized to the median EdU signal of the untreated control.

Loaded MCM2 Assay

Fixed cell immunostaining of loaded MCM2 and flow cytometric analyses were performed as previously described (105). Briefly, following treatments or release from serum starvation, cell suspensions were fixed with 4% PFA and washed twice before stepwise staining: EdU click reaction with FAM-Azide (room temperature for 30 minutes), mouse anti-MCM2 immunostaining (BD Biosciences #610700, 1:200 dilution in PBS with 1% BSA for 1 hour at 37ºC), goat anti-mouse Alexa Fluor 594 immunostaining (Thermo Fisher A-11005 for 1h at 37ºC), and Hoechst 33342 (1:10,000 in PBS overnight at 4ºC). Cell suspensions were filtered for single cells and analyzed using a BD FACSCelesta flow cytometer outfitted with 405, 488, and 561 nm lasers. FACS files were exported and analyzed using FlowJo or at floreada.io, a free open-source flow cytometry analysis tool.

Cells were first gated for cells on forward scatter area vs. side scatter area, then gated on DAPI signal height vs. DAPI signal area for single cells. MCM2+ S-phase cells were then identified using plots of EdU incorporation vs loaded MCM2 in the untreated control. These gates were then applied to all other cells to identify the fraction of cells that entered early G1 with under-licensed origins of replication.

Detection of mitotic DNA synthesis (MiDAS)

MCF10a cells were plated in 96-well plates at a density of 10,000 cells per well into MM. Plates were left in the biosafety cabinet for 30 minutes to allow cells to adhere to the dish, then transferred to the incubator.. After 4 hours, positive control cells were treated with 0.2 µM aphidicolin for 24 hours. Cells were treated with 3 µM TPA for 4 or 6 hours. For the resupply experiment, ZD media was removed from cells and replaced with fresh MM. Media was then removed from all cells and replaced with media containing 40 µM EdU, and allowed to incubate for 30 minutes. Cells were washed with PBS and fixed with 4% PFA in PBS for 10 minutes, then permeabilized with PBS containing 0.1% Triton-X100 for 10 minutes. Cells were washed and incubated with a click chemistry buffer containing Alexa Fluor 647 azide as described previously. Cells were then blocked using PBS containing 3% BSA for 1h before staining with mouse anti-phospho histone H3 (Ser10) (1:400 dilution into PBS + 1% BSA, Cell Signaling Technologies) overnight at 4ºC. Cells were then washed and counterstained with a goat anti-mouse secondary antibody conjugated to Alexa Fluor 488 (1:1000 into PBS + 1% BSA, Thermo Fisher) and DAPI. Cells were washed and then immediately imaged as described below.

Immunofluorescence and Fixed Cell Imaging

MCF10a cells expressing H2B-HaloTag and the FUCCI (CA) system were plated in 96-well plates (for Chk1 IF and yH2AX IF, cells were plated in Cellvis P96-1.5H-N plates, for RPA2 IF, cells were plated in PerkinElmer PhenoPlate 96) at a density of 10,000 cells per well. Plates were left in the biosafety cabinet for 30 minutes to allow for proper adhering, then allowed to recover in the incubator for at least 16 hours undisturbed. Prior to fixation, cells were treated for either 2h or 4h with ZD media, or 4 hours with 2 µg/mL aphidicolin. For EdU incorporation at short timepoints, cells were pulsed with 10 µM EdU 30 minutes before fixation. At the time of fixation, cells were washed twice with PBS pH 7.4, then fixed with 4% PFA in PBS pH 7.4 for 15 minutes. Cells were then washed twice with PBS, then permeabilized with 0.05% Triton-X100 in PBS for 20 minutes. Cells were then washed twice with PBS and blocked for 1 hour with PBS and 3% bovine serum albumin (BSA). Afterwards, the BSA solution was removed and the primary antibody solution (1:250 for all targets in 3% PBS) was added without washing. This was allowed to incubate overnight for at least 16 hours at 4ºC. Cells were washed 4X with PBS pH 7.4, then stained with secondary antibody (1:1000 into PBS + 1% BSA goat anti-mouse (H+L) Alexa Fluor 647 for RPA2 and yH2AX, and 1:1000 goat anti-rabbit (H+L) Alexa Fluor 647 for Chk1 pSer317) in PBS with 3% BSA and 100 ng/mL Hoechst dye for 1h at room temperature. Cells labeled with EdU alone were stained using click chemistry to attach an Alexa Fluor 647 azide dye to the ethynyl handle of EdU as described previously. Cells were immediately imaged.

Images of pChk1, yH2AX, and EdU were collected using a Nikon Ti-E High Content Analysis inverted microscope with a Lumencor SPECTRA X light engine (Lumencor) and Hamamatsu Orca FLASH-4.0 V2 scMOS camera (Hamamatsu) using a 40X 0.65 NA CFI Plan air objective from Nikon. A 9x9 large image was taken of the center of each well of the 96-well plate. The DAPI channel was acquired using a 395/15 excitation / 475/24 emission. The YFP channel was acquired using a 510/25 excitation 540/21 emission filter set. The mCherry channel was acquired using a 575/25 excitation 632/60 emission filter set. The Cy5 channel was acquired using a 640/30 excitation 705/72 emission filter set. Single-cell quantitation was done by identifying nuclei using a custom MATLAB pipeline. Since these targets are localized to the nucleus, we then extracted mean intensity in the DAPI, YFP, mCherry, and Cy5 channels in the region of the identified nuclear masks.

Images of RPA2 were collected on a PerkinElmer Opera Phenix high-content screening system with a 20x/1.0 NA water objective. Eight images of each well were collected, each containing three Z-stack images of all channels. Maximal intensity projections were calculated, and used in subsequent analysis of all channels. Single-cell quantitation was done by identifying nuclei using a custom MATLAB pipeline, then extracting mean intensity in the DAPI, YFP, and mCherry channels in those regions. Additionally, single RPA2 foci were found by adaptive thresholding of each nuclear object on the Cy5 channel, with area filtering of objects greater than 5 pixels and with an eccentricity of less than 0.8.

Images of MiDAS were collected on a PerkinElmer Opera Phenix high-content screening system using the PreciScan modality. Briefly, cells were imaged at a low magnification (10X/0.4 NA air objective), then cells were identified and selected for high phospho-histone H3 (Ser10) fluorescence. These cell locations were recorded and the objective was switched to a higher magnification (40X/1.1 NA water objective) and imaged. Six Z planes were acquired for each cell, and at least 20 regions were imaged per well, yielding at least 150 cells per condition. Image processing and MiDAS foci selection was done using the PerkinElmer Harmony software.

Relative metabolite quantification

Relative metabolite quantification was performed by the University of Colorado School of Medicine Metabolomics Core (Aurora, CO). Metabolite extraction was accomplished by the addition of 4°C lysis buffer (LB) (5:3:2 methanol:acetonitrile:water (v/v/v)) to a concentration of 2 x 10^6 cells/mL (based on approximate cell counts) to frozen cell pellets. This mixture was vortexed for 30 min at 4°C and centrifuged for 10 min (18,000g, 4°C) to re-pellet the cells. The supernatant was then removed and placed in autosampler vials for UHPLC-MS analysis. A Thermo Vanquish UHPLC system combined with a Thermo Orbitrap Exploris 120 mass spectrometer (Thermo Fisher Scientific, Waltham, MA, USA) was used for untargeted metabolite analysis. Samples were analyzed both in positive and negative ion mode in separate runs using a 5 min gradient method (241).

El-Maven v0.12.0 was used to identify, quantitate (by peak area) and annotate mass spectra features to produce a global metabolomic analysis (242). Statistical analysis (PLS-DA, Heatmap) and pairwise comparisons were accomplished using MetaboAnalyst 5.0 (243).

Data analysis

Analysis of the DHB-mVenus pulse-chase experiment:

Single cell tracks were extracted from the EllipTrack output, and each mother and daughter cell was joined by at least one mitosis event to get combined mother/daughter cell tracks. To remove non-expressing cells and tracks that were swapped during analysis, two filters were employed: in the first, cells were removed that had an intensity value below a cutoff chosen for each replicate of the experiment. Second, cells that were swapped during tracking have at least one very short intermitotic time (IMT), indicating that the track was attributed a mitosis when there was not one, or the track was swapped with a cell that was mitotic. An IMT cutoff of 50 frames was used, since MCF10a cells have a cell cycle of 60 frames or longer. A sampling of tracks were analyzed by eye to ensure the analyzed tracks behaved as expected, and that poorly tracked cells were kept to a minimum.

CDK2 activity was calculated at every frame by dividing the mean cytoplasmic signal of the DHB-mVenus reporter by the mean nuclear signal. This will typically yield a CDK2 activity ranging between 0.2 and 2 AU. To identify the cell cycle dependence of Zn^{2+} in cells, tracks were binned based on the frame at which they divided. For each frame, we calculated the cell fate of cells dividing in a 5 frame window around that frame in the following manner: if cells had a CDK2 activity > 0.5 by 15 frames after mitosis, they were called "$CDK2^{inc}$". If cells had a CDK2 activity < 0.5 15 frames after mitosis, they were either $CDK2^{emerge}$ or $CDK2^{low}$. To delineate, we determined whether cells began building up CDK2 activity after division, or if they stayed low for the rest of the time lapse. The average and 95% confidence interval were determined for each frame. The data were then plotted as "drug addition relative to anaphase". Since proliferating cells have an IMT of between 60-70 frames, or 12-14 hours, the time point -12 is taken to be either mid or late G1. After cells commit to a cell cycle, the time from S-phase to mitosis is very robustly 8 hours. All analysis was conducted in MATLAB 2020B.

Analysis of the DHB-mCherry p21-mCitrine pulse-chase experiment:

Single-cell tracks were constructed identically to the DHB-mVenus pulse-chase experiment. Mean nuclear fluorescence of the p21-mCitrine signal was used to determine p21 protein expression at each frame of the time-lapse. For each treatment condition, cells were binned according to their CDK2 activity after division similarly to the DHB-mVenus pulse-chase experiment. Since cells were expressing DHB-mCherry, the threshold for CDK2^{inc} and CDK2^{emerge} cells was 0.58 instead of 0.5, which we identified empirically. The CDK2 activity and p21 signal was then averaged and 95% confidence intervals were calculated.

Analysis of the FUCCI (CA) pulse-chase experiment:

Tracks of cells expressing the FUCCI (CA) sensor had to exist for the entirety of the timelapse and were joined by every mitosis event detected by the EllipTrack program. Cells not expressing both FPs at some point in the time lapse were removed from analysis. To identify mitosis events, the local minima were found in the derivative of the mVenus signal. To identify cell cycle phases, the mVenus and mCherry signals were min-max normalized, and subjected to hysteresis thresholding to find roughly where each sensor was on or off. These thresholded FUCCI (CA) signals were then passed through a first-round phase calling algorithm, which simply assigned the G1 phase to mCherry(+) cells, S-phase to mVenus(+) cells, and G2 to mCherry(+) and mVenus(+) cells. Occasionally, this algorithm miscalled the G1/S transition as G2, so a refining function was applied to ensure that cells progressed from G1 to S to G2 to M to G1 and so on in that exact order. Cell cycle phase lengths were measured for each mother and daughter cell and exported for analysis. All analysis was done in MATLAB 2020B and in Python.

Identifying FUCCI cell cycle phase using a Gaussian Mixture Model (GMM)

Mean nuclear intensities of the FUCCI reporter were extracted from fixed cells in every IF experiment. The z-score of each intensity was calculated for each replicate, and then each cell was categorized using a GMM with a set random seed and 10,000 iterations, which ensured that the model converged. Cells were then plotted and color-coded with their respective predicted group, and cell cycle phase was assigned by eye for each experiment. Cells in the group of mCherry(-) and mVenus(-) were removed from analysis. Analysis was done in Python.

3.7 Acknowledgements

I would like to acknowledge NIGMS MIRA R35 GM139644 (A.E.P) for generous financial support. I thank the University of Colorado Flow Cytometry Core, which performed cell sorting and flow cytometric analysis of fixed cells, the University of Colorado Biochemistry Cell Culture Core (specifically Theresa Nahreini) for assistance with cell culture, and the BioFrontiers Computing Core and BioFrontiers IT for providing High Performance Computing resources. I also thank Joseph Dragavon for assistance with the microscopes available in the BioFrontiers Advanced Light Microscopy Core. I thank Dr. Luke Lavis (HHMI Janelia) for the JF669-HaloTag dye, and Dr. Sabrina Spencer (CU Boulder) for generously providing the MCF10a H2B-mTurquoise2, p21-mCitrine, DHB-mCherry cell line, and for the insightful comments on this manuscript. I also thank Dr. Shaun Bevers (University of Colorado School of Medicine Metabolomics Core, Aurora, CO) for preparing and analyzing the metabolomics samples.

Chapter 4: Future Directions

4.1 Zinc and the cell cycle

Zn^{2+} concentration changes throughout the cell cycle. More specifically, Zn^{2+} levels rise around mitosis and stay elevated in early G1. The magnitude of this "Zn^{2+} pulse" varies with media Zn^{2+} concentration. Despite adding to the field of Zn^{2+} biology, our study was unable to address where the Zn^{2+} comes from: Zn^{2+} is bound by proteins, sequestered inside of organelles, and present in high concentrations in the media, so it is plausible that the free Zn^{2+} is mobilized from one of these sources, or a combination. To address this, we can undertake stable isotope tracing of Zn^{2+} around the time of mitosis. By treating cells with a stable Zn^{2+} isotope, fixing cells, and analyzing the cells using nanoscale secondary ion mass spectrometry (NanoSIMS) to yield spatial information about liberated or imported Zn^{2+} stores during and after mitosis. We can then identify whether the Zn^{2+} ions are pumped in from the extracellular space or are liberated from intracellular stores in response to a process in early G1.

We also demonstrated that knockdown of MTF-1, a transcription factor involved in the high Zn^{2+} response, changes the shape and magnitude of the Zn^{2+} pulse. More obscure was the observation that knockdown of this transcription factor altered the *resting* Zn^{2+} levels in cells, counter to the canonical idea that MTF-1 is only responsible for responding to high Zn^{2+}. This raises the question of why this knockdown alters the resting Zn^{2+} concentration in cells. To address this question, we can use computational models of simplified Zn^{2+} regulatory networks to identify changes in free Zn^{2+} in a resting state and in response to a perturbation while varying MTF-1 concentration. Coupled with *in cellulo* quantitative proteomics, we can create an *in vivo* and *in silico* map of Zn^{2+} cellular dynamics to identify variations in tissue responses to high and low Zn^{2+}. Further, we can use an iterative immunofluorescence imaging modality against known Zn^{2+} homeostasis proteins to identify changes in expression of genes by MTF-1. This can yield insights into the temporal dynamics of MTF-1's regulation of resting and perturbed Zn^{2+} homeostasis.

4.2 Zinc and replication stress

Cells require Zn^{2+} for a myriad of cellular processes, including adequate DNA synthesis. A few early studies have identified that cells lacking Zn^{2+} fail to synthesize adequate DNA and, as a result, fail to proliferate in a timely manner. Adding to this canon of work, we have found that mild, transient Zn^{2+} deficiency reversibly inhibits DNA synthesis, as well as activates the DNA replication stress response. We found that Zn^{2+} deficiency activates this response via the Chk1 pathway, and is not due to underlicensing of replication origins in G1. Although there was some rescue of DNA synthesis upon co-treatment with a Chk1 inhibitor, it was not a full rescue, implying that Chk1 is inhibiting other origins of replication from firing and implies that Chk1 activation is a consequence of DNA synthesis impairment. To identify the exact mechanism of DNA synthesis impairment, we can look to an *in vitro* model system to identify what part of the DNA replication complex is Zn^{2+} dependent. By purifying components of the eukaryotic replisome and monitoring DNA synthesis rates under Zn^{2+} deficient conditions, we can identify whether the replication complex is impaired when deprived of Zn^{2+}. We can also use this *in vitro* reconstituted replisome to identify Zn^{2+} occupancy of metal binding proteins after exposure to Zn^{2+} deficiency by using cysteine reactive proteomics. This can yield a deeper insight into the molecular basis of how Zn^{2+} deficiency can alter DNA synthesis.

Bibliography

1. A. Shenkin, The key role of micronutrients. *Clin. Nutr.* **25**, 1–13 (2006).
2. K. Jurowski, B. Szewczyk, G. Nowak, W. Piekoszewski, Biological consequences of zinc deficiency in the pathomechanisms of selected diseases. *JBIC J. Biol. Inorg. Chem.* **19**, 1069–1079 (2014).
3. S. Y. Hess, National Risk of Zinc Deficiency as Estimated by National Surveys. *Food Nutr Bull* **38**, 3–17 (2017).
4. S. P. Nations, *et al.*, An unusual source of excess zinc, leading to hypocupremia and neurologic disease (2008).
5. T. Hara, *et al.*, Physiological roles of zinc transporters: molecular and genetic importance in zinc homeostasis. *J. Physiol. Sci.* **67**, 283–301 (2017).
6. T. Kambe, T. Tsuji, A. Hashimoto, N. Itsumura, The Physiological, Biochemical, and Molecular Roles of Zinc Transporters in Zinc Homeostasis and Metabolism. *Physiol. Rev.* **95**, 749–784 (2015).
7. W. Maret, Molecular aspects of human cellular zinc homeostasis: redox control of zinc potentials and zinc signals. *BioMetals* **22**, 149–157 (2009).
8. K. P. Carter, M. C. Carpenter, B. Fiedler, R. Jimenez, A. E. Palmer, Critical Comparison of FRET-Sensor Functionality in the Cytosol and Endoplasmic Reticulum and Implications for Quantification of Ions. *Anal. Chem.* **89**, 9601–9608 (2017).
9. C. Andreini, L. Banci, I. Bertini, A. Rosato, Counting the Zinc-Proteins Encoded in the Human Genome. *J. Proteome Res.* **5**, 196–201 (2006).
10. A. Rakshit, S. E. Holtzen, M. N. Lo, K. A. Conway, A. E. Palmer, Human cells experience a Zn^{2+} pulse in early G1. *Cell Rep.* **42**, 112656 (2023).
11. L. Sanford, A. E. Palmer, Dissociated Hippocampal Neurons Exhibit Distinct Zn^{2+} Dynamics in a Stimulation-Method-Dependent Manner. *ACS Chem Neurosci* **11**, 508–514 (2020).
12. L. Sanford, M. C. Carpenter, A. E. Palmer, Intracellular Zn^{2+} transients modulate global gene expression in dissociated rat hippocampal neurons. *Sci. Rep.* **9**, 9411 (2019).
13. M. N. Lo, L. J. Damon, J. Wei Tay, S. Jia, A. E. Palmer, Single cell analysis reveals multiple requirements for zinc in the mammalian cell cycle. *eLife* **9**, e51107 (2020).
14. K. J. Anson, G. A. Corbet, A. E. Palmer, Zn^{2+} influx activates ERK and Akt signaling pathways. *Proc. Natl. Acad. Sci.* **118**, e2015786118 (2021).

15. A. C. Jackson, *et al.*, Identification of novel activators of the metal responsive transcription factor (MTF-1) using a gene expression biomarker in a microarray compendium. *Metallomics* **12**, 1400–1415 (2020).

16. A. Krężel, W. Maret, The Bioinorganic Chemistry of Mammalian Metallothioneins. *Chem. Rev.* **121**, 14594–14648 (2021).

17. L. Huang, S. Tepaamorndech, The SLC30 family of zinc transporters – A review of current understanding of their biological and pathophysiological roles. *Mol. Aspects Med.* **34**, 548–560 (2013).

18. J. E. Hardyman, *et al.*, Zinc sensing by metal-responsive transcription factor 1 (MTF1) controls metallothionein and ZnT1 expression to buffer the sensitivity of the transcriptome response to zinc. *Metallomics* **8**, 337–43 (2016).

19. V. Günther, U. Lindert, W. Schaffner, The taste of heavy metals: Gene regulation by MTF-1. *Biochim. Biophys. Acta BBA - Mol. Cell Res.* **1823**, 1416–1425 (2012).

20. N. Saydam, O. Georgiev, M. Y. Nakano, U. F. Greber, W. Schaffner, Nucleo-cytoplasmic Trafficking of Metal-regulatory Transcription Factor 1 Is Regulated by Diverse Stress Signals. *J. Biol. Chem.* **276**, 25487–25495 (2001).

21. Y. Wang, I. Lorenzi, O. Georgiev, W. Schaffner, Metal-responsive transcription factor-1 (MTF-1) selects different types of metal response elements at low vs. high zinc concentration. *Biol. Chem.* **385** (2004).

22. R. A. Colvin, W. R. Holmes, C. P. Fontaine, W. Maret, Cytosolic zinc buffering and muffling: Their role in intracellular zinc homeostasis. *Metallomics* **2**, 306–317 (2010).

23. L. A. Lichten, M. S. Ryu, L. Guo, J. Embury, R. J. Cousins, MTF-1-mediated repression of the zinc transporter Zip10 is alleviated by zinc restriction. *PLoS One* **6**, e21526 (2011).

24. A. T. Miles, G. M. Hawksworth, J. H. Beattie, V. Rodilla, Induction, regulation, degradation, and biological significance of mammalian metallothioneins. *Crit. Rev. Biochem. Mol. Biol.* **35**, 35–70 (2000).

25. R. D. Palmiter, The elusive function of metallothioneins. *Proc. Natl. Acad. Sci. U. S. A.* **95**, 8428–8430 (1998).

26. W. W. Nagel, B. L. Vallee, Cell cycle regulation of metallothionein in human colonic cancer cells. *Proc. Natl. Acad. Sci. U. S. A.* **92**, 579–583 (1995).

27. A. Krężel, W. Maret, Zinc-buffering capacity of a eukaryotic cell at physiological pZn. *JBIC J. Biol. Inorg. Chem.* **11**, 1049–1062 (2006).

28. J. S. Scheller, G. W. Irvine, M. J. Stillman, Unravelling the mechanistic details of metal binding to mammalian metallothioneins from stoichiometric, kinetic, and binding affinity data. *Dalton Trans.* **47**, 3613–3637 (2018).

29. T. Y. Li, D. T. Minkel, C. F. Shaw, D. H. Petering, On the reactivity of metallothioneins with 5,5′-dithiobis-(2-nitrobenzoic acid). *Biochem. J.* **193**, 441–446 (1981).

30. W. Maret, Metallothionein/disulfide interactions, oxidative stress, and the mobilization of cellular zinc. *Neurochem. Int.* **27**, 111–117 (1995).

31. M. Lu, D. Fu, Structure of the Zinc Transporter YiiP. *Science* **317**, 1746–1748 (2007).

32. C. Pang, J. Chai, P. Zhu, J. Shanklin, Q. Liu, Structural mechanism of intracellular autoregulation of zinc uptake in ZIP transporters. *Nat. Commun.* **14**, 3404 (2023).

33. J. Hyld, E. Ramos, D. Ram, The two-domain elevator-type mechanism of zinc-transporting ZIP proteins. *Sci. Adv.* (2022).

34. M. Lu, J. Chai, D. Fu, Structural basis for autoregulation of the zinc transporter YiiP. *Nat. Struct. Mol. Biol.* **16**, 1063–1067 (2009).

35. H. B. Bui, *et al.*, Cryo-EM structures of human zinc transporter ZnT7 reveal the mechanism of Zn2+ uptake into the Golgi apparatus. *Nat. Commun.* **14**, 4770 (2023).

36. Y. Golan, R. Alhadeff, A. Warshel, Y. G. Assaraf, ZnT2 is an electroneutral proton-coupled vesicular antiporter displaying an apparent stoichiometry of two protons per zinc ion. *PLOS Comput. Biol.* **15**, e1006882 (2019).

37. T. Kambe, A. Hashimoto, S. Fujimoto, Current understanding of ZIP and ZnT zinc transporters in human health and diseases. *Cell. Mol. Life Sci.* **71**, 3281–3295 (2014).

38. R. E. Dempski, "Chapter Nine - The Cation Selectivity of the ZIP Transporters" in *Current Topics in Membranes*, Metal Transporters., J. M. Argüello, S. Lutsenko, Eds. (Academic Press, 2012), pp. 221–245.

39. N. Dietrich, D. L. Schneider, K. Kornfeld, A pathway for low zinc homeostasis that is conserved in animals and acts in parallel to the pathway for high zinc homeostasis. *Nucleic Acids Res.* **45**, 11658–11672 (2017).

40. M. E. Corkins, *et al.*, Zinc finger protein Loz1 is required for zinc-responsive regulation of gene expression in fission yeast. *Proc. Natl. Acad. Sci.* **110**, 15371–15376 (2013).

41. D. J. Eide, TRANSCRIPTION FACTORS AND TRANSPORTERS IN ZINC HOMEOSTASIS: LESSONS LEARNED FROM FUNGI. *Crit. Rev. Biochem. Mol. Biol.* **55**, 88–110 (2020).

42. M. Yan, Y. Song, C. P. Wong, K. Hardin, E. Ho, Zinc Deficiency Alters DNA Damage Response Genes in Normal Human Prostate Epithelial Cells. *J. Nutr.* **138**, 667–673 (2008).

43. C.-T. Han, N. W. Schoene, K. Y. Lei, Influence of zinc deficiency on Akt-Mdm2-p53 and Akt-p21 signaling axes in normal and malignant human prostate cells. **297**, 12 (2009).

44. S. H. K. Wong, *et al.*, Zinc deficiency depresses p21 gene expression: inhibition of cell cycle progression is independent of the decrease in p21 protein level in HepG2 cells. *Am. J. Physiol.-Cell Physiol.* **292**, C2175–C2184 (2007).

45. K. A. McCall, C. Huang, C. A. Fierke, Function and mechanism of zinc metalloenzymes. *J. Nutr.* **130**, 1437S–46S (2000).

46. K. Kluska, J. Adamczyk, A. Krężel, Metal binding properties, stability and reactivity of zinc fingers. *Coord. Chem. Rev.* **367**, 18–64 (2018).

47. S. A. Lambert, *et al.*, The Human Transcription Factors. *Cell* **172**, 650–665 (2018).

48. Y. Li, W. Maret, Transient fluctuations of intracellular zinc ions in cell proliferation. *Exp. Cell Res.* **315**, 2463–2470 (2009).

49. L. J. Damon, J. Aaron, A. E. Palmer, Single molecule microscopy to profile the effect of zinc status on transcription factor dynamics. *Sci Rep* **12**, 17789 (2022).

50. C. Zhang, D. Maslar, T. F. Minckley, K. D. LeJeune, Y. Qin, Spontaneous, synchronous zinc spikes oscillate with neural excitability and calcium spikes in primary hippocampal neuron culture. *J. Neurochem.* **157**, 1838–1849 (2021).

51. L. J. Damon, *et al.*, “Cellular zinc status alters chromatin accessibility and binding of transcription factor p53 to genomic sites” (Genomics, 2023) https:/doi.org/10.1101/2023.11.20.567954 (March 10, 2024).

52. S. L. Kelleher, N. H. McCormick, V. Velasquez, V. Lopez, Zinc in Specialized Secretory Tissues: Roles in the Pancreas, Prostate, and Mammary Gland. *Adv. Nutr.* **2**, 101–111 (2011).

53. R. B. Franklin, *et al.*, Human ZIP1 is a major zinc uptake transporter for the accumulation of zinc in prostate cells. *J. Inorg. Biochem.* **96**, 435–442 (2003).

54. D. J. Eide, Zinc transporters and the cellular trafficking of zinc. *Biochim. Biophys. Acta BBA - Mol. Cell Res.* **1763**, 711–722 (2006).

55. Y. Han, J. M. Goldberg, S. J. Lippard, A. E. Palmer, Superiority of SpiroZin2 Versus FluoZin-3 for monitoring vesicular Zn^{2+} allows tracking of lysosomal Zn^{2+} pools. *Sci. Rep.* **8**, 15034 (2018).

56. A. M. Kim, *et al.*, Zinc sparks are triggered by fertilization and facilitate cell cycle resumption in mammalian eggs. *ACS Chem Biol* **6**, 716–23 (2011).

57. F. E. Duncan, *et al.*, The zinc spark is an inorganic signature of human egg activation. *Sci. Rep.* **6**, 24737 (2016).

58. E. L. Que, *et al.*, Quantitative mapping of zinc fluxes in the mammalian egg reveals the origin of fertilization-induced zinc sparks. *Nat Chem* **7**, 130–9 (2015).

59. B. Zhu, *et al.*, Increased expression of zinc transporter ZIP4, ZIP11, ZnT1, and ZnT6 predicts poor prognosis in pancreatic cancer. *J Trace Elem Med Biol* **65**, 126734 (2021).

60. P. Chandler, *et al.*, Subtype-specific accumulation of intracellular zinc pools is associated with the malignant phenotype in breast cancer. *Mol. Cancer* **15**, 2 (2016).

61. K. V. Sullivan, *et al.*, Zinc stable isotope analysis reveals Zn dyshomeostasis in benign tumours, breast cancer, and adjacent histologically normal tissue. *Metallomics* **13**, mfab027 (2021).

62. R. R. Prasad, *et al.*, Stage-specific differential expression of zinc transporter SLC30A and SLC39A family proteins during prostate tumorigenesis. *Mol. Carcinog.* **61**, 454–471 (2022).

63. G. R. Rosania, Y.-T. Chang, Targeting hyperproliferative disorders with cyclin dependent kinase inhibitors. *Expert Opin. Ther. Pat.* **10**, 215–230 (2000).

64. S. Gookin, *et al.*, A map of protein dynamics during cell-cycle progression and cell-cycle exit. *PLOS Biol.* **15**, e2003268 (2017).

65. K. J. Barnum, M. J. O'Connell, "Cell Cycle Regulation by Checkpoints" in *Cell Cycle Control: Mechanisms and Protocols*, Methods in Molecular Biology., E. Noguchi, M. C. Gadaleta, Eds. (Springer, 2014), pp. 29–40.

66. K. Vermeulen, D. R. Van Bockstaele, Z. N. Berneman, The cell cycle: a review of regulation, deregulation and therapeutic targets in cancer. *Cell Prolif* **36**, 131–49 (2003).

67. M. Malumbres, Cyclin-dependent kinases. *Genome Biol.* **15**, 122 (2014).

68. K. W. Overton, S. L. Spencer, W. L. Noderer, T. Meyer, C. L. Wang, Basal p21 controls population heterogeneity in cycling and quiescent cell cycle states. *Proc. Natl. Acad. Sci.* **111**, E4386–E4393 (2014).

69. O. Aprelikova, Y. Xiong, E. T. Liu, Both p16 and p21 Families of Cyclin-dependent Kinase (CDK) Inhibitors Block the Phosphorylation of Cyclin-dependent Kinases by the CDK-activating Kinase *. *J. Biol. Chem.* **270**, 18195–18197 (1995).

70. G. P. Ilyin, D. Glaise, D. Gilot, G. Baffet, C. Guguen-Guillouzo, Regulation and role of p21 and p27 cyclin-dependent kinase inhibitors during hepatocyte differentiation and growth. *Am. J. Physiol.-Gastrointest. Liver Physiol.* **285**, G115–G127 (2003).

71. J. Moser, I. Miller, D. Carter, S. L. Spencer, Control of the Restriction Point by Rb and p21. *Proc. Natl. Acad. Sci.* **115**, E8219–E8227 (2018).

72. I. Thurlings, A. de Bruin, "E2F Transcription Factors Control the Roller Coaster Ride of Cell Cycle Gene Expression" in *Cell Cycle Oscillators: Methods and Protocols*, Methods in Molecular Biology., A. S. Coutts, L. Weston, Eds. (Springer, 2016), pp. 71–88.

73. G. Yao, T. J. Lee, S. Mori, J. R. Nevins, L. You, A bistable Rb–E2F switch underlies the restriction point. *Nat. Cell Biol.* **10**, 476–482 (2008).

74. D. G. Johnson, J. DeGregori, Putting the Oncogenic and Tumor Suppressive Activities of E2F into Context. *Curr. Mol. Med.* **6**, 731–738 (2006).

75. C. H. Topham, S. S. Taylor, Mitosis and apoptosis: how is the balance set? *Curr. Opin. Cell Biol.* **25**, 780–785 (2013).

76. P. Saha, Q. Eichbaum, E. D. Silberman, B. J. Mayer, A. Dutta, p21CIP1 and Cdc25A: Competition between an Inhibitor and an Activator of Cyclin-Dependent Kinases. *Mol. Cell. Biol.* **17**, 4338–4345 (1997).

77. R. D. Hernansaiz-Ballesteros, C. Földi, L. Cardelli, L. G. Nagy, A. Csikász-Nagy, Evolution of opposing regulatory interactions underlies the emergence of eukaryotic cell cycle checkpoints. *Sci. Rep.* **11**, 11122 (2021).

78. S. L. Spencer, *et al.*, The Proliferation-Quiescence Decision Is Controlled by a Bifurcation in CDK2 Activity at Mitotic Exit. *Cell* **155**, 369–383 (2013).

79. J. P. Matson, J. G. Cook, Cell cycle proliferation decisions: the impact of single cell analyses. *FEBS J.* **284**, 362–375 (2017).

80. M. Min, Y. Rong, C. Tian, S. L. Spencer, Temporal integration of mitogen history in mother cells controls proliferation of daughter cells. *Science* **368**, 1261–1265 (2020).

81. J. C. Limas, J. G. Cook, Preparation for DNA replication: the key to a successful S phase. *FEBS Lett.* **593**, 2853–2867 (2019).

82. N. Rhind, P. Russell, Signaling Pathways that Regulate Cell Division. *Cold Spring Harb. Perspect. Biol.* **4**, a005942–a005942 (2012).

83. B. Grallert, E. Boye, The multiple facets of the intra-S checkpoint. *Cell Cycle* **7**, 2315–2320 (2008).

84. H. K. Matthews, C. Bertoli, R. A. M. de Bruin, Cell cycle control in cancer. *Nat. Rev. Mol. Cell Biol.* **23**, 74–88 (2022).

85. F. Bleichert, Mechanisms of replication origin licensing: a structural perspective. *Curr. Opin. Struct. Biol.* **59**, 195–204 (2019).

86. D. Remus, *et al.*, Concerted Loading of Mcm2–7 Double Hexamers around DNA during DNA Replication Origin Licensing. *Cell* **139**, 719–730 (2009).

87. M. L. DePamphilis, *et al.*, Regulating the licensing of DNA replication origins in metazoa. *Curr. Opin. Cell Biol.* **18**, 231–239 (2006).

88. N. Rhind, DNA replication timing: random thoughts about origin firing. *Nat. Cell Biol.* **8**, 1313–1316 (2006).

89. D. R. Iyer, N. Rhind, The Intra-S Checkpoint Responses to DNA Damage. *Genes* **8**, 74 (2017).

90. M. K. Zeman, K. A. Cimprich, Causes and consequences of replication stress. *Nat. Cell Biol.* **16**, 2–9 (2014).

91. S. Koundrioukoff, *et al.*, Stepwise Activation of the ATR Signaling Pathway upon Increasing Replication Stress Impacts Fragile Site Integrity. *PLoS Genet.* **9**, e1003643 (2013).

92. J. Smith, L. Mun Tho, N. Xu, D. A. Gillespie, "Chapter 3 - The ATM–Chk2 and ATR–Chk1 Pathways in DNA Damage Signaling and Cancer" in *Advances in Cancer Research*, G. F. Vande Woude, G. Klein, Eds. (Academic Press, 2010), pp. 73–112.

93. W. R. Taylor, G. R. Stark, Regulation of the G2/M transition by p53. *Oncogene* **20**, 1803–1815 (2001).

94. S. M. Kim, S. L. Forsburg, Replication stress by MMS stimulates DNA synthesis in post-replicative G2-phase in S. pombe . *MicroPublication Biol.* **2023**, 10.17912/micropub.biology.000852.

95. L. H. Daigh, C. Liu, M. Chung, K. A. Cimprich, T. Meyer, Stochastic Endogenous Replication Stress Causes ATR-Triggered Fluctuations in CDK2 Activity that Dynamically Adjust Global DNA Synthesis Rates. *Cell Syst.* **7**, 17-27.e3 (2018).

96. A. R. Barr, *et al.*, DNA damage during S-phase mediates the proliferation-quiescence decision in the subsequent G1 via p21 expression. *Nat. Commun.* **8**, 14728 (2017).

97. J. R. McIntosh, Mitosis. *Cold Spring Harb. Perspect. Biol.* **8**, a023218 (2016).

98. P. Strzyz, No proper rest in mitosis. *Nat. Rev. Mol. Cell Biol.* **18**, 653–653 (2017).

99. H. X. Chao, *et al.*, Evidence that the human cell cycle is a series of uncoupled, memoryless phases. *Mol Syst Biol* **15**, e8604 (2019).

100. J. K. Chesters, R. Boyne, Nature of the Zn^{2+} requirement for DNA synthesis by 3T3 cells. *Exp. Cell Res.* **192**, 631–634 (1991).

101. H. Rubin, Inhibition of DNA synthesis in animal cells by ethylene diamine tetraacetate, and its reversal by zinc. *Proc. Natl. Acad. Sci. U. S. A.* **69**, 712–716 (1972).

102. K. Watanabe, K. Hasegawa, H. Ohtake, C. Tohyama, M. Koga, Inhibition of DNA Synthesis by EDTA and its Cancellation by Zinc in Primary Cultures of Adult Rat Hepatocytes. *Biomed. Res.* **14**, 99–110 (1993).

103. J. K. Chesters, L. Petrie, A possible role for cyclins in the zinc requirements during G1 and G2 phases of the cell cycle. *J. Nutr. Biochem.* **10**, 279–290 (1999).

104. M. Min, S. L. Spencer, Spontaneously slow-cycling subpopulations of human cells originate from activation of stress-response pathways. *PLOS Biol.* **17**, e3000178 (2019).

105. J. P. Matson, *et al.*, Intrinsic checkpoint deficiency during cell cycle re-entry from quiescence. *J. Cell Biol.* **218**, 2169–2184 (2019).

106. C. K. Vilas, L. E. Emery, E. L. Denchi, K. M. Miller, Caught with One's Zinc Fingers in the Genome Integrity Cookie Jar. *Trends Genet.* **34**, 313–325 (2018).

107. J. E. Phillips, V. G. Corces, CTCF: Master Weaver of the Genome. *Cell* **137**, 1194–1211 (2009).

108. A. R. Blanden, *et al.*, Zinc shapes the folding landscape of p53 and establishes a pathway for reactivating structurally diverse cancer mutants. *eLife* **9**, e61487 (2020).

109. E. Ho, B. N. Ames, Low intracellular zinc induces oxidative DNA damage, disrupts p53, NFκB, and AP1 DNA binding, and affects DNA repair in a rat glioma cell line. *Proc. Natl. Acad. Sci.* **99**, 16770–16775 (2002).

110. E. Ho, C. Courtemanche, B. N. Ames, Zinc Deficiency Induces Oxidative DNA Damage and Increases P53 Expression in Human Lung Fibroblasts. *J. Nutr.* **133**, 2543–2548 (2003).

111. M. Fischer, Census and evaluation of p53 target genes. 14 (2017).

112. D. J. Eide, The oxidative stress of zinc deficiency. *Metallomics* **3**, 1124–1129 (2011).

113. M. Son, U. Srikanth, K. Puttaparthi, C. Luther, J. L. Elliott, Biochemical properties and in vivo effects of the SOD1 zinc-binding site mutant (H80G). *J. Neurochem.* **118**, 891–901 (2011).

114. S. V. Seetharaman, *et al.*, Disrupted Zinc-Binding Sites in Structures of Pathogenic SOD1 Variants D124V and H80R. *Biochemistry* **49**, 5714–5725 (2010).

115. K. Homma, *et al.*, SOD1 as a Molecular Switch for Initiating the Homeostatic ER Stress Response under Zinc Deficiency. *Mol. Cell* **52**, 75–86 (2013).

116. R. J. Radford, S. J. Lippard, Chelators for investigating zinc metalloneurochemistry. *Curr. Opin. Chem. Biol.* **17**, 129–136 (2013).

117. T. Takeda, *et al.*, Zinc deficiency causes delayed ATP clearance and adenosine generation in rats and cell culture models. *Commun. Biol.* **1**, 1–13 (2018).

118. S. D. Dick, *et al.*, Structural Basis for the Activation and Target Site Specificity of CDC7 Kinase. *Structure* **28**, 954-962.e4 (2020).

119. J. P. Slater, A. S. Mildvan, L. A. Loeb, ZINC in DNA polymerases. *Biochem. Biophys. Res. Commun.* **44**, 37–43 (1971).

120. F. Y. H. Wu, C. W. Wu, Zinc in DNA Replication and Transcription. *Annu. Rev. Nutr.* **7**, 251–272 (1987).

121. E. P. S. Pratt, L. J. Damon, K. J. Anson, A. E. Palmer, Tools and techniques for illuminating the cell biology of zinc. *Biochim. Biophys. Acta BBA - Mol. Cell Res.* **1868**, 118865 (2021).

122. Y. Qin, *et al.*, Direct comparison of a genetically encoded sensor and small molecule indicator: implications for quantification of cytosolic Zn(2+). *ACS Chem Biol* **8**, 2366–71 (2013).

123. T.-W. Chen, *et al.*, Ultrasensitive fluorescent proteins for imaging neuronal activity. *Nature* **499**, 295–300 (2013).

124. J. Akerboom, *et al.*, Crystal Structures of the GCaMP Calcium Sensor Reveal the Mechanism of Fluorescence Signal Change and Aid Rational Design*. *J. Biol. Chem.* **284**, 6455–6464 (2009).

125. A. A. Pakhomov, V. I. Martynov, GFP Family: Structural Insights into Spectral Tuning. *Chem. Biol.* **15**, 755–764 (2008).

126. Y. Qin, D. W. Sammond, E. Braselmann, M. C. Carpenter, A. E. Palmer, Development of an Optical Zn^{2+} Probe Based on a Single Fluorescent Protein. *ACS Chem. Biol.* **11**, 2744–2751 (2016).

127. Y. Zhang, *et al.*, Fast and sensitive GCaMP calcium indicators for imaging neural populations. *Nature* **615**, 884–891 (2023).

128. B. L. Fiedler, *et al.*, Droplet Microfluidic Flow Cytometer For Sorting On Transient Cellular Responses Of Genetically-Encoded Sensors. *Anal. Chem.* **89**, 711–719 (2017).

129. M. Chen, *et al.*, Genetically Encoded, Photostable Indicators to Image Dynamic Zn2+ Secretion of Pancreatic Islets. *Anal. Chem.* **91**, 12212–12219 (2019).

130. Z. Chen, H. Ai, Single Fluorescent Protein-Based Indicators for Zinc Ion (Zn^{2+}). *Anal. Chem.* **88**, 9029–9036 (2016).

131. E. A. Jares-Erijman, T. M. Jovin, FRET imaging. *Nat. Biotechnol.* **21**, 1387–1395 (2003).

132. J. L. Vinkenborg, *et al.*, Genetically encoded FRET sensors to monitor intracellular Zn2+ homeostasis. *Nat. Methods* **6**, 737–40 (2009).

133. A. E. Palmer, R. Y. Tsien, Measuring calcium signaling using genetically targetable fluorescent indicators. *Nat. Protoc.* **1**, 1057–1065 (2006).

134. A. E. Palmer, Y. Qin, J. G. Park, J. E. McCombs, Design and application of genetically encoded biosensors. *Trends Biotechnol.* **29**, 144–152 (2011).

135. L. H. Lindenburg, J. L. Vinkenborg, J. Oortwijn, S. J. A. Aper, M. Merkx, MagFRET: The First Genetically Encoded Fluorescent Mg2+ Sensor. *PLOS ONE* **8**, e82009 (2013).

136. Y. Qin, P. J. Dittmer, J. G. Park, K. B. Jansen, A. E. Palmer, Measuring steady-state and dynamic endoplasmic reticulum and Golgi Zn2+ with genetically encoded sensors. *Proc. Natl. Acad. Sci.* **108**, 7351–7356 (2011).

137. C. Deo, *et al.*, The HaloTag as a general scaffold for far-red tunable chemigenetic indicators. *Nat. Chem. Biol.* **17**, 718–723 (2021).

138. C. Deo, *et al.*, The HaloTag as a general scaffold for far-red tunable chemigenetic indicators. *Nat. Chem. Biol.* **17**, 718–723 (2021).

139. D. Zhang, *et al.*, Design of a palette of SNAP-tag mimics of fluorescent proteins and their use as cell reporters. *Cell Discov.* **9**, 1–17 (2023).

140. C. G. England, H. Luo, W. Cai, HaloTag Technology: A Versatile Platform for Biomedical Applications. *Bioconjug. Chem.* **26**, 975–986 (2015).

141. X. Sun, *et al.*, Development of SNAP-Tag Fluorogenic Probes for Wash-Free Fluorescence Imaging. *ChemBioChem* **12**, 2217–2226 (2011).

142. Y. Matsui, *et al.*, Visualization of long-term Mg2+ dynamics in apoptotic cells using a novel targetable fluorescent probe. *Chem. Sci.* **8**, 8255–8264 (2017).

143. C. R. Goldsmith, S. J. Lippard, 6-Methylpyridyl for Pyridyl Substitution Tunes the Properties of Fluorescent Zinc Sensors of the Zinpyr Family. *Inorg. Chem.* **45**, 555–561 (2006).

144. T. Budde, A. Minta, J. A. White, A. R. Kay, Imaging free zinc in synaptic terminals in live hippocampal slices. *Neuroscience* **79**, 347–358 (1997).

145. G. K. Walkup, S. C. Burdette, S. J. Lippard, R. Y. Tsien, A New Cell-Permeable Fluorescent Probe for Zn^{2+}. *J. Am. Chem. Soc.* **122**, 5644–5645 (2000).

146. S. C. Burdette, C. J. Frederickson, W. Bu, S. J. Lippard, ZP4, an Improved Neuronal Zn^{2+} Sensor of the Zinpyr Family. *J. Am. Chem. Soc.* **125**, 1778–1787 (2003).

147. E. P. S. Pratt, K. J. Anson, J. K. Tapper, D. M. Simpson, A. E. Palmer, Systematic Comparison of Vesicular Targeting Signals Leads to the Development of Genetically Encoded Vesicular Fluorescent Zn2+ and pH Sensors. *ACS Sens.* **5**, 3879–3891 (2020).

148. G. R. Rosania, K. Shedden, N. Zheng, X. Zhang, Visualizing chemical structure-subcellular localization relationships using fluorescent small molecules as probes of cellular transport. *J. Cheminformatics* **5**, 44 (2013).

149. T. M. Oyama, M. Saito, T. Yonezawa, Y. Okano, Y. Oyama, Nanomolar concentrations of zinc pyrithione increase cell susceptibility to oxidative stress induced by hydrogen peroxide in rat thymocytes. *Chemosphere* **87**, 1316–1322 (2012).

150. N. L. Reeder, *et al.*, The antifungal mechanism of action of zinc pyrithione. *Br. J. Dermatol.* **165**, 9–12 (2011).

151. N. L. Reeder, *et al.*, Zinc Pyrithione Inhibits Yeast Growth through Copper Influx and Inactivation of Iron-Sulfur Proteins. *Antimicrob. Agents Chemother.* **55**, 5753–5760 (2011).

152. Z. Huang, X. Zhang, M. Bosch, S. J. Smith, S. J. Lippard, Tris(2-pyridylmethyl)amine (TPA) as a membrane-permeable chelator for interception of biological mobile zinc†. *Metallomics* **5**, 648–655 (2013).

153. J. W. Meeusen, A. Nowakowski, D. H. Petering, Reaction of Metal-Binding Ligands with the Zinc Proteome: Zinc Sensors and N,N,N′,N′-Tetrakis(2-pyridylmethyl)ethylenediamine. *Inorg. Chem.* **51**, 3625–3632 (2012).

154. R. E. Carraway, P. R. Dobner, Zinc pyrithione induces ERK- and PKC-dependent necrosis distinct from TPEN-induced apoptosis in prostate cancer cells. *Biochim. Biophys. Acta BBA - Mol. Cell Res.* **1823**, 544–557 (2012).

155. G. Anderegg, E. Hubmann, N. G. Podder, F. Wenk, Pyridinderivate als Komplexbildner. XI. Die Thermodynamik der Metallkomplexbildung mit Bis-, Tris- und Tetrakis[(2-pyridyl)methyl]-aminen. *Helv. Chim. Acta* **60**, 123–140 (1977).

156. J. H. Kaplan, E. B. Maryon, How Mammalian Cells Acquire Copper: An Essential but Potentially Toxic Metal. *Biophys. J.* **110**, 7–13 (2016).

157. E. Pan, *et al.*, Vesicular zinc promotes presynaptic and inhibits postsynaptic long term potentiation of mossy fiber-CA3 synapse. *Neuron* **71**, 1116–1126 (2011).

158. P. Paoletti, A. M. Vergnano, B. Barbour, M. Casado, Zinc at glutamatergic synapses. *Neuroscience* **158**, 126–136 (2009).

159. P. T. Grant, T. L. Coombs, B. H. Frank, Differences in the nature of the interaction of insulin and proinsulin with zinc. *Biochem. J.* **126**, 433–440 (1972).

160. J. W. Finley, M. Briske-Anderson, P. G. Reeves, L. K. Johnson, Zinc uptake and transcellular movement by CACO-2 cells: Studies with media containing fetal bovine serum. *J. Nutr. Biochem.* **6**, 137–144 (1995).

161. M. Clegg, L. Hanna, B. Niles, T. Momma, C. Keen, Zinc deficiency-induced cell death. *IUBMB Life Int. Union Biochem. Mol. Biol. Life* **57**, 661–669 (2005).

162. C. E. R. Richardson, *et al.*, A Method for Selective Depletion of Zn(II) Ions from Complex Biological Media and Evaluation of Cellular Consequences of Zn(II) Deficiency. *J. Am. Chem. Soc.* **140**, 2413–2416 (2018).

163. D. Beauchemin, Inductively Coupled Plasma Mass Spectrometry. *Anal. Chem.* **80**, 4455–4486 (2008).

164. S. Regot, J. J. Hughey, B. T. Bajar, S. Carrasco, M. W. Covert, High-sensitivity measurements of multiple kinase activities in live single cells. *Cell* **157**, 1724–1734 (2014).

165. T. Kudo, *et al.*, Live-cell measurements of kinase activity in single cells using translocation reporters. *Nat. Protoc.* **13**, 155–169 (2018).

166. T. la Cour, *et al.*, Analysis and prediction of leucine-rich nuclear export signals. *Protein Eng. Des. Sel.* **17**, 527–536 (2004).

167. M. R. Hodel, A. H. Corbett, A. E. Hodel, Dissection of a Nuclear Localization Signal *. *J. Biol. Chem.* **276**, 1317–1325 (2001).

168. A. K. Kim, H. D. Wu, T. Inoue, Rational Design of a Protein Kinase A Nuclear-cytosol Translocation Reporter. *Sci. Rep.* **10**, 9365 (2020).

169. H. W. Yang, *et al.*, Stress-mediated exit to quiescence restricted by increasing persistence in CDK4/6 activation. *eLife* **9**, e44571 (2020).

170. T. Radtke, D. Schmalz, E. Coutavas, T. M. Soliman, R. Peters, Kinetics of protein import into isolated Xenopus oocyte nuclei. *Proc. Natl. Acad. Sci.* **98**, 2407–2412 (2001).

171. H. L. Rust, P. R. Thompson, Kinase Consensus Sequences: A Breeding Ground for Crosstalk. *ACS Chem. Biol.* **6**, 881–892 (2011).

172. L. K. Teixeira, S. I. Reed, Ubiquitin Ligases and Cell Cycle Control. *Annu. Rev. Biochem.* **82**, 387–414 (2013).

173. K. I. Nakayama, K. Nakayama, Ubiquitin ligases: cell-cycle control and cancer. *Nat. Rev. Cancer* **6**, 369–381 (2006).

174. A. Sakaue-Sawano, *et al.*, Visualizing Spatiotemporal Dynamics of Multicellular Cell-Cycle Progression. *Cell* **132**, 487–498 (2008).

175. A. Sakaue-Sawano, *et al.*, Genetically Encoded Tools for Optical Dissection of the Mammalian Cell Cycle. *Mol. Cell* **68**, 626-640.e5 (2017).

176. G. D. Grant, K. M. Kedziora, J. C. Limas, J. G. Cook, J. E. Purvis, Accurate delineation of cell cycle phase transitions in living cells with PIP-FUCCI. *Cell Cycle* **17**, 2496–2516 (2018).

177. D. Mahdessian, *et al.*, Spatiotemporal dissection of the cell cycle with single-cell proteogenomics. *Nature* **590**, 649–654 (2021).

178. C. Vaziri, *et al.*, A p53-dependent checkpoint pathway prevents rereplication. *Mol. Cell* **11**, 997–1008 (2003).

179. J. E. Purvis, *et al.*, p53 dynamics control cell fate. *Science* **336**, 1440–1444 (2012).

180. S. Geny, *et al.*, “Tagging Proteins with Fluorescent Reporters Using the CRISPR/Cas9 System and Double-Stranded DNA Donors” in *Multiprotein Complexes: Methods and Protocols*, Methods in Molecular Biology., A. Poterszman, Ed. (Springer US, 2021), pp. 39–57.

181. T. Kanda, K. F. Sullivan, G. M. Wahl, Histone–GFP fusion protein enables sensitive analysis of chromosome dynamics in living mammalian cells. *Curr. Biol.* **8**, 377–385 (1998).

182. C. Tian, C. Yang, S. L. Spencer, EllipTrack: A Global-Local Cell-Tracking Pipeline for 2D Fluorescence Time-Lapse Microscopy. *Cell Rep.* **32**, 107984 (2020).

183. H. Leonhardt, *et al.*, Dynamics of DNA Replication Factories in Living Cells. *J. Cell Biol.* **149**, 271–280 (2000).

184. S. D. Cappell, M. Chung, A. Jaimovich, S. L. Spencer, T. Meyer, Irreversible APC Cdh1 Inactivation Underlies the Point of No Return for Cell-Cycle Entry. *Cell* **166**, 167–180 (2016).

185. B. T. Bajar, *et al.*, Fluorescent indicators for simultaneous reporting of all four cell cycle phases. *Nat. Methods* **13**, 993–996 (2016).

186. Y. Xiong, *et al.*, p21 is a universal inhibitor of cyclin kinases. *Nature* **366**, 701–704 (1993).

187. M. Matthaei, H. Meng, A. K. Meeker, C. G. Eberhart, A. S. Jun, Endothelial Cdkn1a (p21) Overexpression and Accelerated Senescence in a Mouse Model of Fuchs Endothelial Corneal Dystrophy. *Invest. Ophthalmol. Vis. Sci.* **53**, 6718–6727 (2012).

188. D. Weinstat-Saslow, *et al.*, Overexpression of cyclin D mRNA distinguishes invasive and in situ breast carcinomas from non-malignant lesions. *Nat. Med.* **1**, 1257–1260 (1995).

189. Z. Cai, *et al.*, Overexpressed Cyclin D1 and CDK4 proteins are responsible for the resistance to CDK4/6 inhibitor in breast cancer that can be reversed by PI3K/mTOR inhibitors. *Sci. China Life Sci.* **66**, 94–109 (2023).

190. R. Di Blasi, *et al.*, Resource-aware construct design in mammalian cells. *Nat. Commun.* **14**, 3576 (2023).

191. M. Jinek, *et al.*, A Programmable Dual-RNA–Guided DNA Endonuclease in Adaptive Bacterial Immunity. *Science* **337**, 816–821 (2012).

192. J. Goedhart, *et al.*, Structure-guided evolution of cyan fluorescent proteins towards a quantum yield of 93%. *Nat. Commun.* **3**, 751 (2012).

193. N. C. Shaner, *et al.*, A bright monomeric green fluorescent protein derived from Branchiostoma lanceolatum. *Nat. Methods* **10**, 407–409 (2013).

194. R. S. MacDonald, The role of zinc in growth and cell proliferation. *J Nutr* **130**, 1500s–8s (2000).

195. J. S. Severo, *et al.*, Role of Zinc in Zinc-α2-Glycoprotein Metabolism in Obesity: a Review of Literature. *Biol. Trace Elem. Res.* **193**, 81–88 (2020).

196. J. Olechnowicz, A. Tinkov, A. Skalny, J. Suliburska, Zinc status is associated with inflammation, oxidative stress, lipid, and glucose metabolism. *J Physiol Sci* **68**, 19–31 (2018).

197. C. G. C. Chesters, G. N. Rolinson, Role of Zinc in Metabolism. *Nature* **165**, 851–852 (1950).

198. J. K. Chesters, L. Petrie, H. Vint, Specificity and timing of the Zn^{2+} requirement for DNA synthesis by 3T3 cells. *Exp. Cell Res.* **184**, 499–508 (1989).

199. J. K. Chesters, L. Petrie, A. J. Travis, A requirement for Zn^{2+} for the induction of thymidine kinase but not ornithine decarboxylase in 3T3 cells stimulated from quiescence. *Biochem. J.* **272**, 525–527 (1990).

200. T. Kambe, K. M. Taylor, D. Fu, Zinc transporters and their functional integration in mammalian cells. *J Bio Chem* **296**, 100320 (2021).

201. A. Krężel, W. Maret, The Functions of Metamorphic Metallothioneins in Zinc and Copper Metabolism. *Int J Mol Sci* **18** (2017).

202. L. Ji, *et al.*, Knockout of MTF1 Inhibits the Epithelial to Mesenchymal Transition in Ovarian Cancer Cells. *J Cancer* **9**, 4578–4585 (2018).

203. D. Lim, K. M. Jocelyn, G. W. Yip, B. H. Bay, Silencing the Metallothionein-2A gene inhibits cell cycle progression from G1- to S-phase involving ATM and cdc25A signaling in breast cancer cells. *Cancer Lett* **276**, 109–17 (2009).

204. R. Studer, C. P. Vogt, M. Cavigelli, P. E. Hunziker, J. H. Kägi, Metallothionein accretion in human hepatic cells is linked to cellular proliferation. *Biochem. J.* **328 (Pt 1)**, 63–67 (1997).

205. R. McRae, B. Lai, C. J. Fahrni, Subcellular redistribution and mitotic inheritance of transition metals in proliferating mouse fibroblast cells. *Metallomics* **5**, 52–61 (2013).

206. S. Langmade, R. Ravindra, P. Daniels, G. Andrews, The transcription factor MTF-1 mediates metal regulation of the mouse ZnT1 gene. *J Biol Chem* **275**, 34803–34809 (2000).

207. Y. Wang, S. Zhang, S. J. Li, Zn^{2+} induces apoptosis in human highly metastatic SHG-44 glioma cells, through inhibiting activity of the voltage-gated proton channel Hv1. *Biochem. Biophys. Res. Commun.* **438**, 312–317 (2013).

208. L. Sun, Y. Chai, R. Hannigan, V. K. Bhogaraju, K. Machaca, Zinc regulates the ability of Cdc25C to activate MPF/cdk1. *J. Cell. Physiol.* **213**, 98–104 (2007).

209. H.-X. Yuan, Y. Xiong, K.-L. Guan, Nutrient Sensing, Metabolism, and Cell Growth Control. *Mol. Cell* **49**, 379–387 (2013).

210. S. Yamasaki, *et al.*, Zinc is a novel intracellular second messenger. *J. Cell Biol.* **177**, 637–645 (2007).

211. A. T. Hahn, J. T. Jones, T. Meyer, Quantitative analysis of cell cycle phase durations and PC12 differentiation using fluorescent biosensors. *Cell Cycle* **8**, 1044–1052 (2009).

212. K. Engeland, Cell cycle regulation: p53-p21-RB signaling. *Cell Death Differ.* **29**, 946–960 (2022).

213. D. Donjerkovic, D. W. Scott, Regulation of the G1 phase of the mammalian cell cycle. *Cell Res.* **10**, 1–16 (2000).

214. C. Gérard, A. Goldbeter, Temporal self-organization of the cyclin/Cdk network driving the mammalian cell cycle. *Proc. Natl. Acad. Sci.* **106**, 21643–21648 (2009).

215. M. Arora, J. Moser, H. Phadke, A. A. Basha, S. L. Spencer, Endogenous Replication Stress in Mother Cells Leads to Quiescence of Daughter Cells. *Cell Rep.* **19**, 1351–1364 (2017).

216. J. F. Nathans, J. A. Cornwell, M. M. Afifi, D. Paul, S. D. Cappell, Cell cycle inertia underlies a bifurcation in cell fates after DNA damage. *Sci. Adv.* **7**, eabe3882 (2021).

217. H. A. Coller, L. Sang, J. M. Roberts, A new description of cellular quiescence. *PLoS Biol.* **4**, e83 (2006).

218. F. S. Heldt, A. R. Barr, S. Cooper, C. Bakal, B. Novák, A comprehensive model for the proliferation–quiescence decision in response to endogenous DNA damage in human cells. *Proc. Natl. Acad. Sci.* **115**, 2532–2537 (2018).

219. F. F. Diehl, *et al.*, Nucleotide imbalance decouples cell growth from cell proliferation. *Nat. Cell Biol.* **24**, 1252–1264 (2022).

220. S. Clemens, The cell biology of zinc. *J. Exp. Bot.* **73**, 1688–1698 (2022).

221. A. Salic, T. J. Mitchison, A chemical method for fast and sensitive detection of DNA synthesis in vivo. *Proc. Natl. Acad. Sci.* **105**, 2415–2420 (2008).

222. M. E. Ashour, N. Mosammaparast, Mechanisms of damage tolerance and repair during DNA replication. *Nucleic Acids Res.* **49**, 3033–3047 (2021).

223. A. Ciccia, S. J. Elledge, The DNA Damage Response: Making it safe to play with knives. *Mol. Cell* **40**, 179–204 (2010).

224. A. C. Bester, *et al.*, Nucleotide Deficiency Promotes Genomic Instability in Early Stages of Cancer Development. *Cell* **145**, 435 (2011).

225. N. Böhly, *et al.*, Increased replication origin firing links replication stress to whole chromosomal instability in human cancer. *Cell Rep.* **41**, 111836 (2022).

226. N. Shaikh, *et al.*, Replication stress generates distinctive landscapes of DNA copy number alterations and chromosome scale losses. *Genome Biol.* **23**, 223 (2022).

227. S. Saxena, L. Zou, Hallmarks of DNA replication stress. *Mol. Cell* **82**, 2298–2314 (2022).

228. T. S. Byun, M. Pacek, M. Yee, J. C. Walter, K. A. Cimprich, Functional uncoupling of MCM helicase and DNA polymerase activities activates the ATR-dependent checkpoint. *Genes Dev.* **19**, 1040–1052 (2005).

229. D. R. Iyer, N. Rhind, Replication fork slowing and stalling are distinct, checkpoint-independent consequences of replicating damaged DNA. *PLOS Genet.* **13**, e1006958 (2017).

230. M. Huang, *et al.*, Chk1 and Chk2 are differentially involved in homologous recombination repair and cell cycle arrest in response to DNA double-strand breaks induced by camptothecins. *Mol. Cancer Ther.* **7**, 1440–1449 (2008).

231. W. Wu, *et al.*, Mitotic DNA synthesis in response to replication stress requires the sequential action of DNA polymerases zeta and delta in human cells. *Nat. Commun.* **14**, 706 (2023).

232. C. Mocanu, *et al.*, DNA replication is highly resilient and persistent under the challenge of mild replication stress. *Cell Rep.* **39**, 110701 (2022).

233. S. Spadari, F. Sala, G. Pedrali-Noy, Aphidicolin: a specific inhibitor of nuclear DNA replication in eukaryotes. *Trends Biochem. Sci.* **7**, 29–32 (1982).

234. The UniProt Consortium, UniProt: the Universal Protein Knowledgebase in 2023. *Nucleic Acids Res.* **51**, D523–D531 (2023).

235. R. Dua, D. L. Levy, J. L. Campbell, Role of the putative zinc finger domain of Saccharomyces cerevisiae DNA polymerase epsilon in DNA replication and the S/M checkpoint pathway. *J. Biol. Chem.* **273**, 30046–30055 (1998).

236. J. Sanchez Garcia, L. F. Ciufo, X. Yang, S. E. Kearsey, S. A. MacNeill, The C-terminal zinc finger of the catalytic subunit of DNA polymerase δ is responsible for direct interaction with the B-subunit. *Nucleic Acids Res.* **32**, 3005–3016 (2004).

237. T. J. Kelley, S. Moghaddas, R. Bose, S. Basu, Inhibition of immunopurified DNA polymerase-alpha from PA-3 prostate tumor cells by platinum (II) antitumor drugs. *Cancer Biochem. Biophys.* **13**, 135–146 (1993).

238. K. Mayanagi, *et al.*, Two conformations of DNA polymerase D-PCNA-DNA, an archaeal replisome complex, revealed by cryo-electron microscopy. *BMC Biol.* **18**, 152 (2020).

239. C. F. Springgate, A. S. Mildvan, R. Abramson, J. L. Engle, L. A. Loeb, Escherichia coli Deoxyribonucleic Acid Polymerase I, a Zinc Metalloenzyme: Nuclear Quadrupolar Relaxation Studies of the Role of Bound Zinc. *J. Biol. Chem.* **248**, 5987–5993 (1973).

240. J. B. Grimm, *et al.*, A general method to fine-tune fluorophores for live-cell and in vivo imaging. *Nat. Methods* **14**, 987–994 (2017).

241. T. Nemkov, J. A. Reisz, S. Gehrke, K. C. Hansen, A. D'Alessandro, "High-Throughput Metabolomics: Isocratic and Gradient Mass Spectrometry-Based Methods" in *High-Throughput Metabolomics: Methods and Protocols*, Methods in Molecular Biology., A. D'Alessandro, Ed. (Springer, 2019), pp. 13–26.

242. S. Agrawal, *et al.*, El-MAVEN: A Fast, Robust, and User-Friendly Mass Spectrometry Data Processing Engine for Metabolomics. *Methods Mol. Biol. Clifton NJ* **1978**, 301–321 (2019).

243. Z. Pang, *et al.*, MetaboAnalyst 5.0: narrowing the gap between raw spectra and functional insights. *Nucleic Acids Res.* **49**, W388–W396 (2021).